Distinct small-scale heterogeneity inferred from fluctuated envelopes of shallow earthquakes

神薗, めぐみ

Doctoral Thesis

Distinct small-scale heterogeneity inferred from fluctuated envelopes of shallow earthquakes

Megumi Kamizono

Department of Earth and Planetary Sciences,
Graduate School of Sciences, Kyushu university

January, 2019

Abstract

The Earth's internal structure is basically composed by stratified layers such as the crust, mantle, and core. However, detailed analyses on seismograms have revealed complex structure possibly due to earth's activity. Especially, in the crust, tectonic and volcanic evolution create complex structure. Therefore, it is considered that realistic structure of the earth's crust is characterized by the simple layered structure overlaid with small scale heterogeneity. According to the seismic wave theory, smaller scale heterogeneity than seismic wave length affects the waveform in terms of travel time and amplitude. There are numerous studies to investigate heterogeneous structure in the crust by using travel time of seismic wave and envelope of the waveform. In this study, we have improved a method estimating heterogeneous structure from envelope of observed seismogram and explored anomalous structure around hypocentral area of the 2016 Kumamoto earthquake sequence. Seismic waves traveling in a medium is deformed by heterogeneity, which can be seen as envelope decay and ripple in the envelope. Therefore, we adopted two approaches to evaluate effect of the heterogeneity.

The 2016 Kumamoto earthquake occurred in April 2016. The first earthquake (M6.5) occurred at 21:26 (JST) on April 14th. The main shock (M7.3) occurred at 1:25 (JST) on April 16th. The aftershock activity is high and the active area covers entire Hinagu and Futagawa fault zones. The range is across the entire length of approximately 100 km. The velocity structure by travel time tomography method in this area suggested that the heterogeneous feature controlled the seismic activity. In this study, we investigate relationship between the activity and heterogeneous structure with shorter wavelength.

The envelope decay rate is expressed by attenuation factors (Q^{-1} value) of seismic waves. We analyzed seismograms of earthquakes around the 2016 Kumamoto earthquake activity and estimated the Q^{-1} values for both intrinsic and scattering attenuation. In order to estimate spatial distribution of the attenuation factors, we improved a method proposed by Del Pezzo et al. (2016). Three dimensional spatial weighting functions have been introduced for estimated Q^{-1} values by Monte-Carlo simulation and estimate the Q^{-1}

structure in the hypocentral area of the 2016 Kumamoto earthquake. The intrinsic attenuation structure drastically changes at the active fault and volcanic region. On the other hand, scattering attenuation is strong at the junction of two major faults. The ripple on the envelope observed many seismograms. We extract arrival time and relative amplitude of the ripple and determined strong heterogeneity by stacking many pairs of station and event. The detected strong heterogeneities were found around the fault junction and surrounding area of the Aso caldera. This characteristic is consistent with that from envelope analysis.

Through the seismic wave analyses in this study, we obtained strong heterogeneous structure around the 2016 Kumamoto earthquake sequence. This result suggests that complex fault behavior associated with large earthquake is controlled by strong heterogeneous structure. In the further study, small scale heterogeneity detecting the present study might contribute to evaluation for the potential of the earthquake occurrence.

Contents

Chapter 1.

Introduction

1.1 Seismic wave attenuation and scattering due to heterogeneous structure of the Earth's interior

The seismic waveform observed at a point consists of waves that reach directly to the observation point from a hypocenter and scattered waves that travel via scatterer and arrive later. Generally, seismic waves attenuate while propagating in the earth. The scattered waves found in the latter part of observed seismogram, which is called "coda wave", are generated by heterogeneities in the earth (Aki, 1969, Sato et al., 2012).

By using the coda wave, it is possible to estimate the heterogeneous structure of the Earth.

Based on the radiative transfer theory, shape of the envelope of seismograms is characterized by parameters that express the heterogeneity such as scattering coefficient, strength of velocity perturbation, correlation length and so on. The envelope ignores the phase information of the wave by taking square amplitude for simplicity. It can be handled as propagation of energy density.

In this study, we analyze by focusing on the average structure that dominates the shape of the entire envelope, and strong inhomogeneity structure that produces a strong peak (ripple) especially on the coda part.

Strong heterogeneity distribution inferred from ripple in coda part of a seismogram of natural earthquake have done by many studies. Nishigami (1991, 1997, 1999) have imaged the relative scattering intensity that is estimated by extracting the part deviating from the theoretical envelope in the observation envelope. Obara (1997) reproduced the part of ripple found in the envelope by the simulation based on two models, which are the hybrid model of the reflector and scatterers and the scattering block model respectively. Asano and

Hasegawa (2004) developed an inversion that can evaluate the spatial variation of the scattering intensity and detected large scattering coefficient zones.

1.2 The 2016 Kumamoto Earthquake

The 2016 Kumamoto earthquake sequence involved mainshock of M7.3 occurred on April 16 following the M6.5 largest foreshock occurred on April 14.

The seismic source mechanism of the mainshock was a strike slip with a tension axis in the nearly north-south direction.

Very extensive active aftershock seismicity ranging from the Kumamoto district in Kumamoto Prefecture to central Oita prefecture was observed.

Especially in the central part of Oita prefecture, the earthquake with estimated magnitude of M5.4 was induced by the mainshock despite the distance of the epicenter being far about 70 km.

The Futagawa fault zone and the Hinagu fault zone exist in the source area of the 2016 Kumamoto earthquake.

The M6.5 earthquake (largest foreshock) on April 14 and a M6.4 earthquake on April 15 occurred near the Hinagu fault. The main shock occurred near the Futagawa fault zone.

Aso volcano is located on the eastern of the Futagawa fault zone, and Kuju volcano is located on the northeast. The earthquake sequence created many surface rupture traces appeared in the hypocentral area (Shirahama et al., 2016). Both left lateral and normal fault slip observed and maximum surface break at some parts are over 2 m around the Futagawa fault. Co-seismic fault slip distribution of the main shock was estimated from co-seismic sensor records around the area by Asano and Iwata (2016). They conclude the large slip area at shallow part of the fault exist a part of the fault, which might be cause of the heavy damage at the resident area.

A large number of seismic stations were deployed by the Group for Urgent Joint Seismic Observation of the 2016 Kumamoto Earthquakes (Shimizu et al., 2016) immediately after the largest foreshock.

The aftershocks of the Kumamoto earthquake occurred in the moderate seismic wave velocity layer with the seismic velocity of Vp ~ 6 km / s, Vs ~ 3.5 km / s, the main shock stated the rupture at the bottom of this seismogenic layer (Shito et al., 2017).

Aizawa et al. (2017) investigated the electric resistivity structure of the

area and revealed the high seismicity of aftershocks occurred to avoid the portion of low resistivity.

Wang et al. (2017) and Komatsu et al. (2017) estimated the total attenuation (intrinsic attenuation + scattering attenuation) of the S wave, and found that the regions with large attenuation exist along the Futagawa fault zone and Hinagu fault zone.

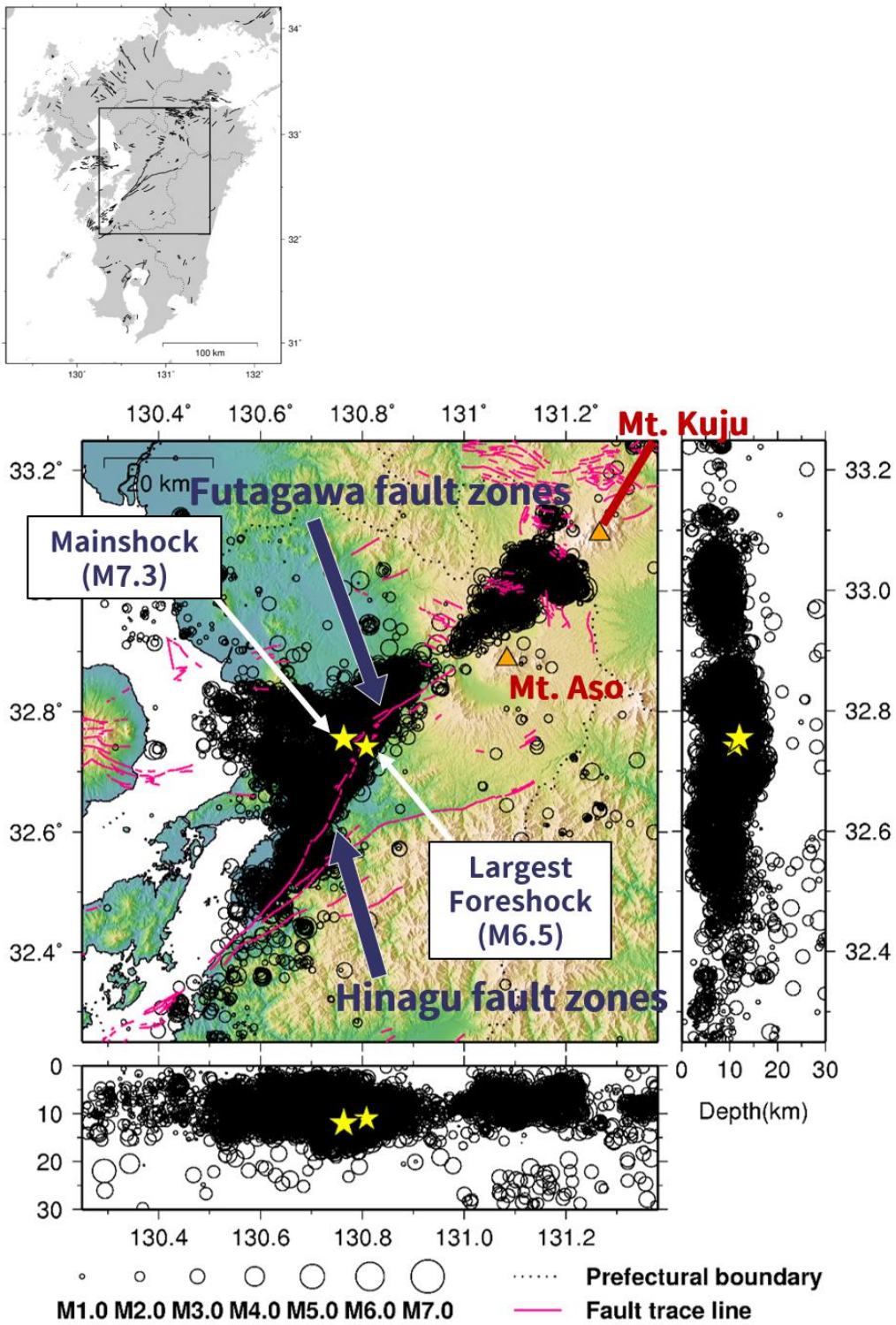

Figure 1.2.1 Map of focal area of the 2016 Kumamoto earthquake. Circles shows the location of the hypocenter and its size depends on the magnitude from the occurrence of the largest foreshock until December 2017.

1.3 Aim of this study

The attenuation of seismic waves is divided into intrinsic attenuation and scattering attenuation.
Intrinsic attenuation represents that the wave energy is converted to the thermal energy by friction and scattering attenuation represents that the wave energy is dissipated due to inhomogeneity of medium.
In this study, intrinsic attenuation and scattering attenuation are separately estimated.
We estimate the seismic attenuation structure in the source region of the 2016 Kumamoto earthquake by combining the spatial distribution of intrinsic attenuation, scattering attenuation, and strong scatterers that produce ripples of observed envelopes.
We proposed a new method for mapping intrinsic attenuation and scattering attenuation on three dimensional space.
Estimating seismic attenuation structure is also important from the viewpoints of numerical simulation of seismic wave field (ex., Earthquake Early Warning)
Seismic attenuation structure strongly reflects the existence of structure boundary and magma / fluid, hence it is important for understanding the structure of Earth's crust.
In addition, the seismic structure of Earth's crust is largely related to the occurrence of the earthquake.
By analyzing the seismic attenuation in the source region of the 2016 Kumamoto earthquake, it is expected that new knowledge about this earthquake will be obtained.

Chapter 2.

Analysis

2.1 Data and basic processing

2.1.1 Observation data

The study area is the source region of the 2016 Kumamoto earthquake (Fig. 2.1.1).
Seismic activity in this area is one of the highest in Kyushu Island, Japan. Especially, many earthquakes observed around Kumamoto City, Futagawa fault, and Hinagu faults as seen in Fig. 1.2.1. In this area, many temporal seismic stations have deployed. Seismic data is transmitted to the center or on-site recorded.
As seen in Fig 1.2.1, the hypocenter distribution is not homogeneous. For obtaining stable solution in an estimation of the heterogeneous attenuation structure, we need to consider both distribution of station and event. Therefore, we select events whose distribution is almost homogenous in the target area from the earthquake catalog.
Waveforms analyzing in this study are required to have sufficient signal strength because we use the later part of seismograms for the estimation. In addition, the amplitude of seismogram for an earthquake with large magnitude might be out of recording range in the instruments. In this study, we set a range in magnitude used in this study from 2 to 4.
We use seismic waveform data recorded from January 2010 to June 2016, including aftershock data of the 2016 Kumamoto earthquake obtained by the Group for Urgent Joint Seismic Observation of the 2016 Kumamoto Earthquakes (Shimizu et al., 2016).
Total number of seismic events and stations are 1732 ($2.0 \leqq M \leqq 4.0$, 0 km < depth < 20 km) and 81, respectively.

2.1.2 Basic processing

Modeling envelope of seismogram

As described above, earthquakes in the optimal magnitude range are selected. Figure 2.1.x shows an example of observed envelopes for the events located in the target area. The envelope is obtained from band-pass filtered seismogram of 8 Hz. We can see the amplitude decrease with increasing lapse time. This decay could be modeled by a scattering theory. At the same time, parts with large amplitude, which seems like "ripple", are found in the envelope. In this study, we attempt to model both the features of the envelope (i.e. envelope decay and ripple).

First, we consider envelope shape and decay of the seismogram. We adopt a solution based on the approximate analytical equation of radiative transfer theory (Paasschesns, 1997) to explain the feature of the observed envelopes,

$$E(r,t|f) \approx \frac{W_0(f)e^{-ct\alpha_t}}{4\pi r^2 c}\delta\left(t-\frac{r}{c}\right) + W_0(f)H\left(t-\frac{r}{c}\right)\frac{\left(1-\frac{r^2}{c^2t^2}\right)^{1/8}}{\left(\frac{4\pi ct}{[3\alpha_t B_0]}\right)^{3/2}}$$

$$\times e^{-ct\alpha_t}G\left(ct\alpha_t B_0\left[1-\frac{r^2}{c^2t^2}\right]^{3/4}\right), \qquad (2.1)$$

$$G(x) \approx e^x\sqrt{1+\frac{2.026}{x}},$$

where E is the density of the seismic energy, r is the distance between source and station, t is the time, f is the frequency, W_0 is the source radiated energy, c is the seismic velocity (in this case S wave velocity), δ is the Dirac delta function, α_t is the total attenuation coefficient, H is the Heaviside function and B_0 is the seismic albedo (scattering attenuation/total attenuation)

Next, we consider the energy density at ripple part in the envelope. Single scattering model (see in the text by Sato et al., 2012) can be adopted for this part because the amplitude is relatively large. The energy can be written by the following formula;

$$E_c = (x,r,t|f) = W_0(f)\frac{g(x)\Delta V}{(4\pi)^2 {r_a}^2 {r_b}^2}exp(-ct\alpha_t)\delta\left(t-\frac{r_a+r_b}{c}\right)\cdot I(f), \qquad (2.2)$$

where E_c is the energy from volume ΔV where scatterers distribute, the volume is located at position x. g(x) is the coefficient of the scattering and r_a, r_b are the distance from the source to the volume and from the scatterers to the observation point respectively.

Data processing sequence

In this study, we measure decay of the observed envelope and amplitude at the ripple part in order to estimate scattering property in the target area. The parameters characterizing the property are solved in several frequency bands. Practical waveform processing is performed by the following procedure.

First, we apply the band-pass filter to the observed velocity seismograms. The central frequencies of the filter (fc) are 2, 4, 8, and 16 Hz, respectively. Band width of the filter set range from fc/2 to 3fc/2. Next, we take the mean square (MS) of amplitude of the filtered seismograms with a smoothing time window with length of 2/fc seconds. To normalize the effects of both the source radiating energy and the observation site amplification, we calculate a ratio of the MS envelope to its average value during an analyzing time window. The time window used in this study starts from 2 s after direct S wave arrival time and ends 30 s after origin time. However, the time window length is shortened until signal to noise ratio greater than two. This setting for the start time of the window is for avoiding direct S wave amplitude that is strongly affected by radiation pattern at the source. The end time of the window limits spatial volume contributing to the scattered waves, which is set to contain the target depth that is entire crust.

As described above, the envelope shape and decay are modeled by the empirical multiple scattering model. The attenuation parameters (i.e. α_t, B_0 in equation 2.1) are obtained by comparing synthetic envelopes with observed one. We calculate residual between logarithmic observed envelope and synthetic one for a pair of α_t and B_0 and then search the optimal parameter pair among a probable range of the pair. The range of them are α_t=0.01 – 0.5, B_0=0.05 – 0.95, respectively. We iteratively apply this procedure to all event and station pairs. The dataset of the attenuation parameters that can explain the observed envelope for the event and station pairs are created through the processing.

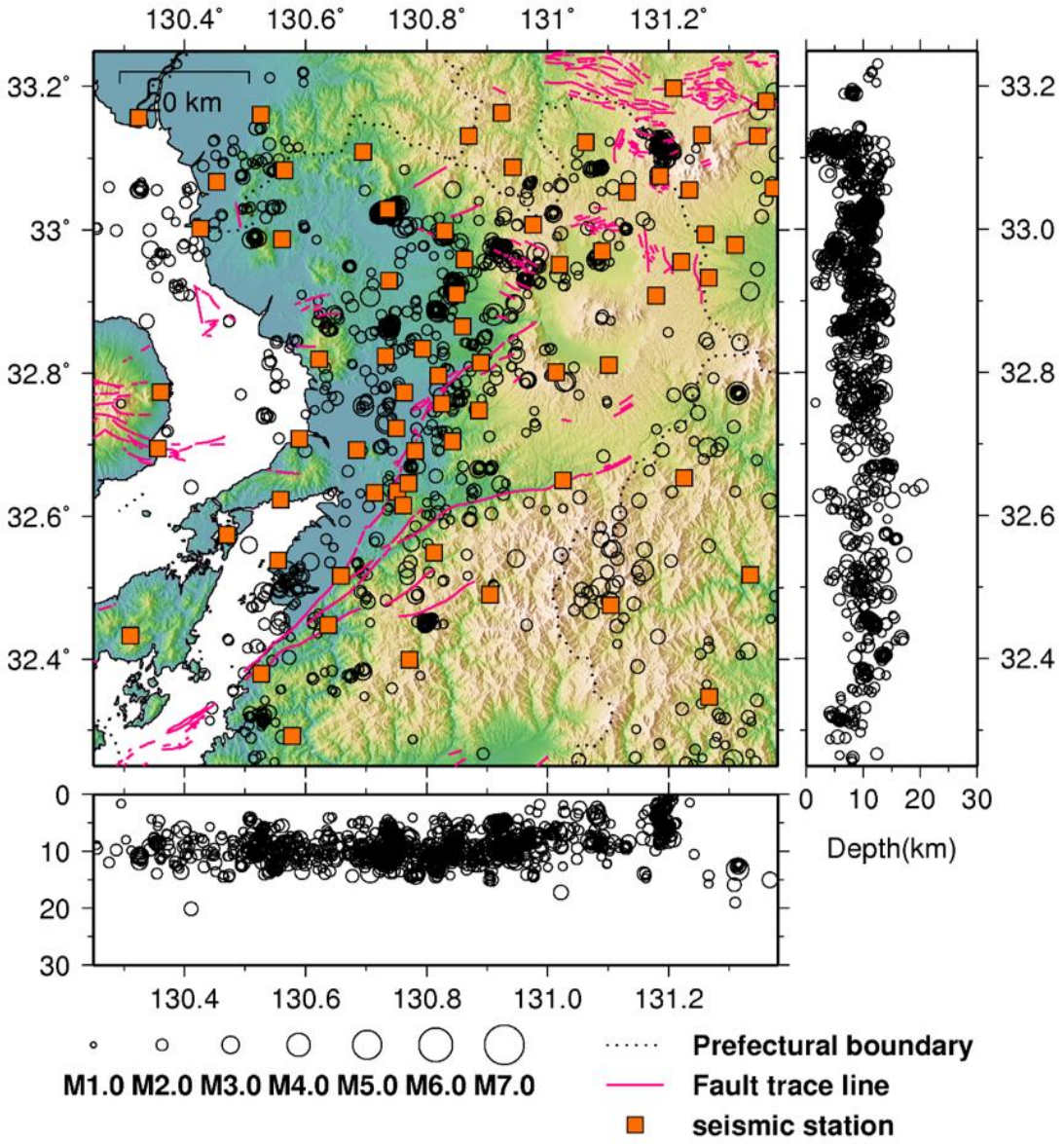

Figure 2.1.1 Map view of used seismic events and seismic stations. Solid circles show the location of the hypocenter from January 2010 to June 2016.

2.2 $Q_{i,s}^{-1}$ mapping

Intrinsic and scattering attenuation (Q_i and Q_s) are described by the estimated attenuation parameters (α_t, B_0) as following formula.

$$B_0 = \frac{{Q_s}^{-1}}{({Q_i}^{-1}+{Q_s}^{-1})} \qquad \alpha_t = \frac{2\pi f}{c}({Q_i}^{-1} + {Q_s}^{-1}) \tag{2.3}$$

Therefore,

$${Q_i}^{-1} = \frac{c}{2\pi f}\alpha_t(1-B_0) \qquad {Q_s}^{-1} = \frac{c}{2\pi f}\alpha_t B_0 \tag{2.4}$$

Spatial variation of the attenuation factors is estimated from the dataset of the parameters for all station and event pair. Del Pezzo et al. (2016) has developed a method to obtain the variation by spatial averaging with two dimensional weighting function defined by epicentral distance. They successfully obtained the attenuation $Q_{i,s}^{-1}$ structure around volcanic island. However, it could not apply to the dataset with large depth variation of hypocenter distribution. Three dimensional weighting function was explored in Del Pezzo et al. (2018), but it doesn't correspond to the Paasschens's equation.

We extend their method that is applicable to estimation of Q_i and Q_s maps on three-dimensional space with appropriate space-weighting functions to estimate realistic seismic attenuation structure.

Del Pezzo et al. (2016) proposed an approach using numerical simulation to solve the radiative transfer equation that models seismic energy envelopes for both highly and rarely inhomogeneous medium. Spatial density of paths and spatial density of energy particle collisions were obtained using Direct Simulation Monte Carlo method (Yoshimoto, 2000), and they were treated as space-weighting functions of intrinsic attenuation and scattering attenuation, respectively. The numerical simulation of the space-weighting functions is highly time consuming. Therefore, they assume an identical pattern for both intrinsic and scattering attenuation, and found approximate 2D space-weighting function of best fitting with a large number of observed envelopes by trial-and-error.

However, the approximate 2D space-weighting function has the

following problems:
We cannot capture the three-dimensional change of the structure.
The approximate 2D space-weighting function assuming the hypocenter depth of 0 km cannot be applied for natural earthquakes data with hypocenter depths ranging from 0 to 20 km used in this study. Therefore, we did not use the approximate 2D space-weighting function, but we straightforwardly calculated the 3D space-weighting function by Monte Carlo Simulation for all the envelope data.
This has the merit that there is no deviation from the actual weight distribution unlike the use of the approximate 2D space-weighting function.
We achieved the extremely time consuming calculation by using the MPI parallel computation technique.
Q_i^{-1} and Q_s^{-1} at a point x are estimated by taking weighting average of attenuation factor among all station – event pairs as following formula.

$$Q_{i,s}{}^{-1}[x,y] = \frac{\sum_j \left(Q_{i,s}{}^{-1}{}^{j}\right) W_j[x_k, y_k]}{\sum_j W_j(x_k, y_k)}, \qquad (2.5)$$

where $Q_{i,s}^{-1}$ is attenuation factor of j-th event – station pair for either intrinsic energy loss or wave scattering. Wi is spatial weighting factor calculated for j-th pair. The spatial weighting factors for Q_i^{-1} and Q_s^{-1} are obtained from the spatial density of paths and spatial density of energy particle collisions using the numerical simulation (i.e. Direct Simulation Monte Carlo method), respectively. The weighting factors are assigned to spatial points where scattered energy contributes to the envelope within the lapse time window for each event – station pair. Figure 2.2.1 show examples of spatial weighting factors for intrinsic and scattering attenuation factor.

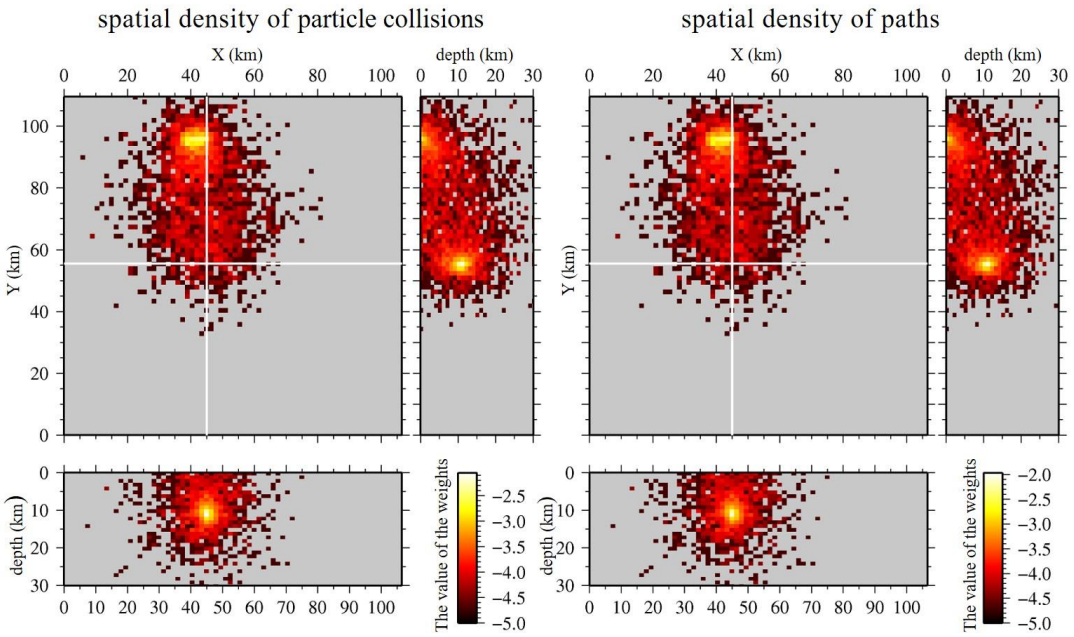

Figure 2.2.1. Spatial weighting factor distribution along a line through hypocenter and station. Left and right panels show the logarithm of values of the spatial density of paths and particle collisions for weighting factor of Q_i^{-1} and Q_s^{-1}, respectively.

The figure shows that large weighting factor distributes around source and station locations. This is consistent to feature expected from the radiative transfer theory. The factor for Q_i^{-1} is slightly different from for Q_s^{-1}. The weighting factor distribution strongly depend on the hypocenter depth as seen in Fig. 2.2.1. This indicates that 3-D weighting factor is required to discuss the $Q_{i,s}^{-1}$ structure from data of earthquakes with wide depth range.

We perform the simulation for every event – station pairs using parameters α_t and B_0 estimated in the envelope fitting described above and determine spatial weighting functions.

2.3 Checkerboard Resolution Test

Spatial resolution of Q_i^{-1} and Q_s^{-1} is affected by the distribution of the event – station pairs. Checkerboard Resolution Test (CRT) is often adopted to evaluate the spatial resolution in many studies (e.g. Shito et al., 2017 for velocity tomography). We perform CRT to examine the resolution of the spatial images of Q_i^{-1} and Q_s^{-1} estimated from real dataset used in this study. The CRT test confirms solved images from artificial dataset that contains Q_i^{-1} and Q_s^{-1} values calculated from modeled structure and the pairs. The modeled structure is designated spatial variation with checkerboard pattern.

The dataset in the testing procedure is generated as following steps:

(1) A model structure with checkerboard pattern is defined.

(2) Numerical 3D spatial weighting functions are calculated for all the observed pairs.

(3) Observed Q_i^{-1} and Q_s^{-1} for a pair in the test calculated by taking summation of product of spatial weighting factor and given value by the modeled structure within the target area.

Then we apply the above described procedure to estimate spatial distribution of attenuation factor.

In this resolution test, we set a modeled structure with checkerboard pattern shown in Fig. 2.3.1. The pattern composed by $Q_{i,s}^{-1}$ values of 0.001 and 0.1 with 15 km interval is assigned in the test. These values correspond to upper and lower values of the pairs in the dataset of present analysis. The block interval almost coincides to the average station separation in the target area.

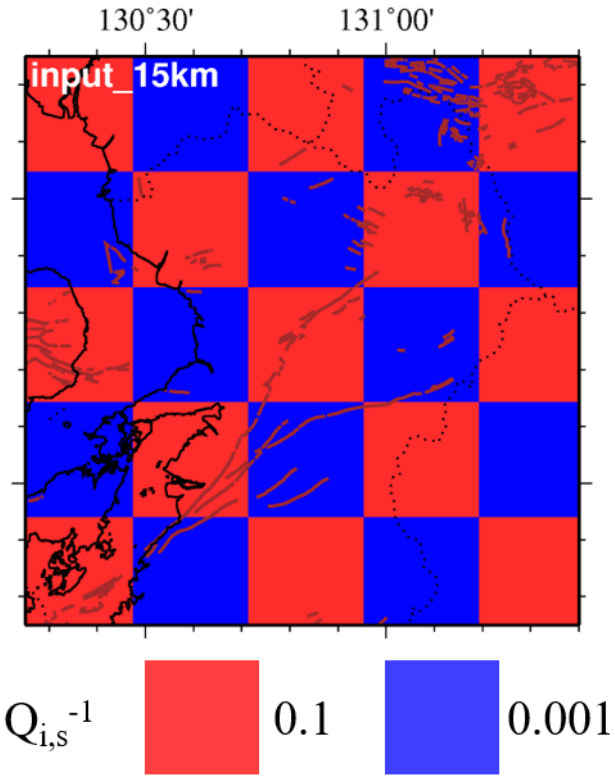

Figure 2.3.1 $Q_{i,s}^{-1}$ structure adopted in CRT. Black and white colors show the assigned $Q_{i,s}^{-1}$ values of 0.001 and 0.1, respectively.

2.4 Strong scatterer

In this section, we discuss the “ripple” found in the observed envelope. The ripple is composed by scattered wave with larger amplitude than smoothed envelope that could be attributed to averaged structure in the scattering shell. The amplitude in a ripple part is calculated based on formula (2.2). However, the scattering strength for scattered wave contributing to the ripple amplitude is difficult to estimate because the volume size of the distributing scatterers and the strength cannot be separated from each other. Therefore, we only estimate the location of the strong scatterers in the target area.

Location of volume containing strong scatterers is determined by coordinates of source and receiver, and travel time of the strong scattered waves based on our assumption that the energy at the ripple part consists of single scattered waves.

The scattering shell defined by the single scattering model is obtained by using the travel time of ripple for a source and receiver pair (as schematically shown in Fig.2.4.1). We consider a spatial likelihood function that constant value is assigned in the scattering shell with thickness dr. dr is equal to product of velocity in the medium and time length of the ripple. The minimum time length is 2/fc, where fc is central frequency of a band pass filter applying to the observed seismogram. By superimposing all the obtained likelihood functions and searching spatial peaks of the function, we obtain locations of the strong scatters in the target region.

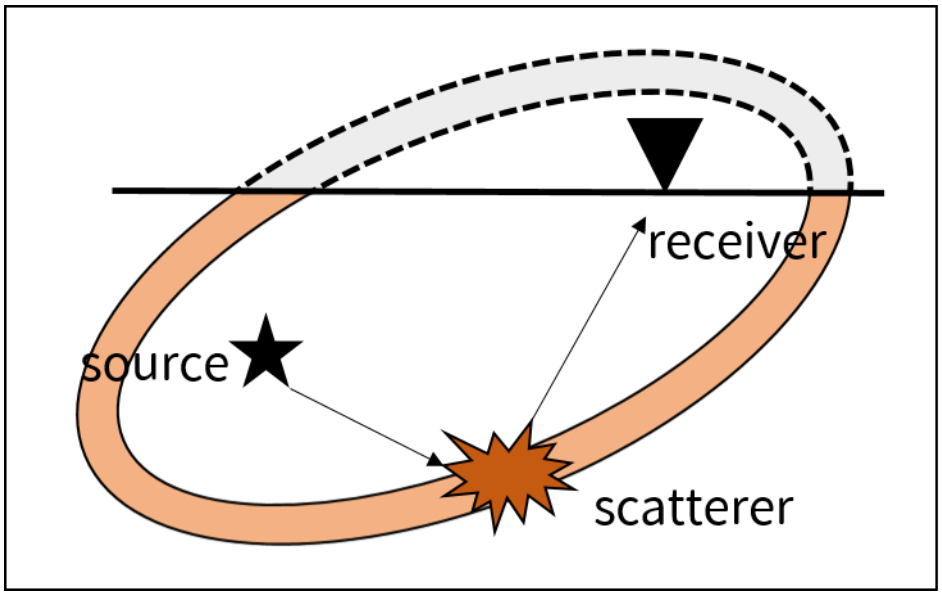

Figure 2.4.1 Conceptual view of the detecting scatterer. The scatterer is on the scattering shell of a certain travel time.

From an observed seismogram, we extract ripple part and its travel time to determine the spatial function. First, we calculate the theoretical envelope for a hypocenter - observation point pair data from the attenuation parameter (α_t, B_0) estimated in chap. 2.1. Ripple parts are extracted from the observed envelope by comparing with the theoretical envelope. The condition for the extraction is that the energy at the observed envelope is greater than six times of the theoretical one. The condition is adjusted to provide optimum image that scatterer distribution does not become blurred.

Chapter 3.

Result

3.1 Resolution test

CRT is performed for the real dataset used in this study by the procedure described in the section 2.3. We generated test dataset by using parameters of the practical event – station pairs, time window length for each frequency band. In this test, we adopted two dimensional attenuation structure with checker board pattern in horizontal direction (see 2.3). The results for Q_i^{-1} and Q_s^{-1} at depth ranges of every 2 km are shown in Fig. 3.1.1 – Fig. 3.1.27.
Spatial resolution in the estimation of Q_i^{-1} and Q_s^{-1} can be evaluated by pattern recovering of the result from the given checkerboard structure. The results for Q_i^{-1} structure reveal that the spatial pattern is recovered in the depth ranges existing station and events. There is no significant difference in the resolution for the entire frequency bands. However, the pattern is not clear at the southern part of the target area where the total weight factor is small. In addition, the CRT results imply that results in Q_i^{-1} estimation for the real data at deeper range than 20 km is not applicable for discussion about spatial variation.
Generally speaking, Q_s^{-1} spatial pattern in the test shows similar result to that for Q_i^{-1}. The result for Q_s^{-1} reveals better recovering than for Q_i^{-1}. This difference could be attributed to discrepancy of spatial pattern of the weighting functions for Q_i^{-1} and Q_s^{-1}.

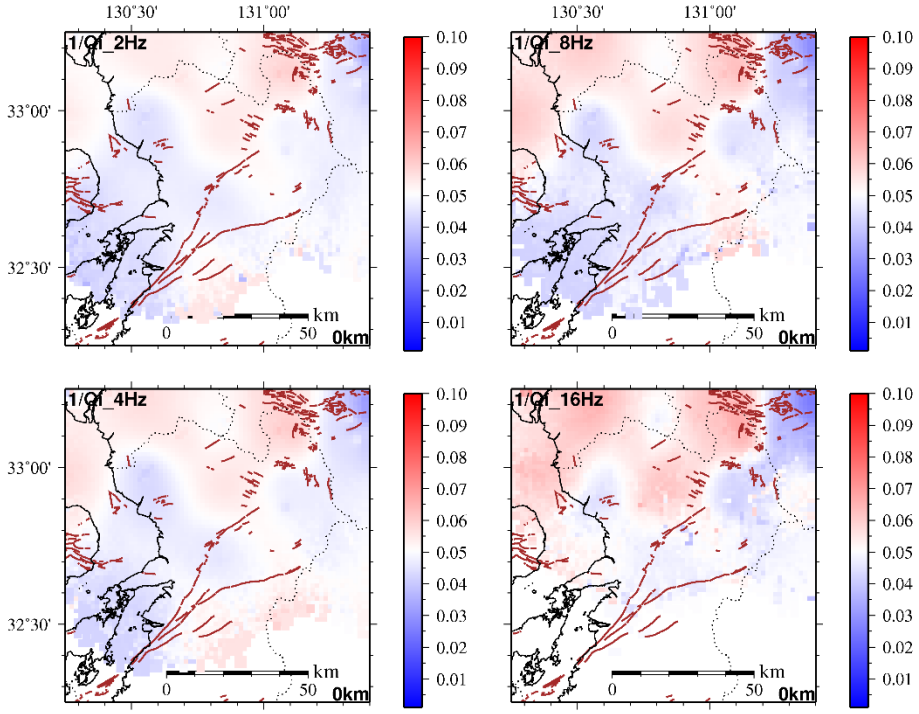

Figure 3.1.1 Map showing Q_i^{-1} distribution by the checkerboard resolution test at depth of 0 km. The result at four frequency ranges are displayed. Colors in the map indicates Q_i^{-1} value as shown in the scale bar at the left of the map.

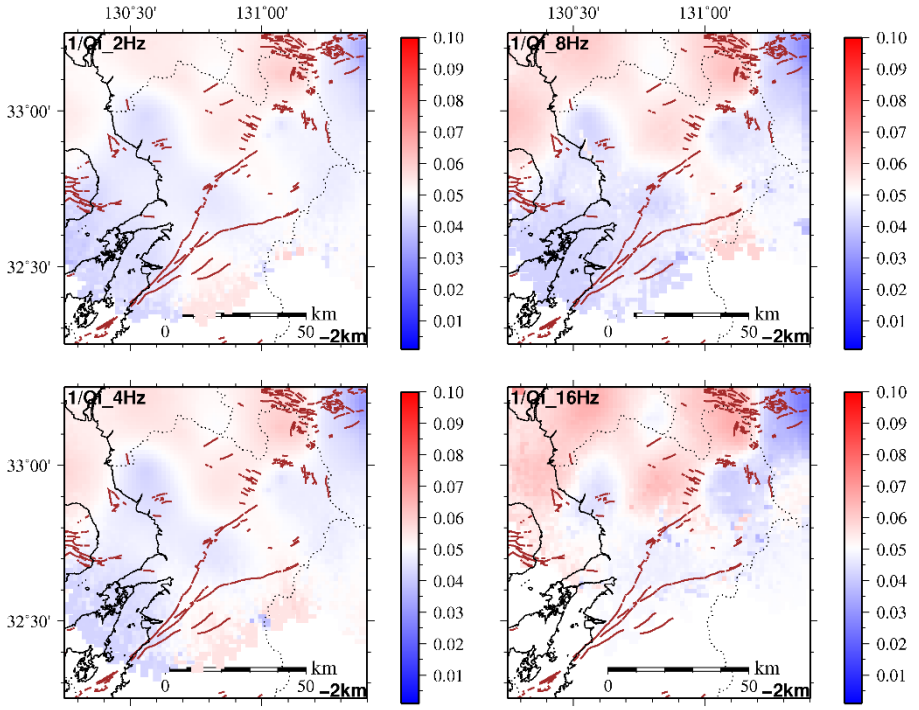

Figure 3.1.2 Same as Fig. 3.1.1 except depth = 2 km.

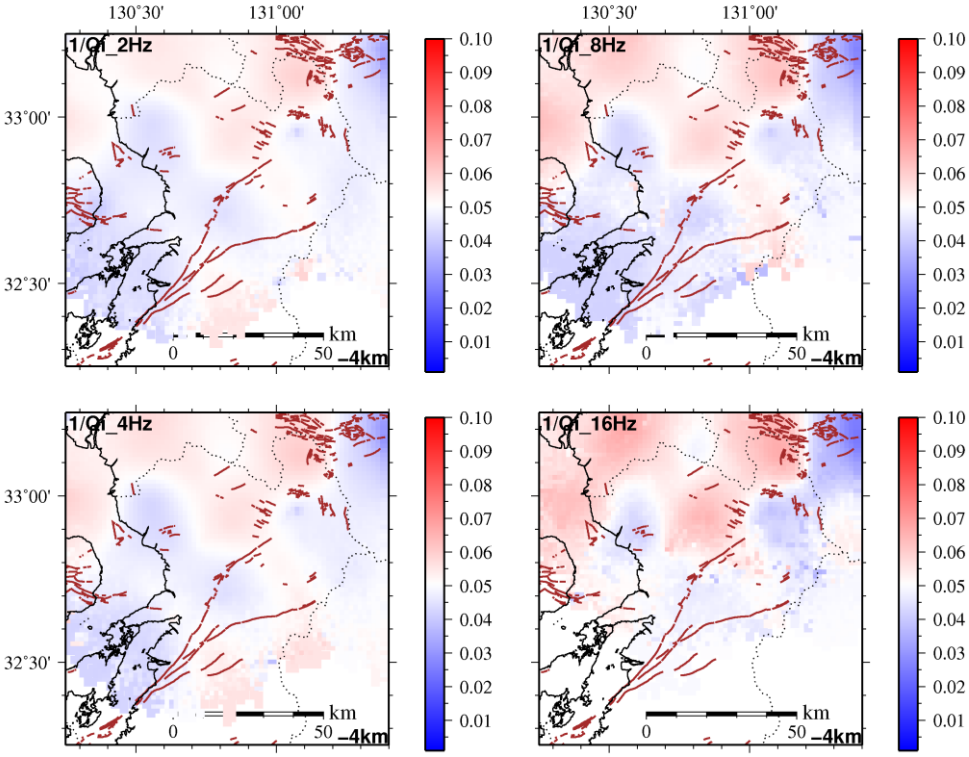

Figure 3.1.3 Same as Fig. 3.1.1 except depth = 4 km.

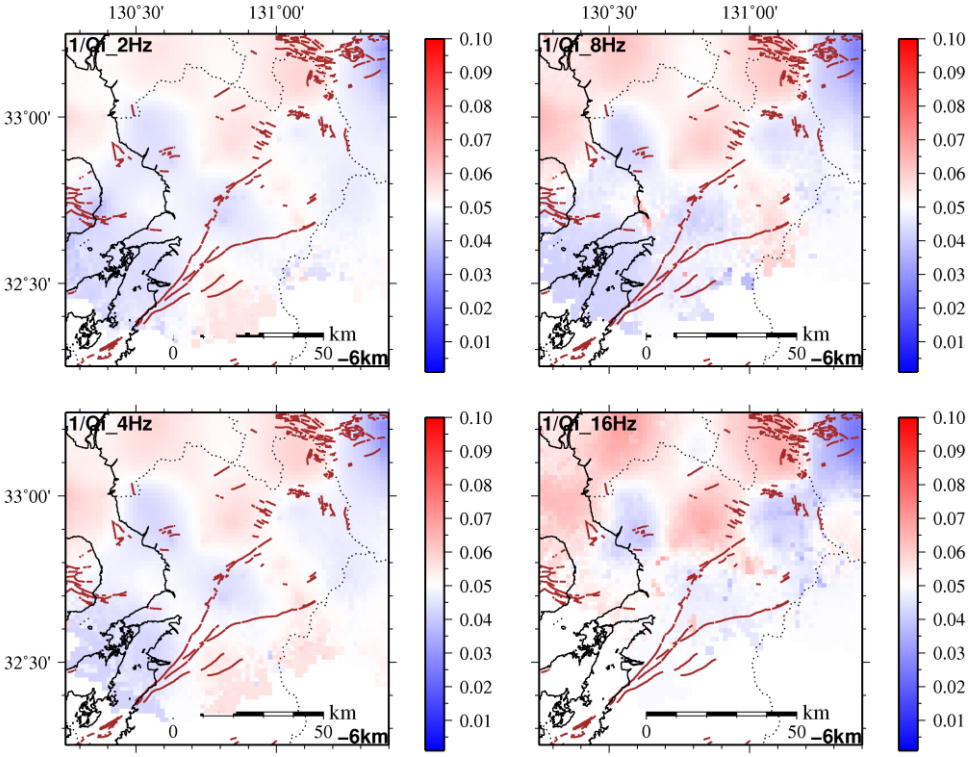

Figure 3.1.4 Same as Fig. 3.1.1 except depth = 6 km.

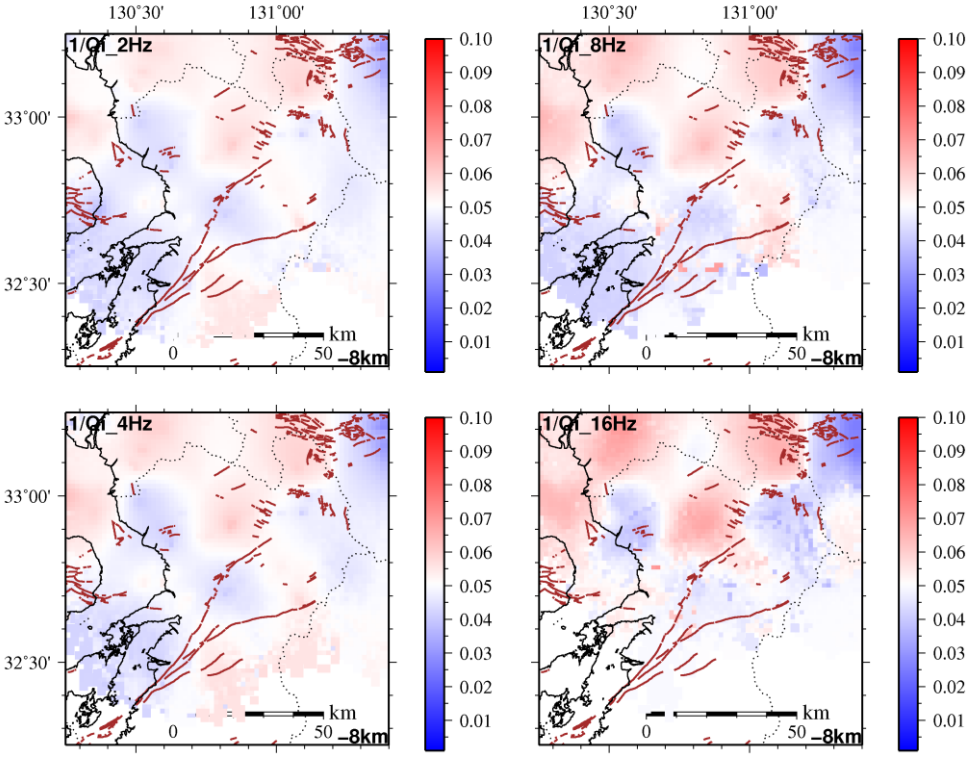

Figure 3.1.5 Same as Fig. 3.1.1 except depth = 8 km.

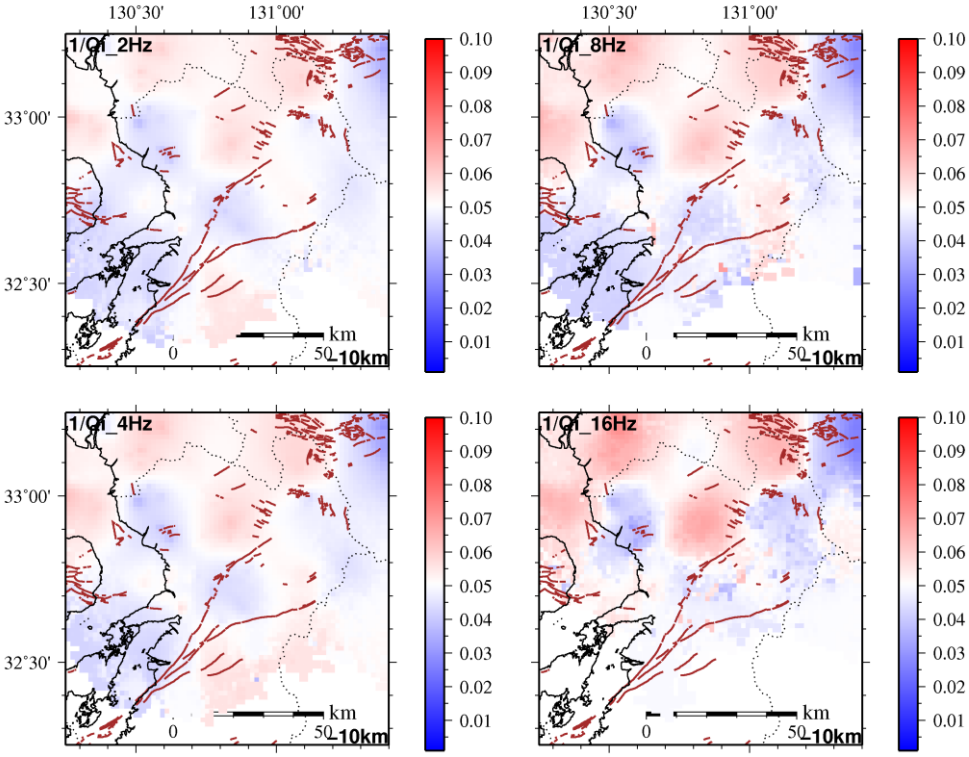

Figure 3.1.6 Same as Fig. 3.1.1 except depth = 10 km.

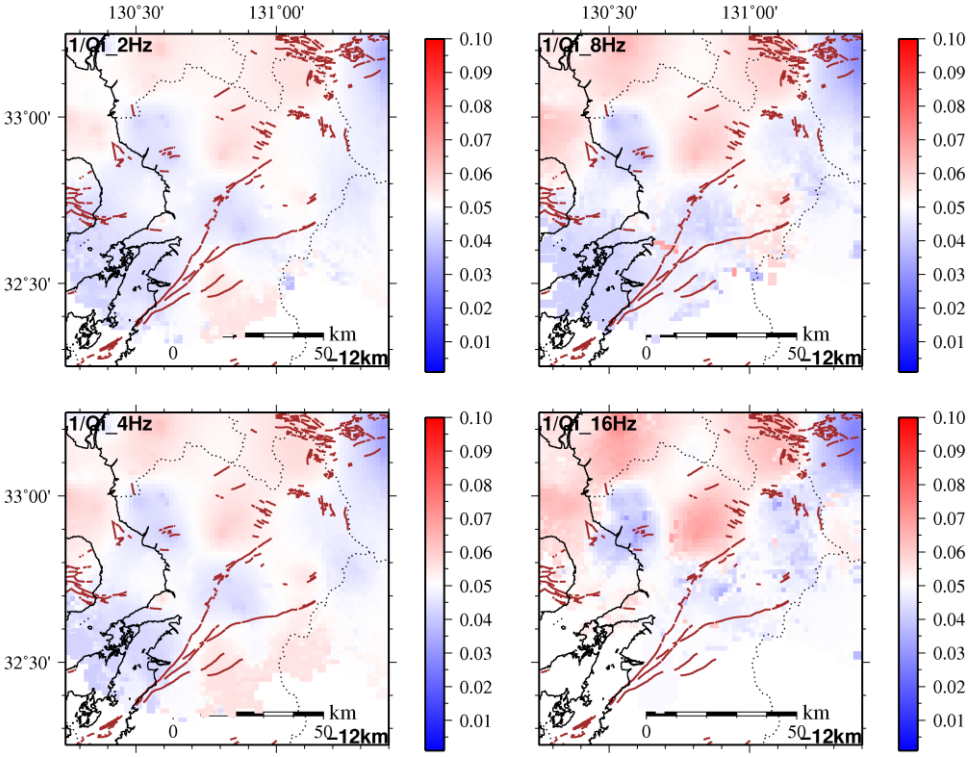

Figure 3.1.7 Same as Fig. 3.1.1 except depth = 12 km.

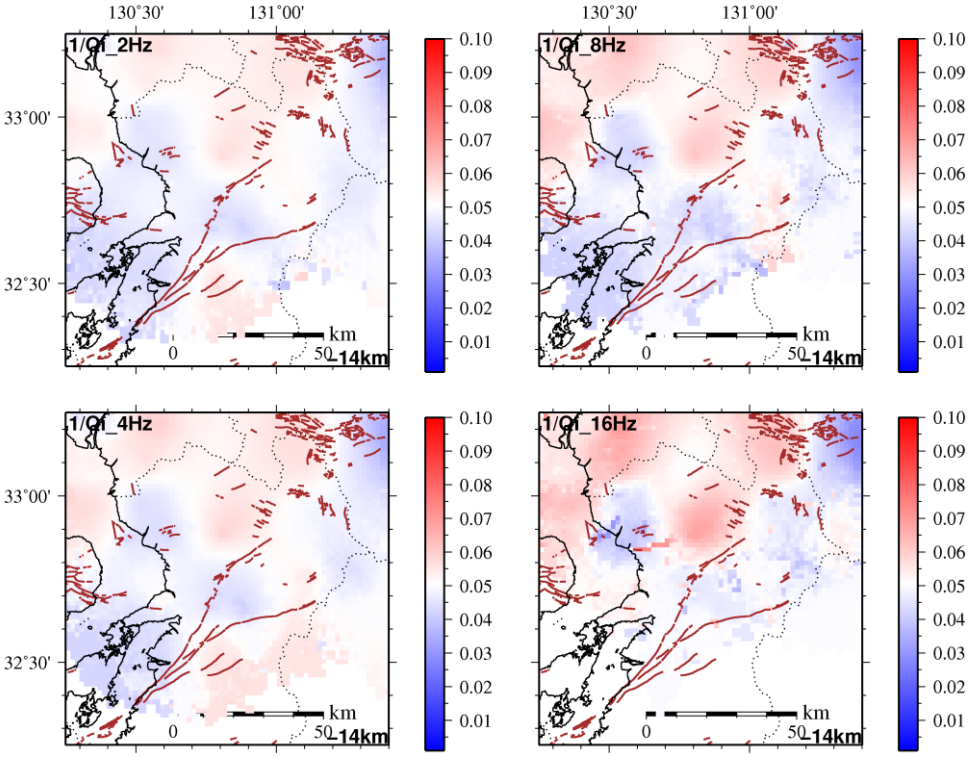

Figure 3.1.8 Same as Fig. 3.1.1 except depth = 14 km.

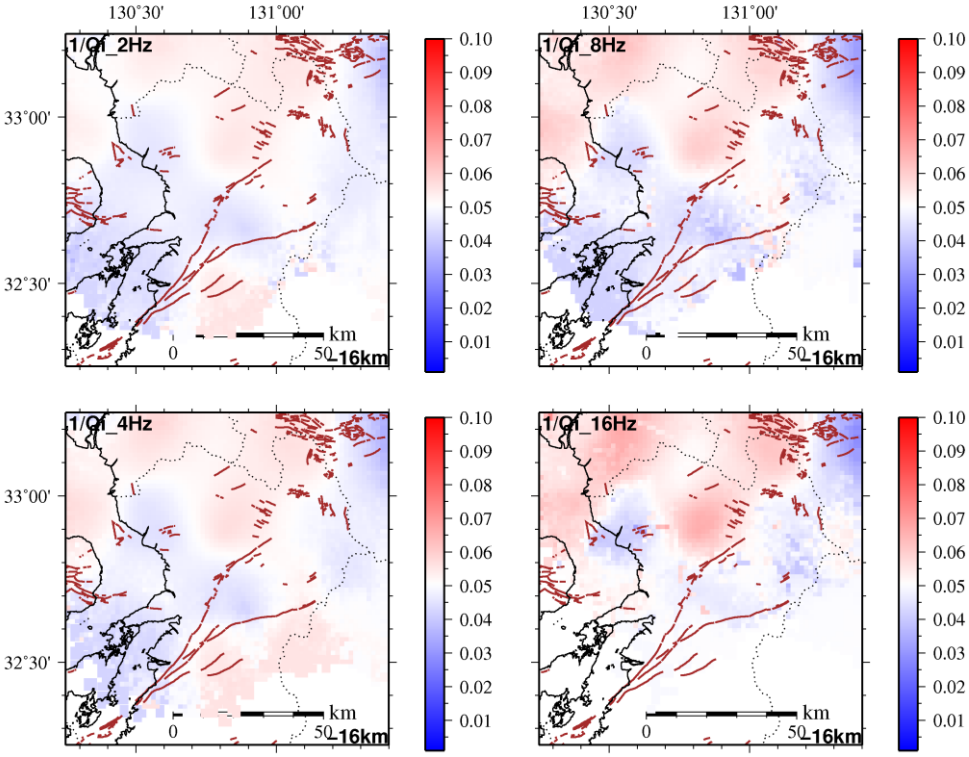

Figure 3.1.9 Same as Fig. 3.1.1 except depth = 16 km.

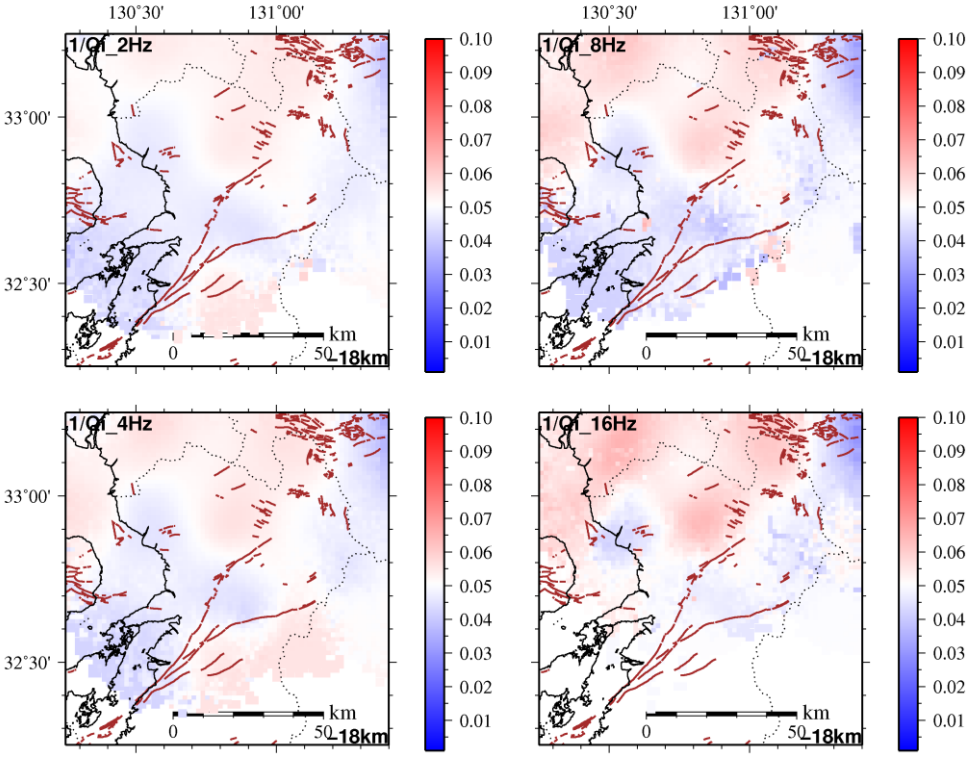

Figure 3.1.10 Same as Fig. 3.1.1 except depth = 18 km.

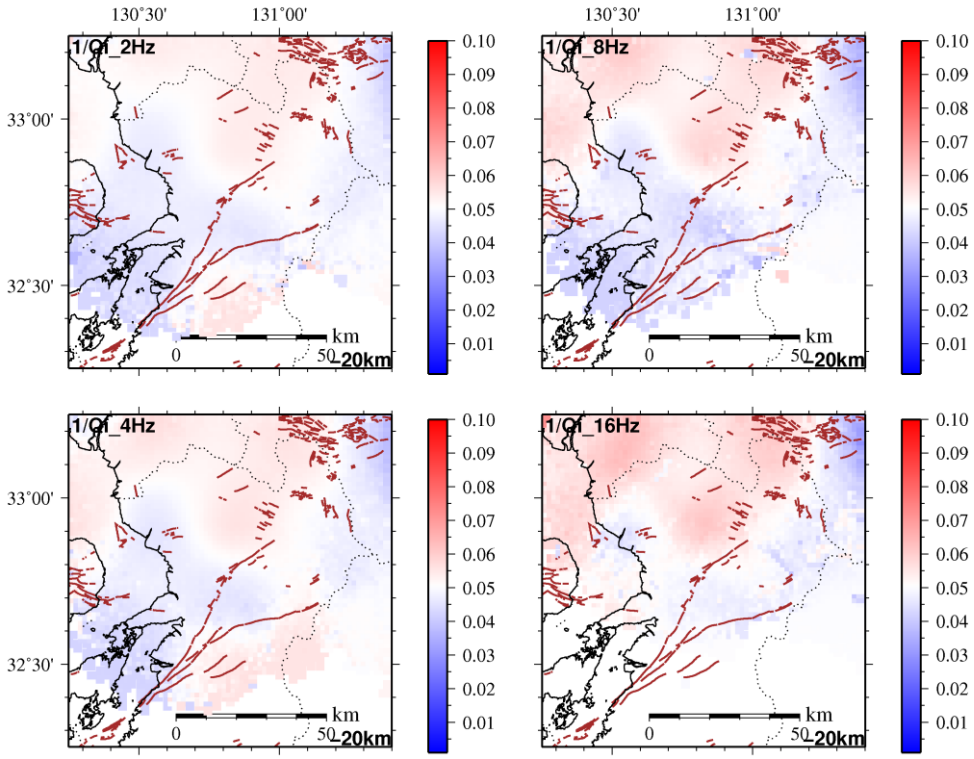

Figure 3.1.11 Same as Fig. 3.1.1 except depth = 20 km.

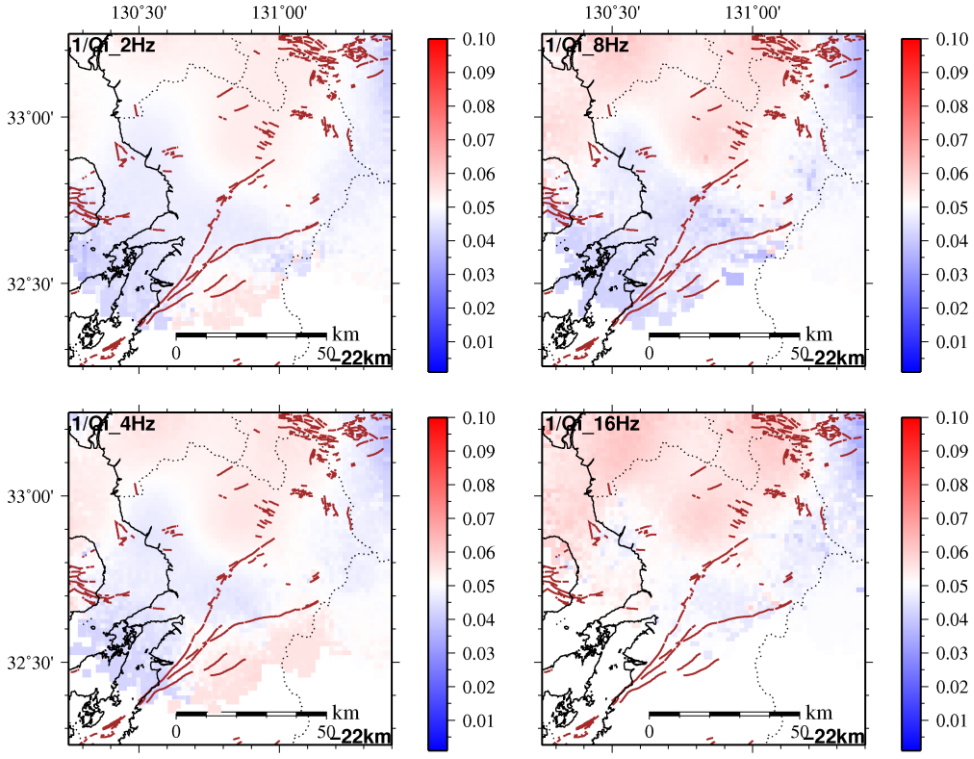

Figure 3.1.12 Same as Fig. 3.1.1 except depth = 22 km.

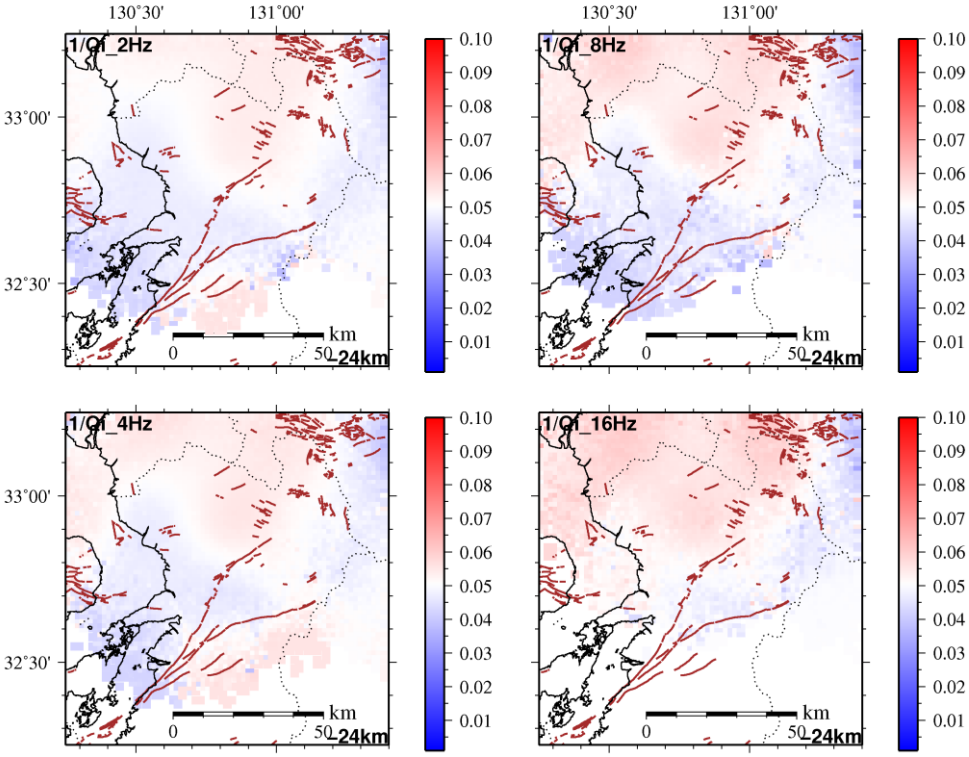

Figure 3.1.13 Same as Fig. 3.1.1 except depth = 24 km.

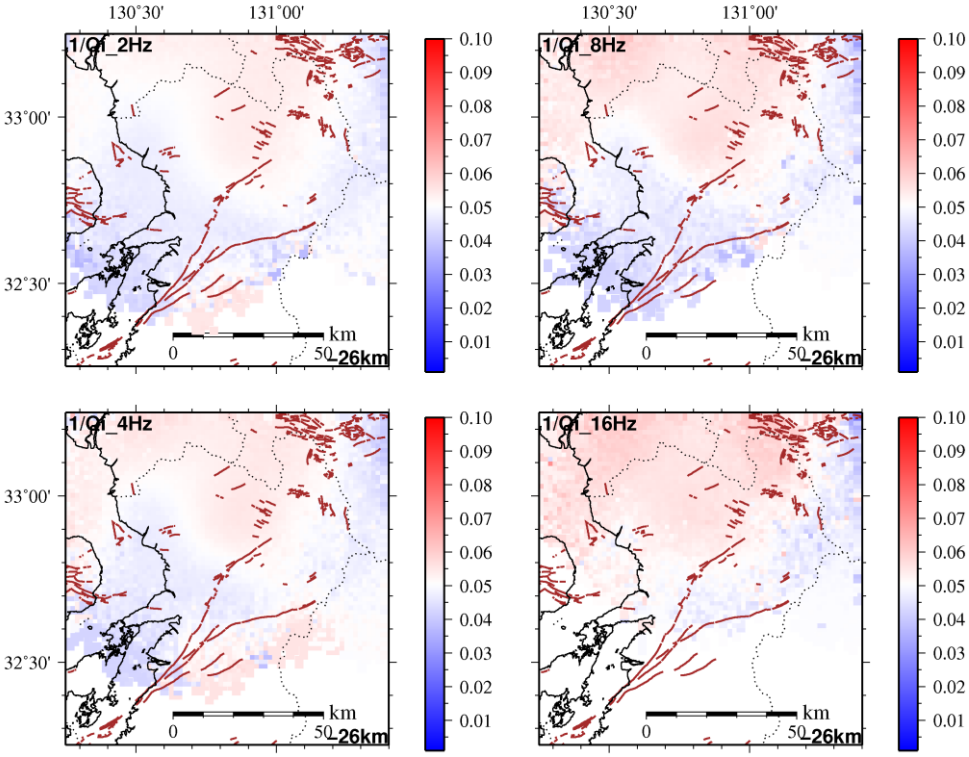

Figure 3.1.14 Same as Fig. 3.1.1 except depth = 26 km.

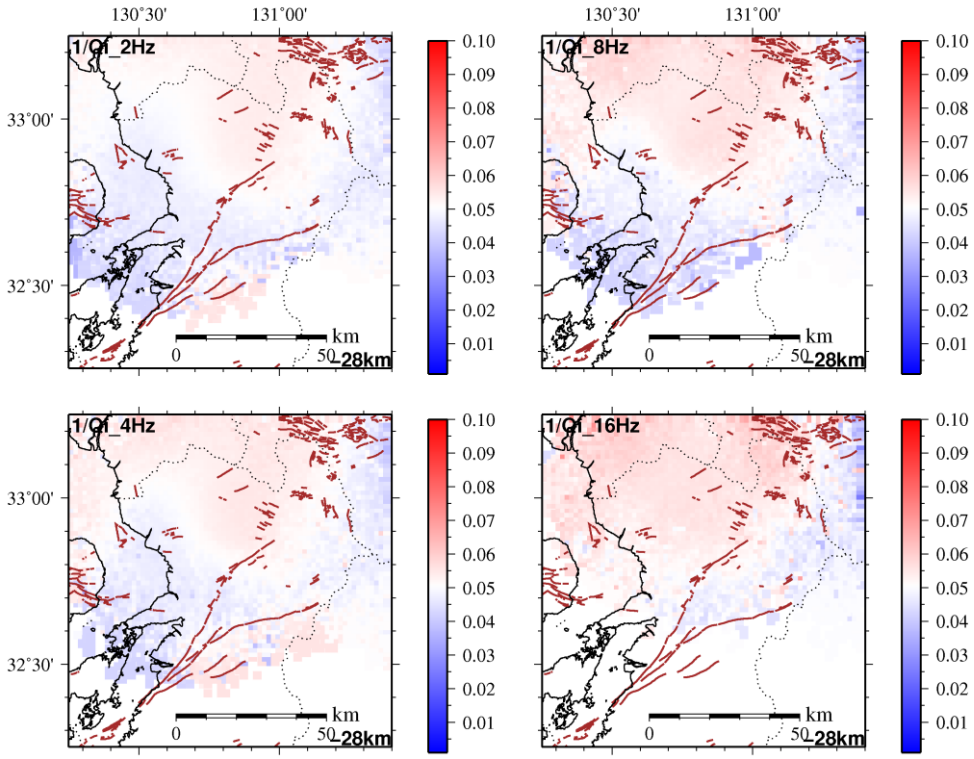

Figure 3.1.15 Same as Fig. 3.1.1 except depth = 28 km.

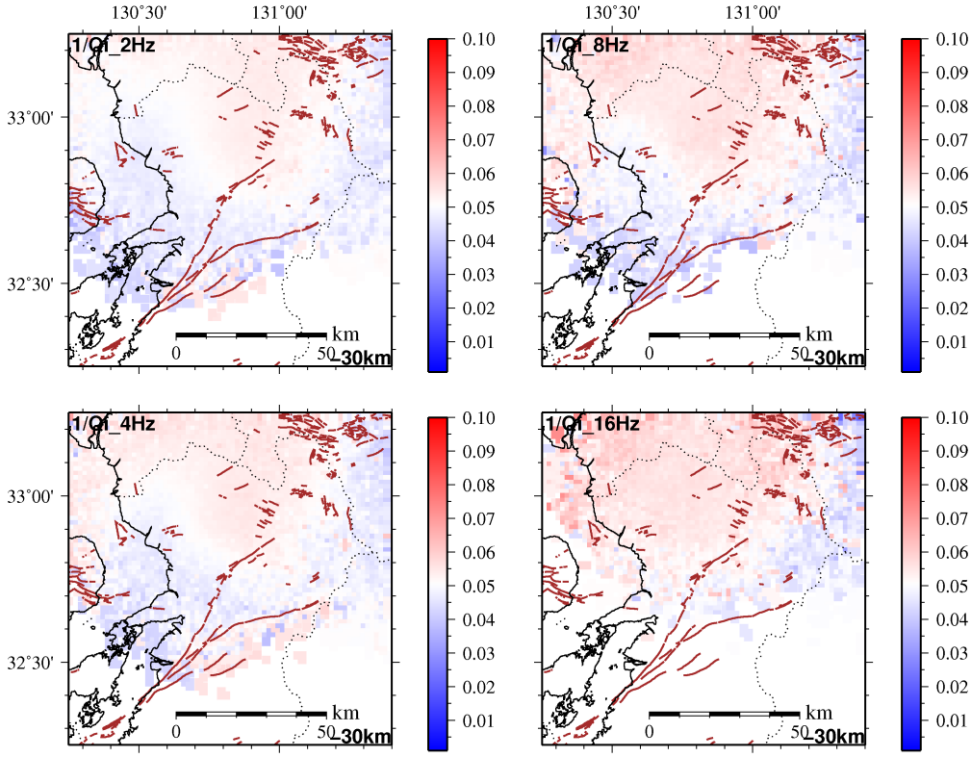

Figure 3.1.16 Same as Fig. 3.1.1 except depth = 30 km.

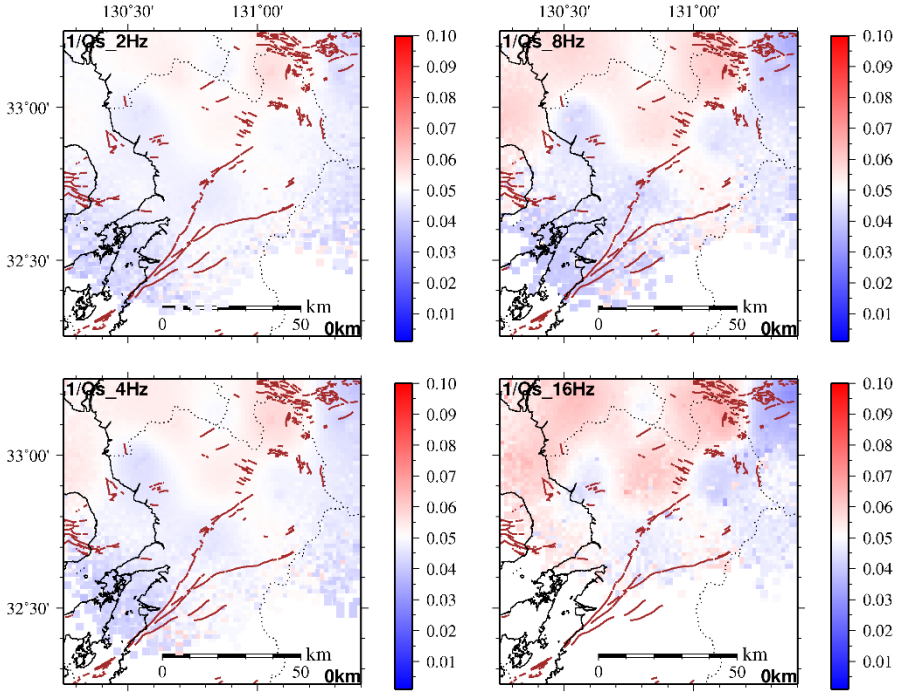

Figure 3.1.17 Map showing Q_s^{-1} distribution by the checkerboard resolution test at depth of 0 km. The result at four frequency ranges are displayed. Colors in the map indicates Q_s^{-1} value as shown in the scale bar at the left of the map.

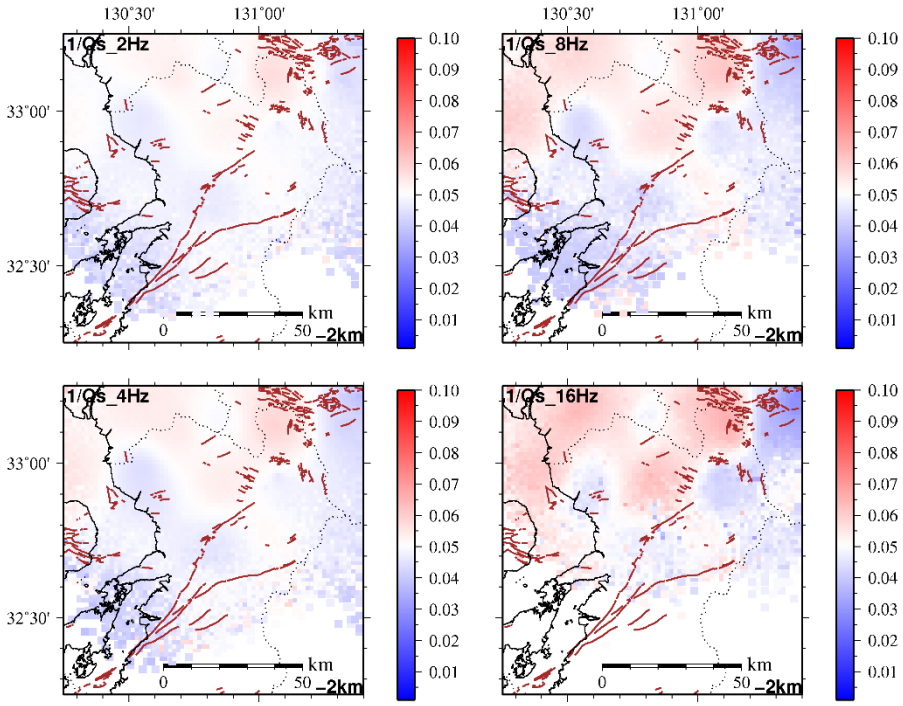

Figure 3.1.18 Same as Fig. 3.1.17 except depth = 2 km.

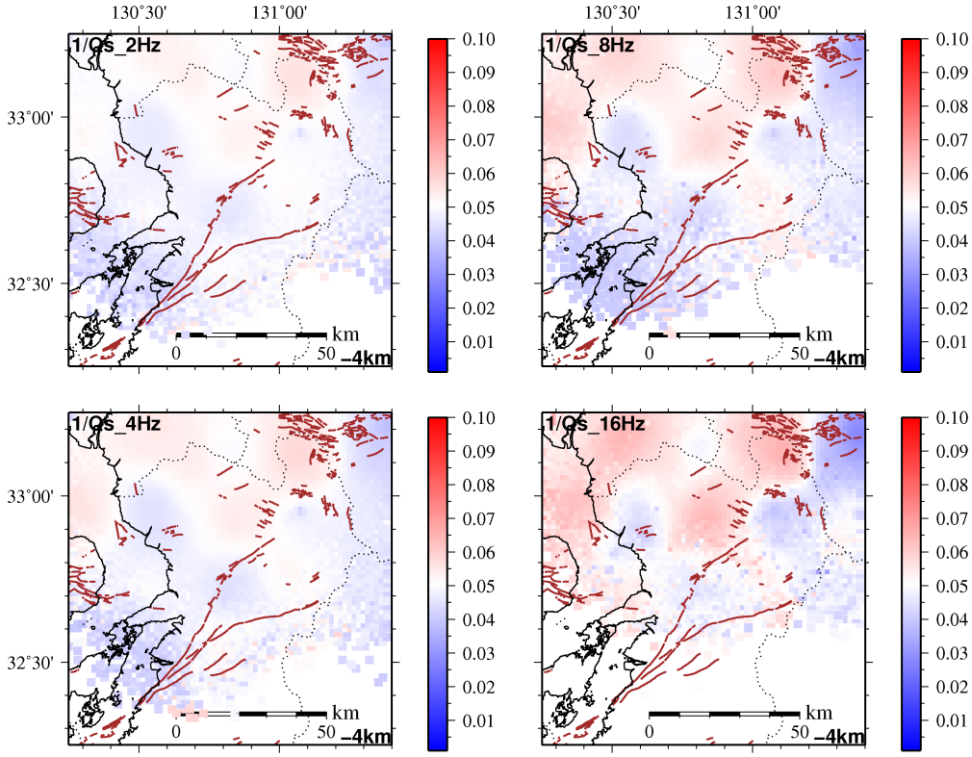

Figure 3.1.19 Same as Fig. 3.1.17 except depth = 4 km.

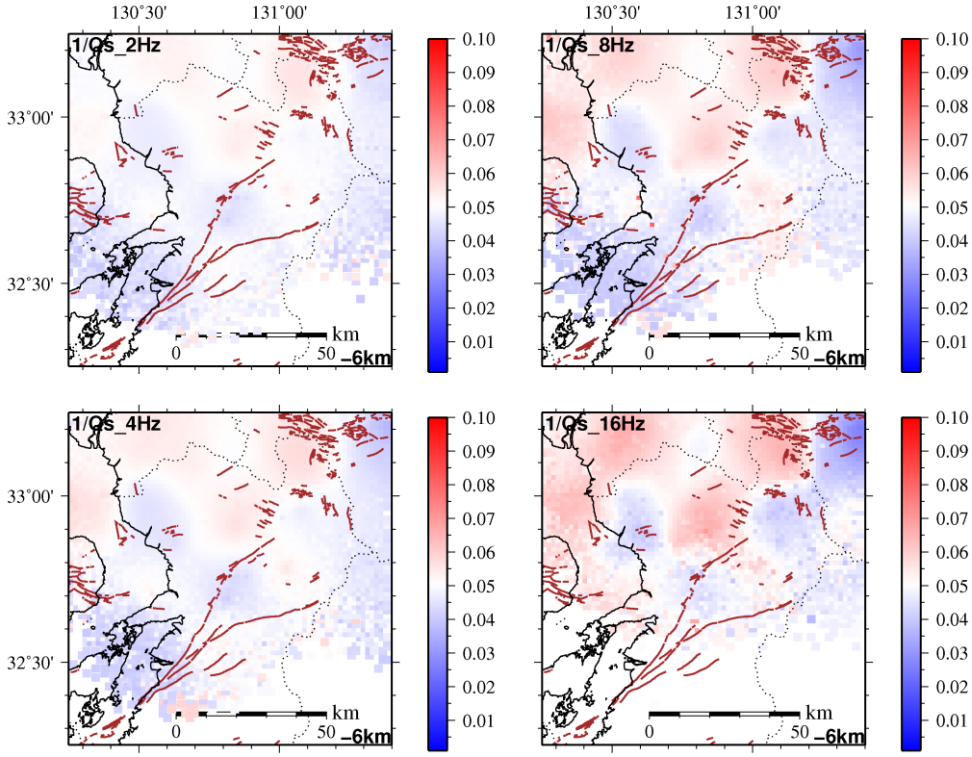

Figure 3.1.20 Same as Fig. 3.1.17 except depth = 6 km.

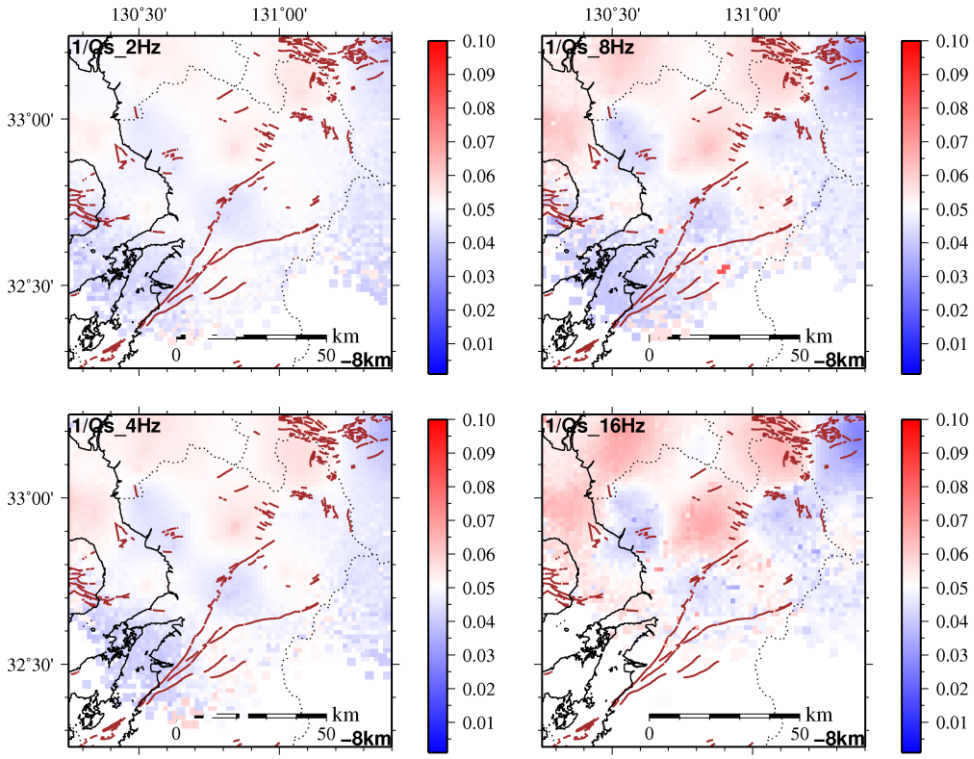

Figure 3.1.21 Same as Fig. 3.1.17 except depth = 8 km.

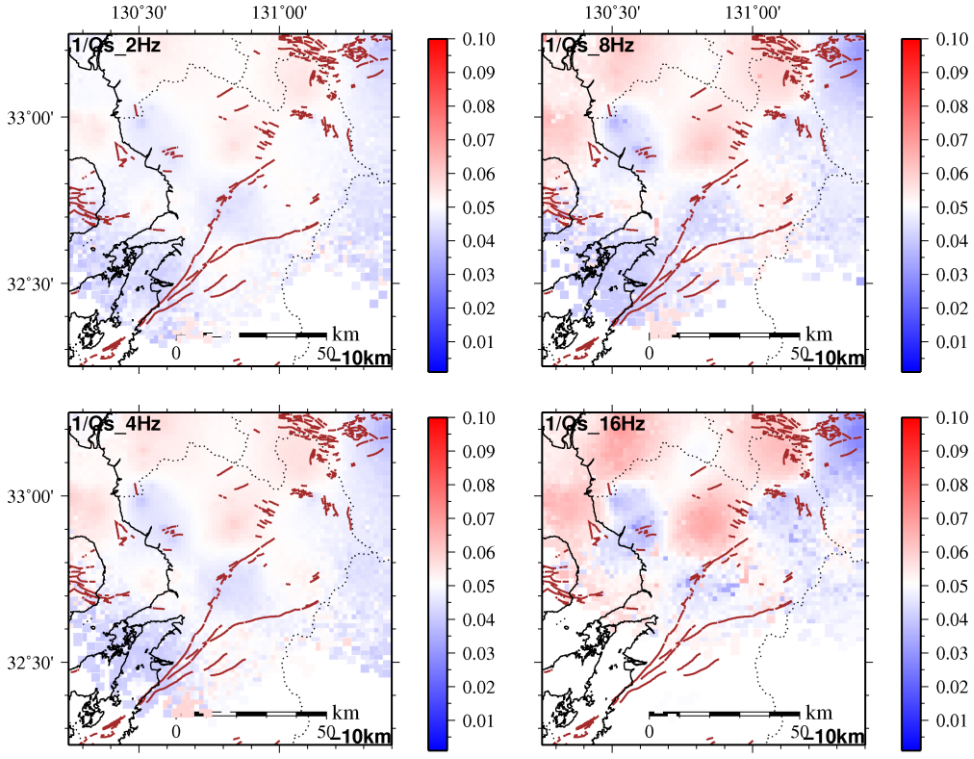

Figure 3.1.22 Same as Fig. 3.1.17 except depth = 10 km.

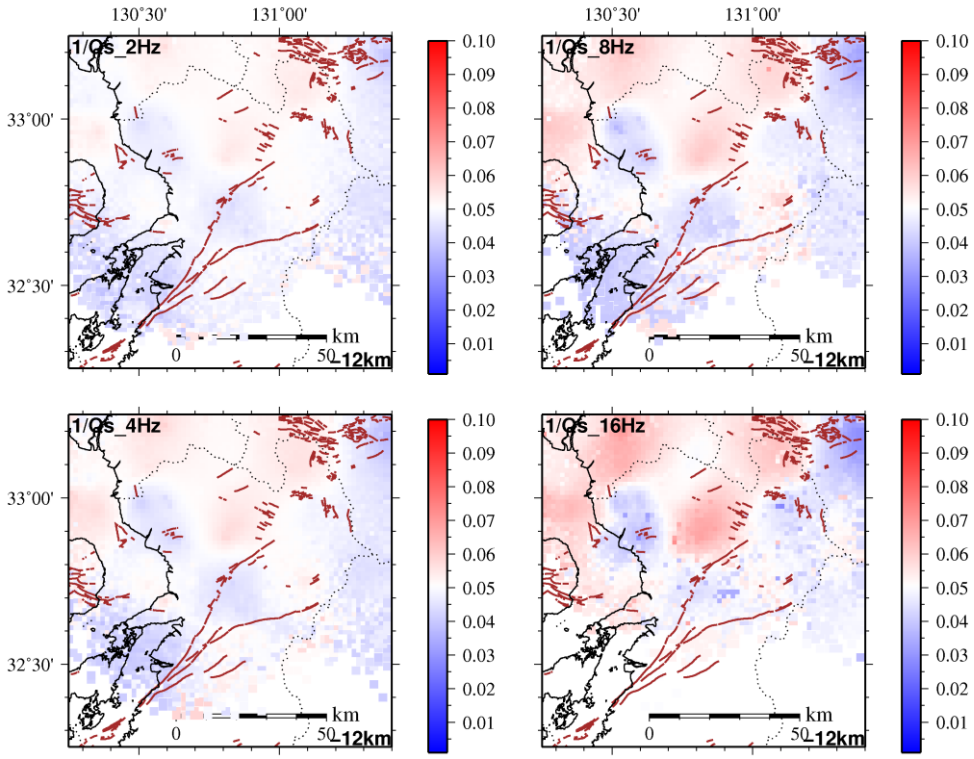

Figure 3.1.23 Same as Fig. 3.1.17 except depth = 12 km.

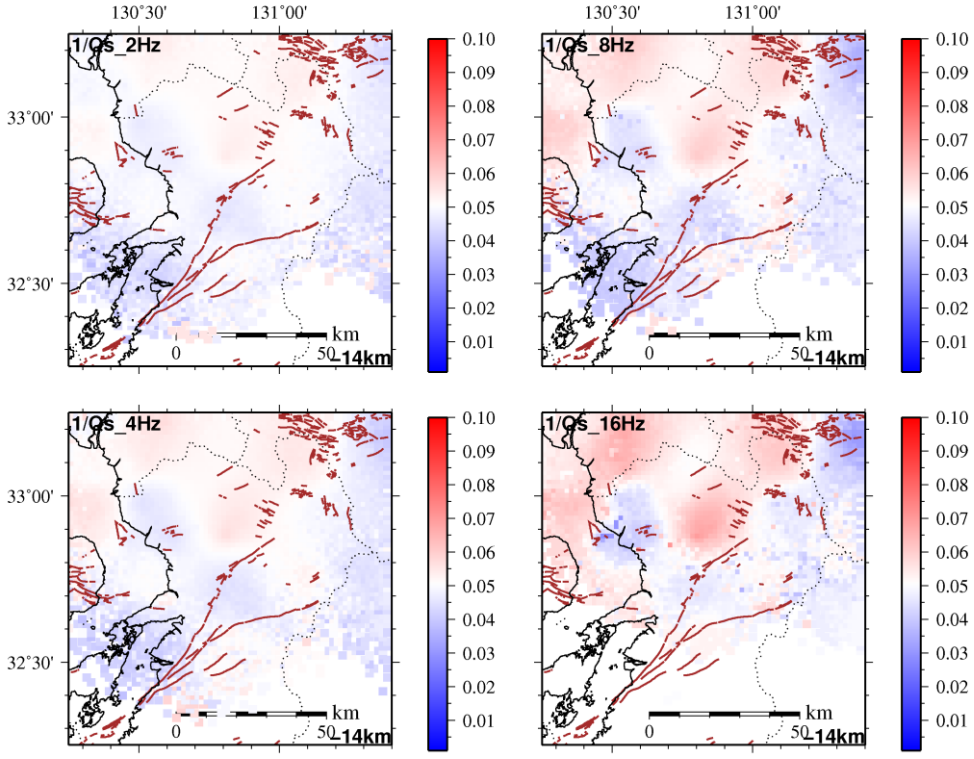

Figure 3.1.24 Same as Fig. 3.1.17 except depth = 14 km.

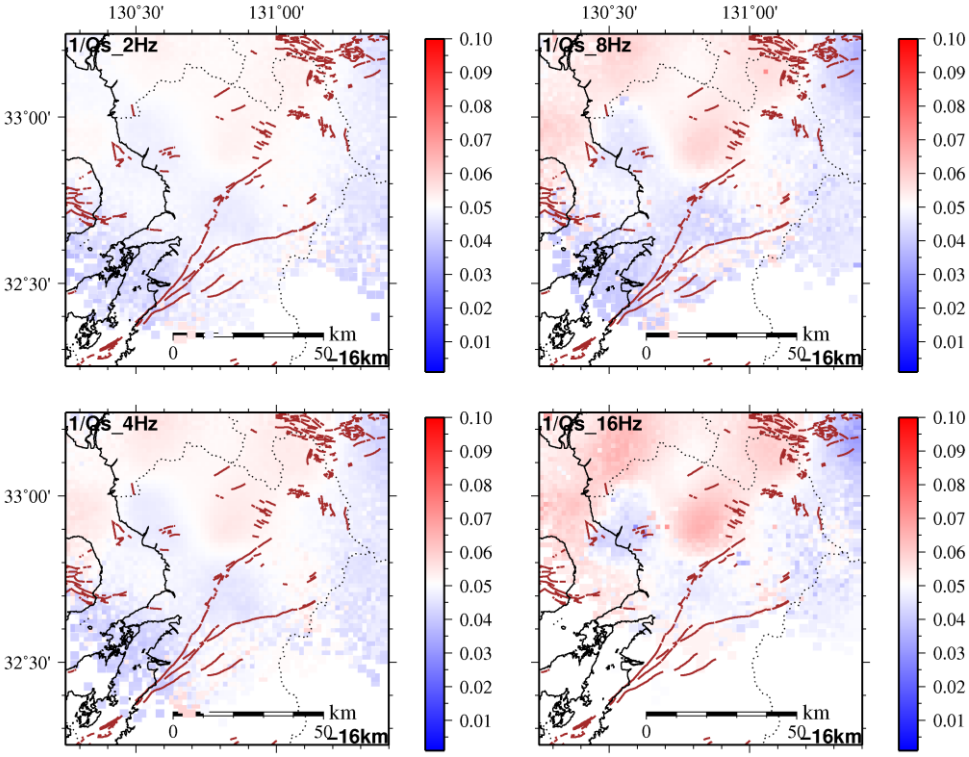

Figure 3.1.25 Same as Fig. 3.1.17 except depth = 16 km.

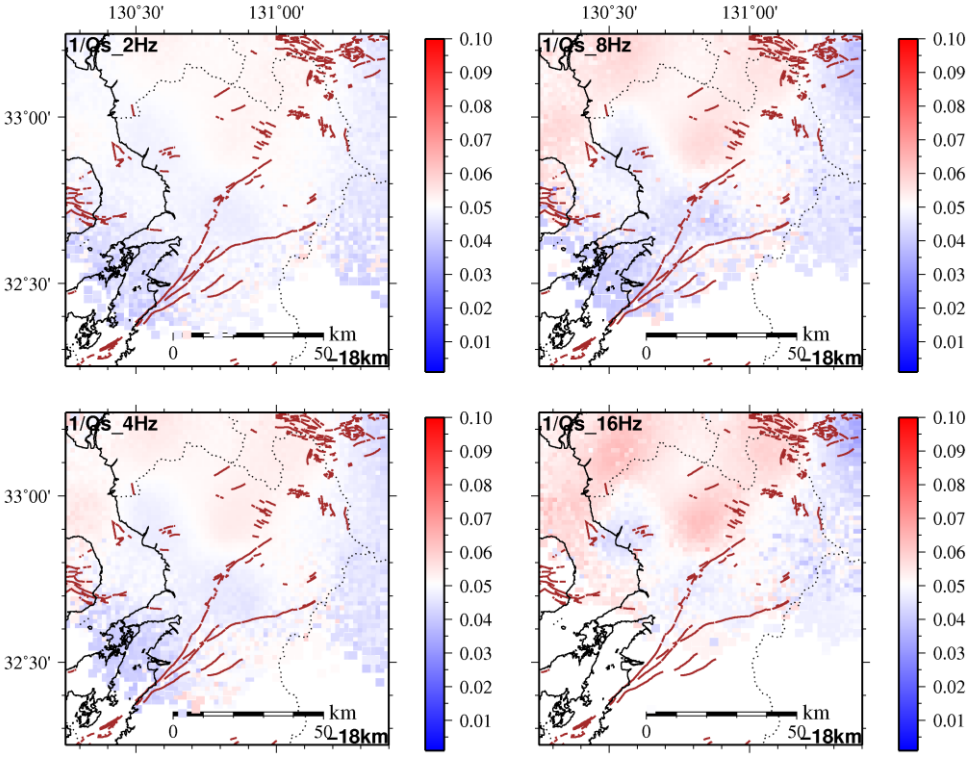

Figure 3.1.26 Same as Fig. 3.1.17 except depth = 18 km.

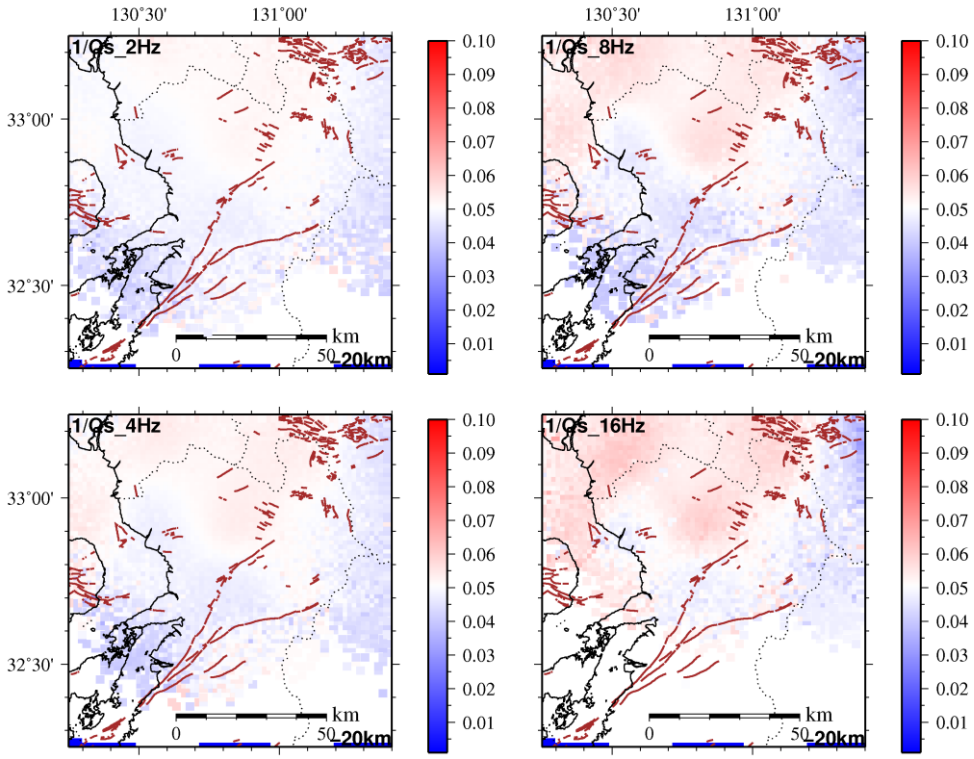

Figure 3.1.27 Same as Fig. 3.1.17 except depth = 20 km.

3.2 $Q_{i,s}^{-1}$ mapping

We obtain the spatial distribution for Q_i^{-1} and Q_s^{-1} values from the observed envelopes through the processing described in Chapter 2.

Q_i^{-1} structure

The results for Q_i^{-1} at depth ranges of every 2 km are shown in Figs.3.2.1 – 3.2.16, respectively. Spatial weighting factor distributions are plotted in the maps of Figs. 3.2.17 – 3.2.32

In general, the value of Q_i^{-1} spatially perturbs in a range of twice or three times as the average value for the entire target area. In the band of 2, 4 Hz, the value in areas of Kuju to Aso reveals strong attenuation. Especially, at 2 Hz, the attenuation factor around Kuju is the largest among the target area and it continues to the deep part.

At 4 Hz, a northeastern part with large attenuation corresponds to the Aso caldera, and the anomalous region with large attenuation shrink for deeper area than 10 km.

In the frequency bands at 8 and 16 Hz, the region of high attenuation is found in the northern part of the Futagawa fault zone.

The strong attenuation part seen in middle part of the result of 8 Hz shift southward with increment of the depth range.

A remarkable high attenuation zone around depth of 5 km at 16 Hz band corresponds to the northern edge of the high seismic activity zone after the 2016 Kumamoto earthquake.

Vertical cross-sections across the fault zone are shown in Figs. 3.2.33 – 3.2.36. The areas with strong intrinsic attenuation are found north of the fault zone.

Q_s^{-1} structure

The results for Q_s^{-1} and the spatial weighting factor are shown in Figs.3.2.37 – 3.2.52 and 3.2.53 – 3.2.68, respectively.

Spatial distribution in Q_s^{-1} value is relatively homogeneous compared with Q_s^{-1} structure. The Q_s^{-1} value in the east of the fault zone is slightly higher than in the west for all the frequency ranges. For higher frequency ranges than 4 Hz, relative high attenuation area is found in the surrounding area of Aso caldera (e.g. Kumamoto and Takachiho

areas). At 8 Hz, the attenuation value at the northern part of the Futagawa fault is larger than that of the surroundings, but the area shift toward south with inclement of the depth. Vertical cross-sections of Q_s^{-1} distribution across the fault zone are shown in Figs. 3.2.69 – 3.2.72. The areas with strong intrinsic attenuation are found north of the fault zone. Two strong scattering attenuation areas are found at the aftershock area and about 20 km north of the aftershock area. Seismic activities in the both areas are relatively high among the target area. The events analyzed in this study are selected to be homogeneous distribution for avoiding resolution bias. Therefore, the feature that corresponding of high scattering to seismic activity might be reliable.
The spatial variation is not stronger than the intrinsic attenuation. This can be attributed to the processing in this study. As described in chapter 2, the envelope is normalized by average amplitude during analyzing time window. This process weakens the contribution of the Q_s^{-1} to the formula 2.1. Based on formula 2.1, the Q_s^{-1} contribution dominates at the latter half part of the analyzing window. In order to resolve fine structure of Q_s^{-1}, time window of the analysis requires to start just after direct S wave. However, effect of radiation pattern of the earthquake must strongly affect to the estimation. Therefore, we adopt our time window setting.

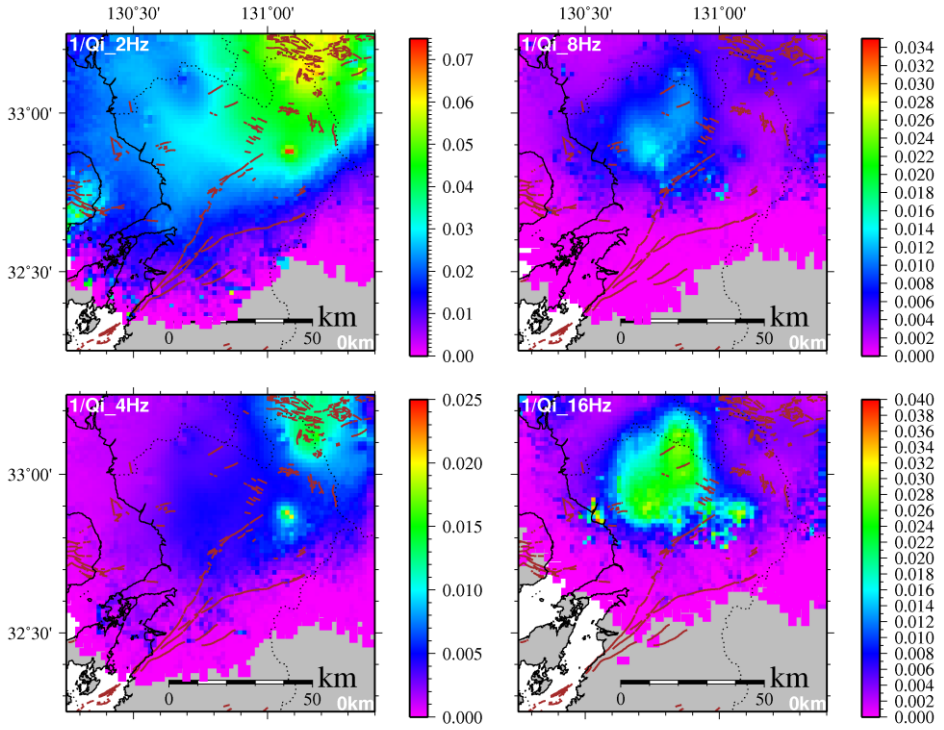

Figure 3.2.1 Map showing estimated Q_i^{-1} distribution at depth of 0 km. The result at four frequency ranges are displayed. Color in the map indicates Q_i^{-1} value as shown in the scale bar at the left of the map.

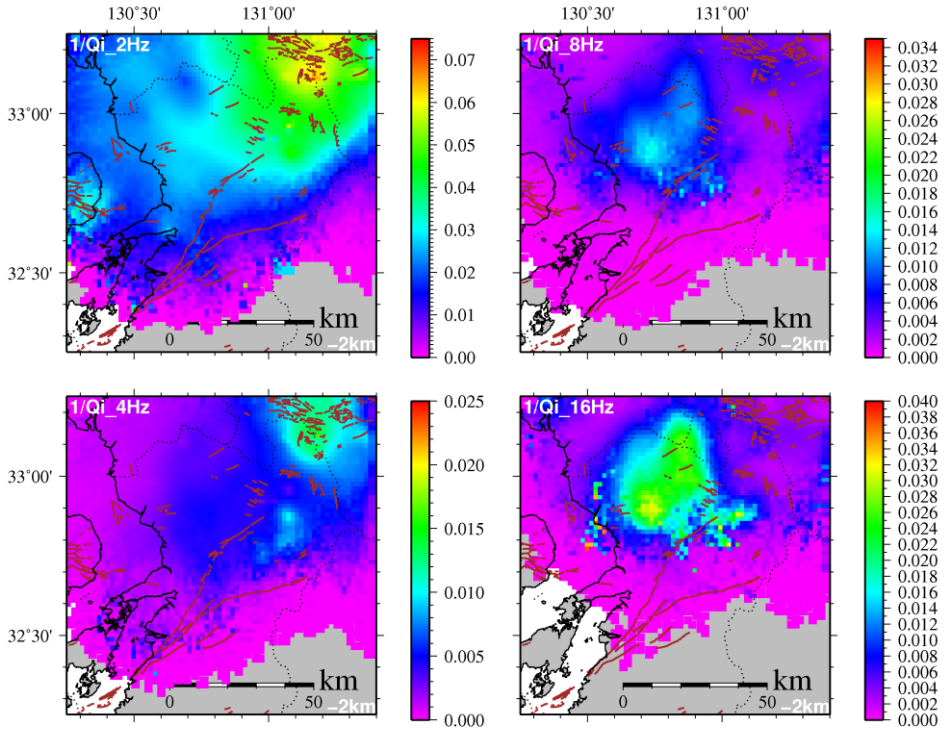

Figure 3.2.2 Same as Fig. 3.2.1 except depth = 2 km.

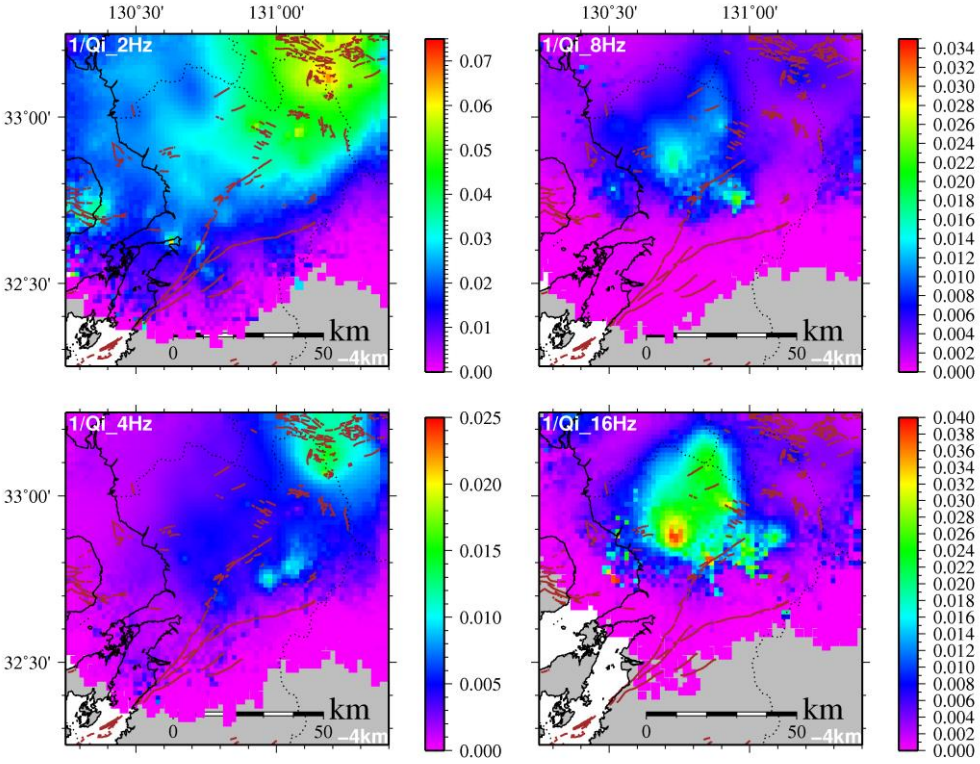

Figure 3.2.3 Same as Fig. 3.2.1 except depth = 4 km.

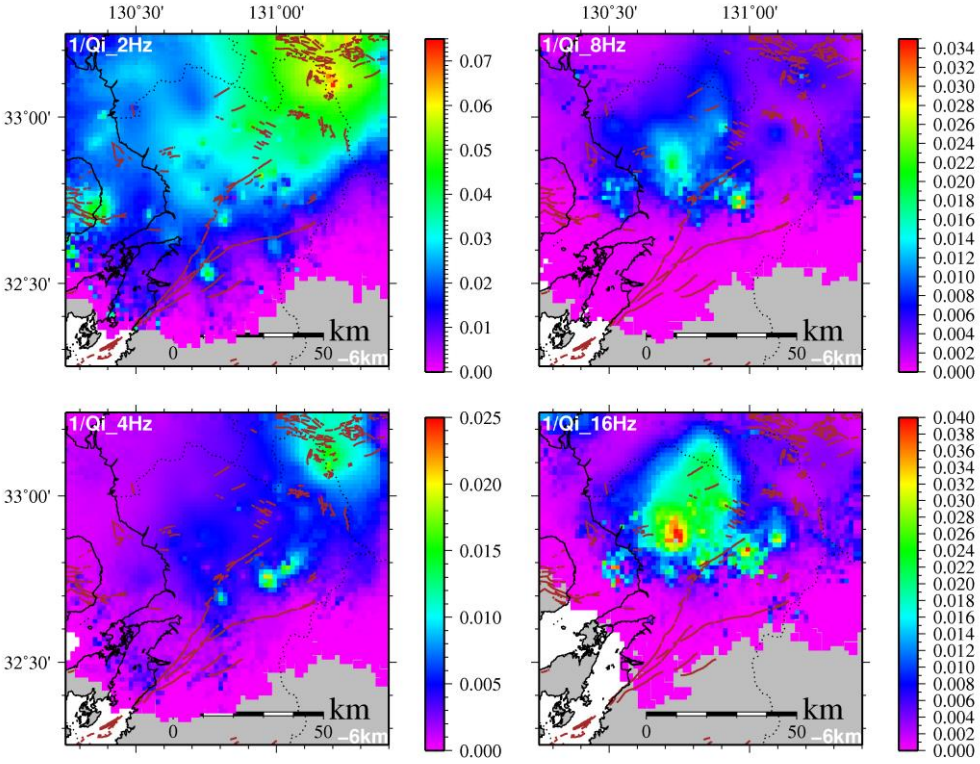

Figure 3.2.4 Same as Fig. 3.2.1 except depth = 6 km.

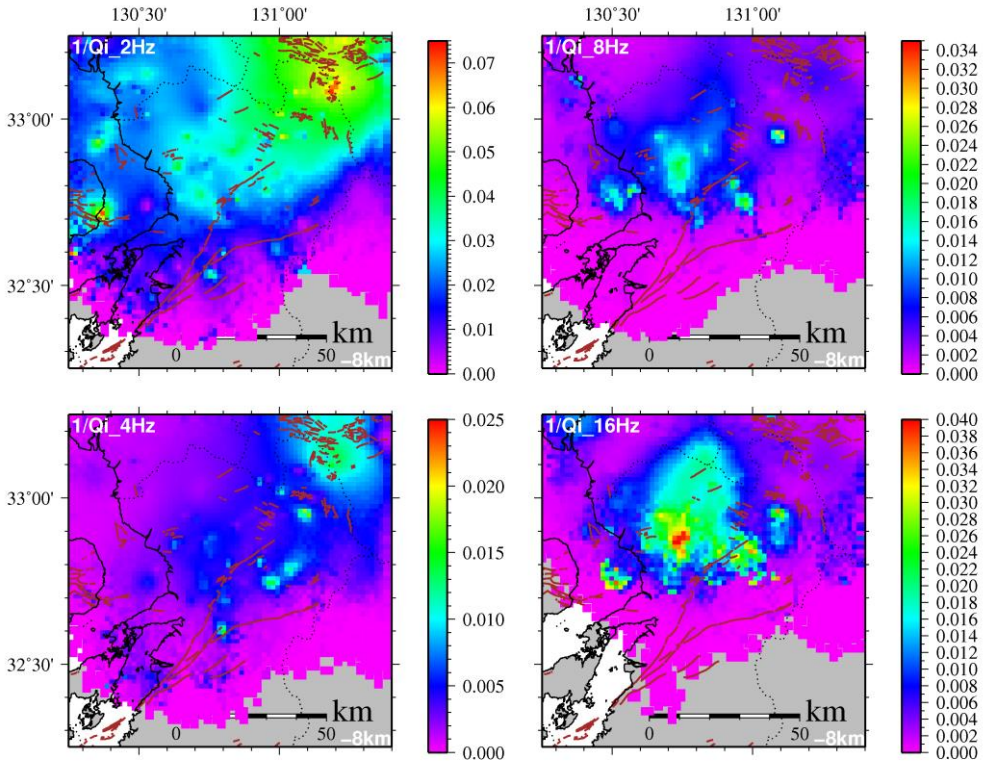

Figure 3.2.5 Same as Fig. 3.2.1 except depth = 8 km.

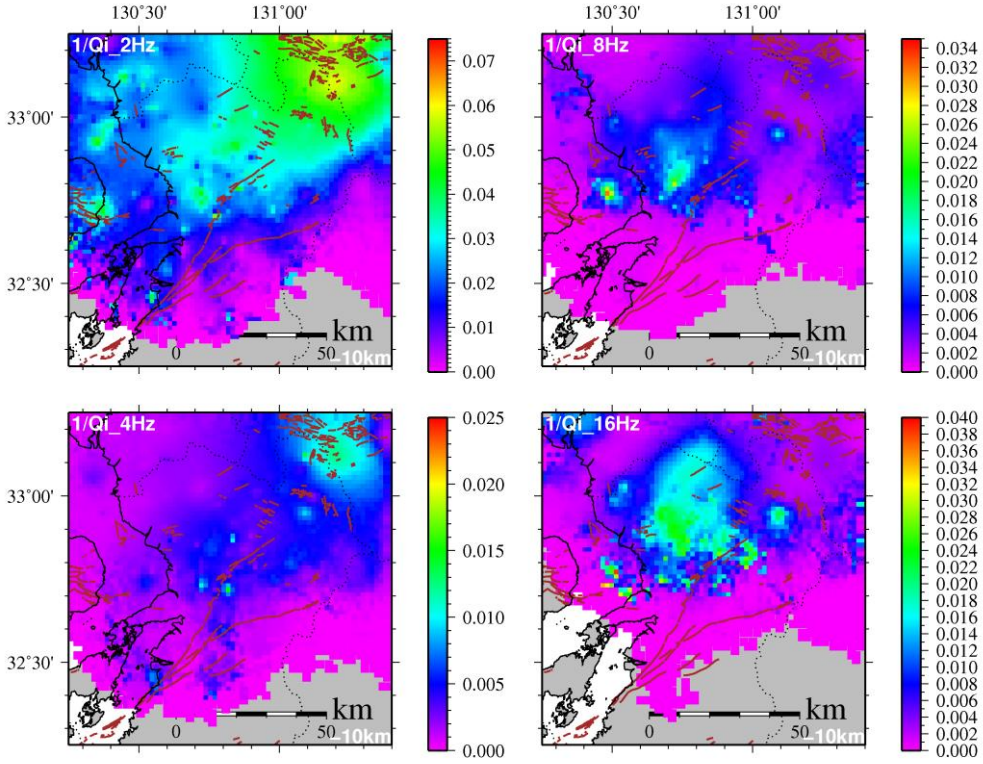

Figure 3.2.6 Same as Fig. 3.2.1 except depth = 10 km.

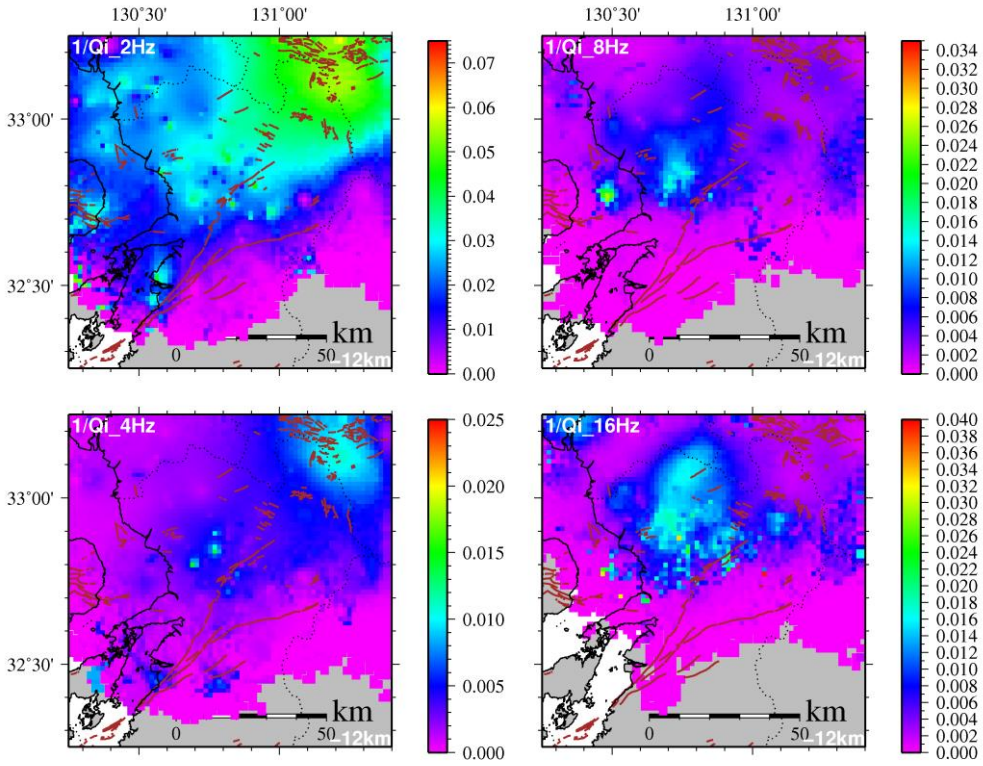

Figure 3.2.7 Same as Fig. 3.2.1 except depth = 12 km.

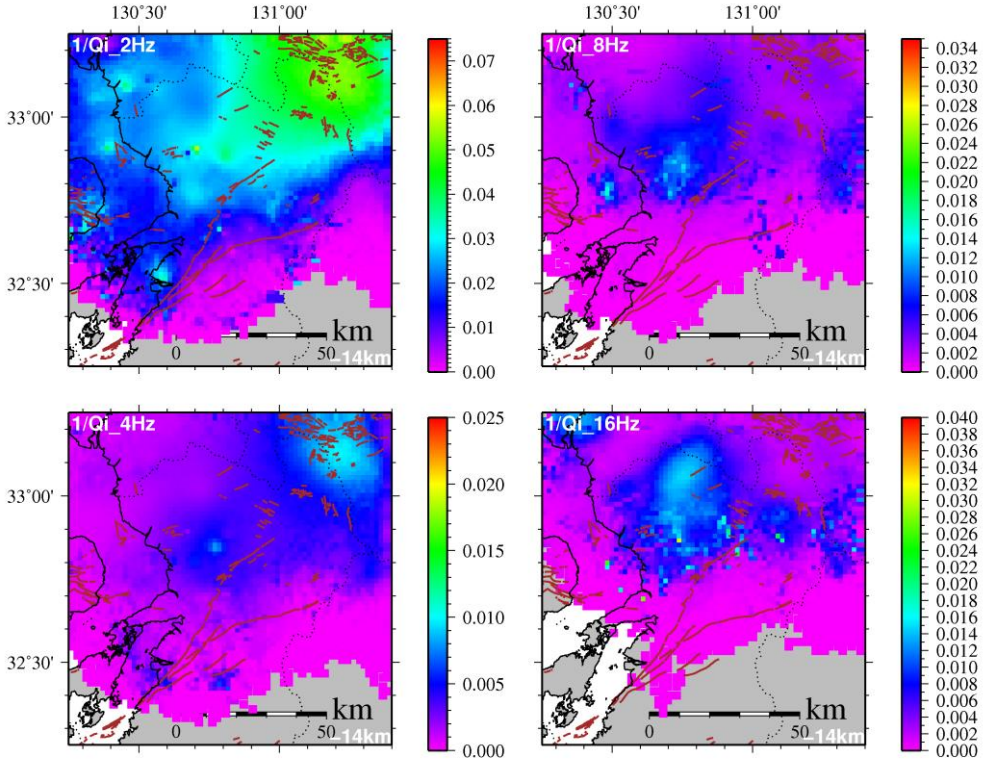

Figure 3.2.8 Same as Fig. 3.2.1 except depth = 14 km.

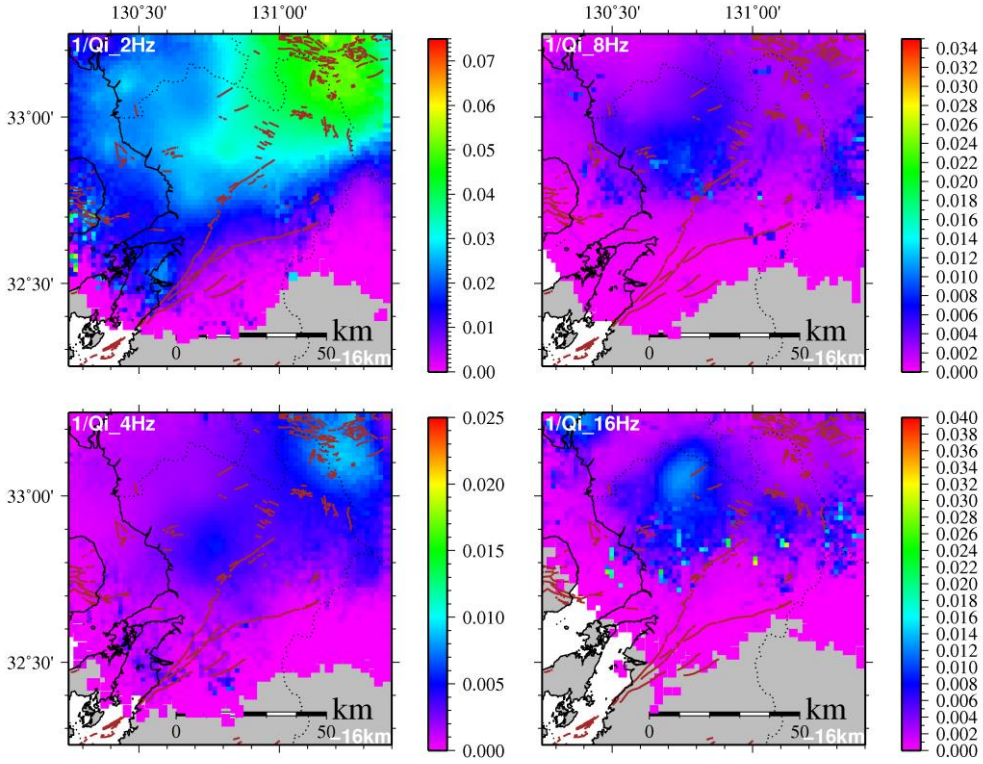

Figure 3.2.9 Same as Fig. 3.2.1 except depth = 16 km.

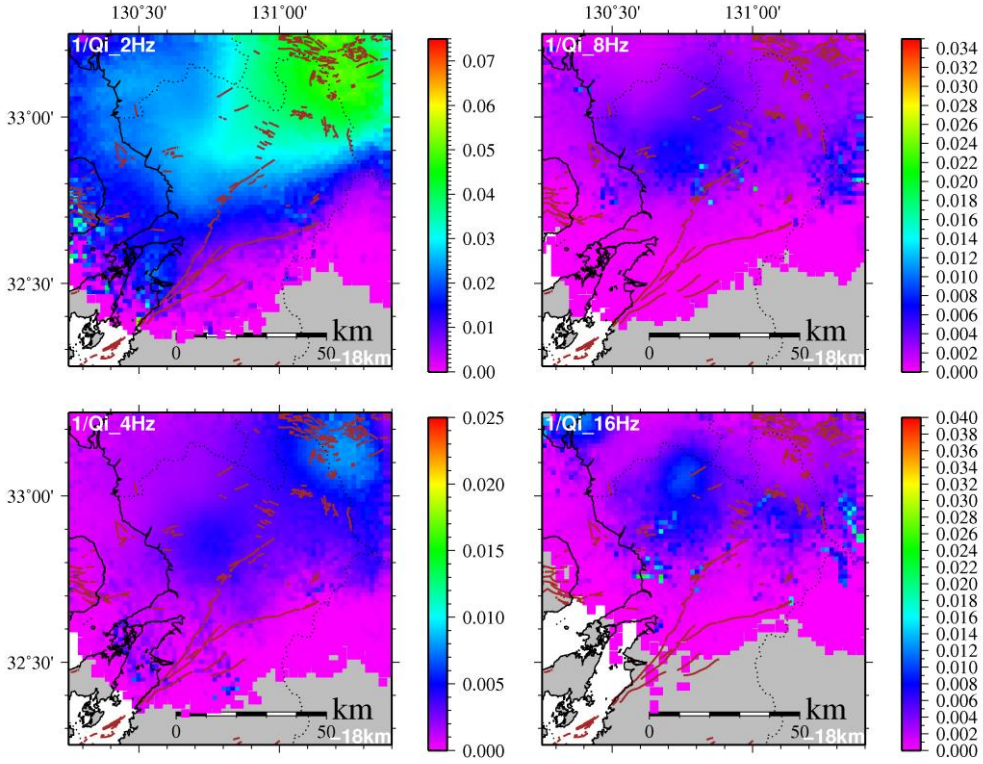

Figure 3.2.10 Same as Fig. 3.2.1 except depth = 18 km.

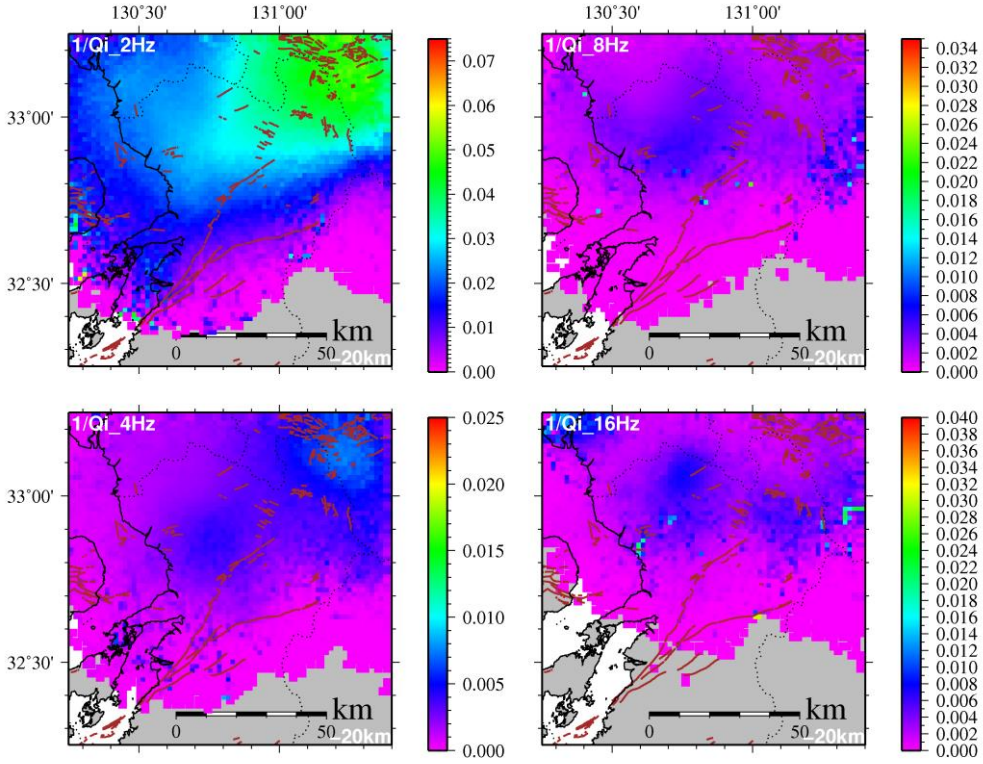

Figure 3.2.11 Same as Fig. 3.2.1 except depth = 20 km.

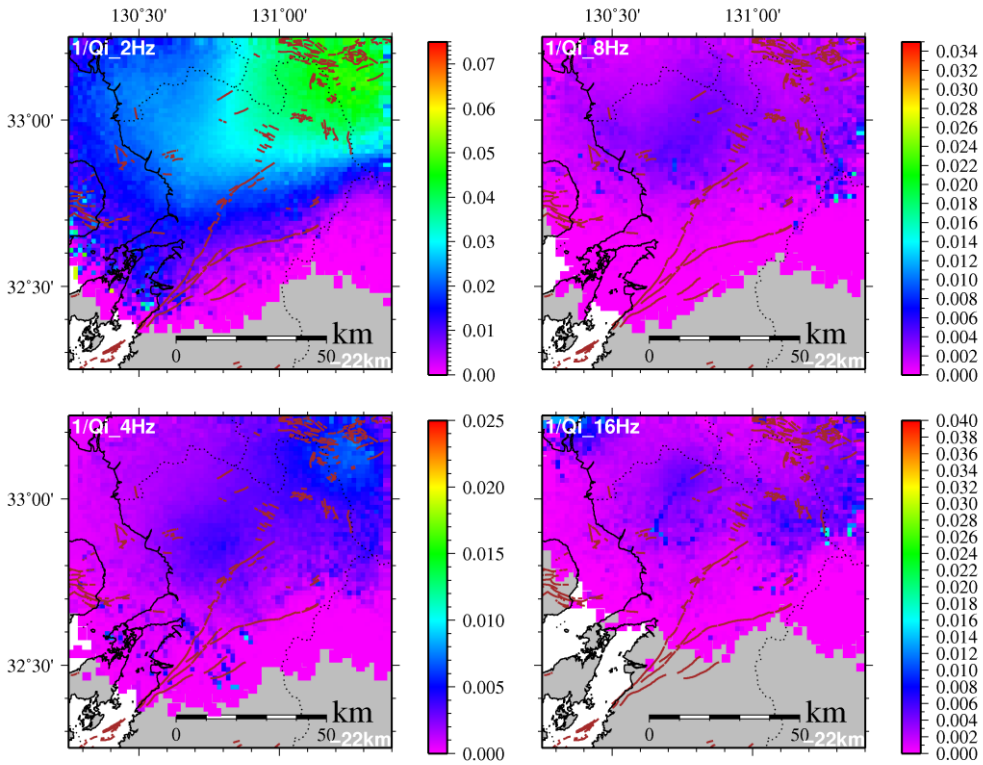

Figure 3.2.12 Same as Fig. 3.2.1 except depth = 22 km.

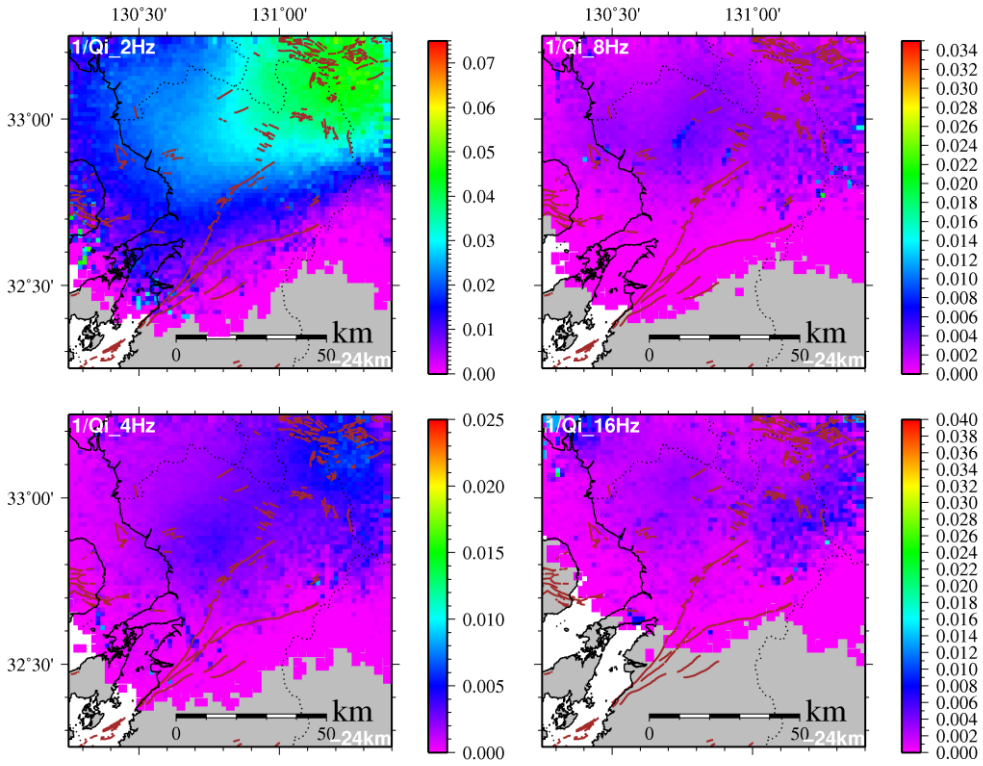

Figure 3.2.13 Same as Fig. 3.2.1 except depth = 24 km.

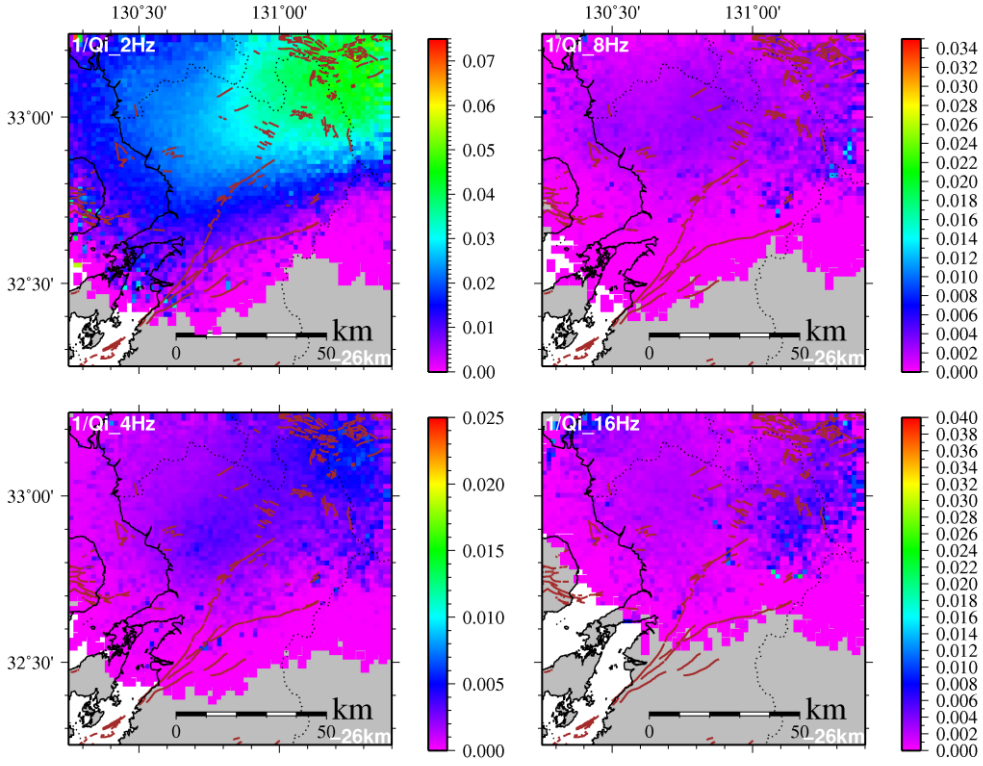

Figure 3.2.14 Same as Fig. 3.2.1 except depth = 26 km.

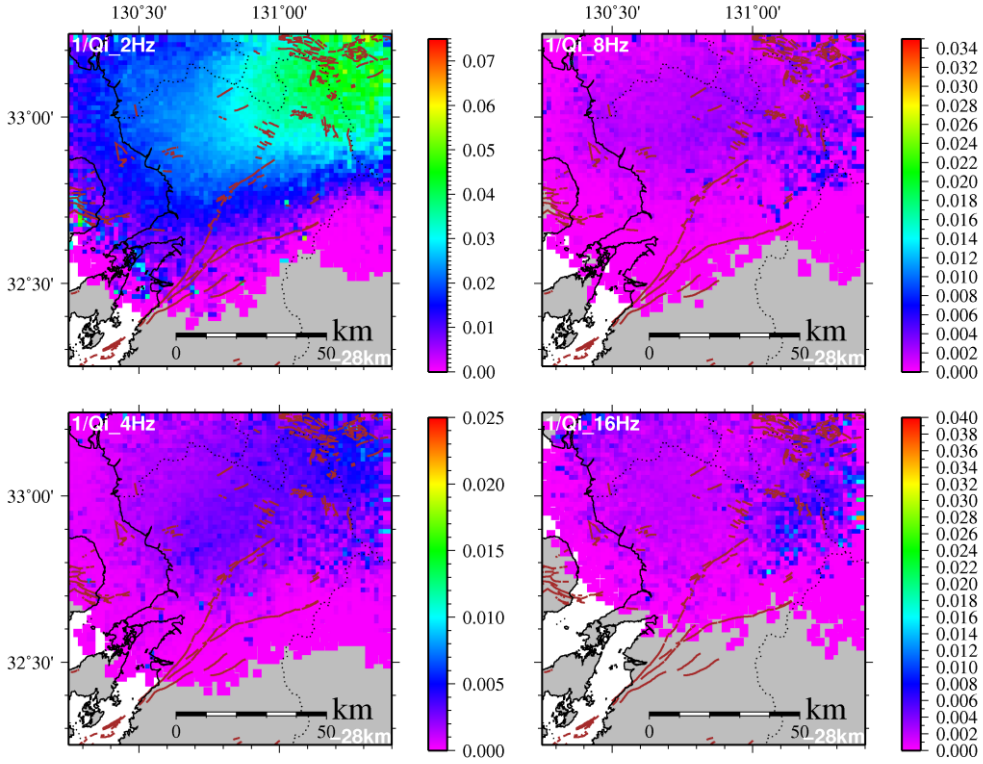

Figure 3.2.15 Same as Fig. 3.2.1 except depth = 28 km.

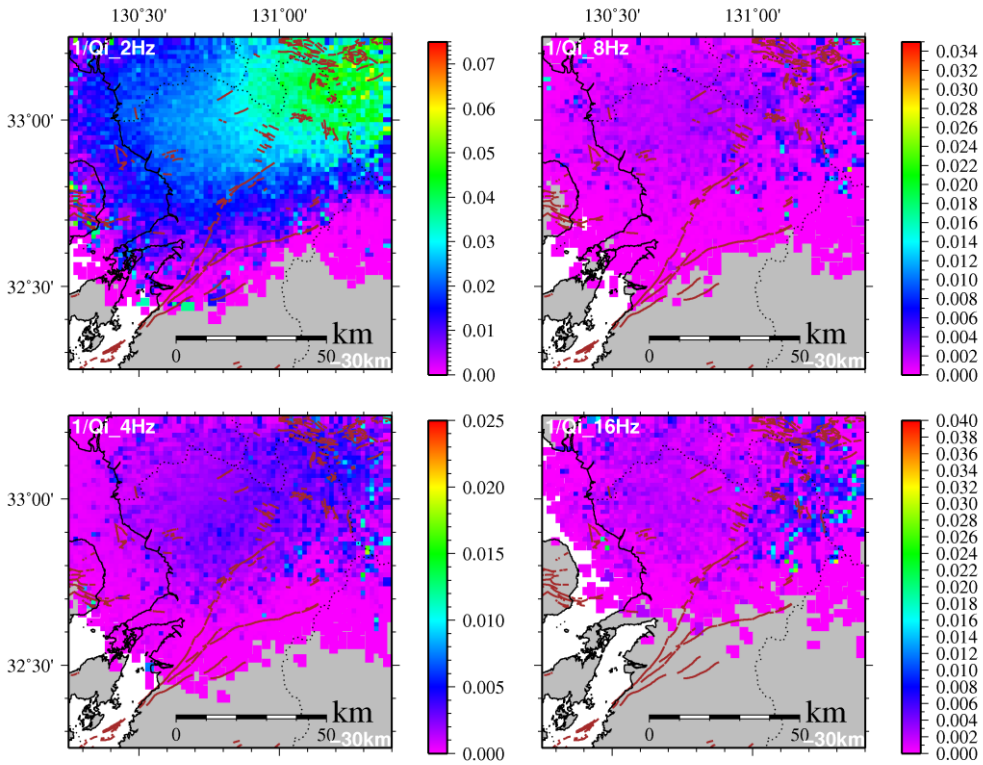

Figure 3.2.16 Same as Fig. 3.2.1 except depth = 30 km.

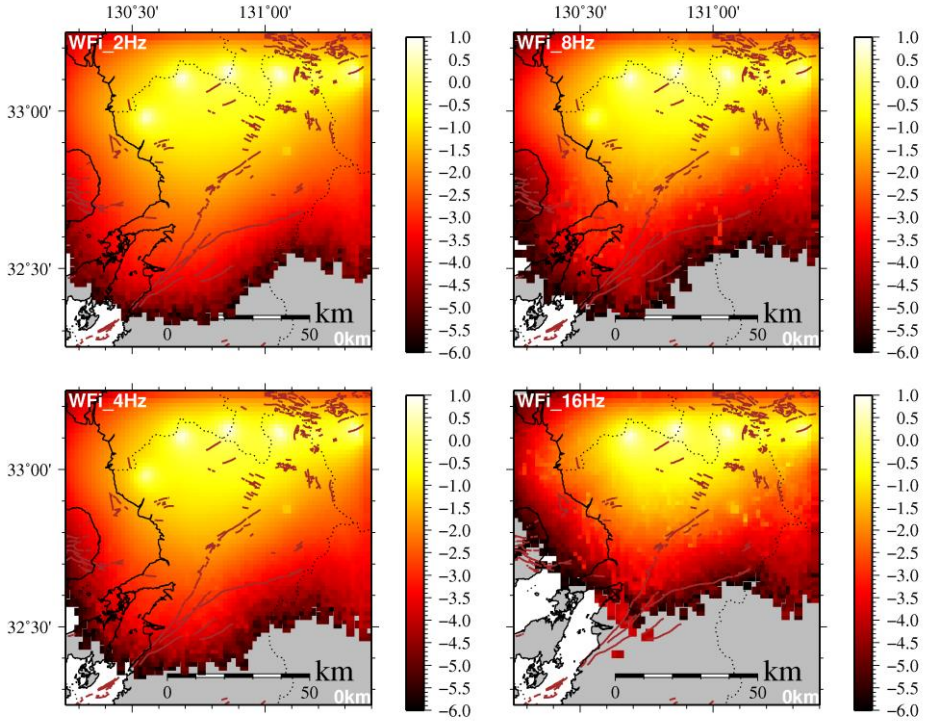

Figure 3.2.17 Map showing the weight distribution of Q_i^{-1} at depth 0 km. The result at four frequency ranges are displayed. Colors in the map indicates Q_i^{-1} value as shown in the scale bar at the left of the map.

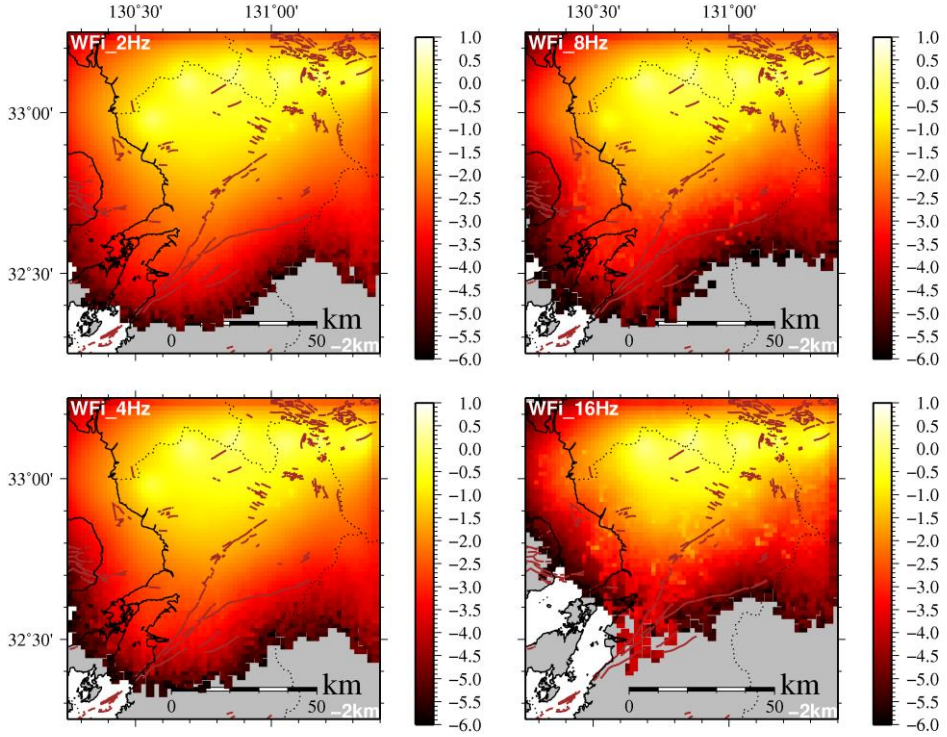

Figure 3.2.18 Same as Fig. 3.2.17 except depth = 2 km.

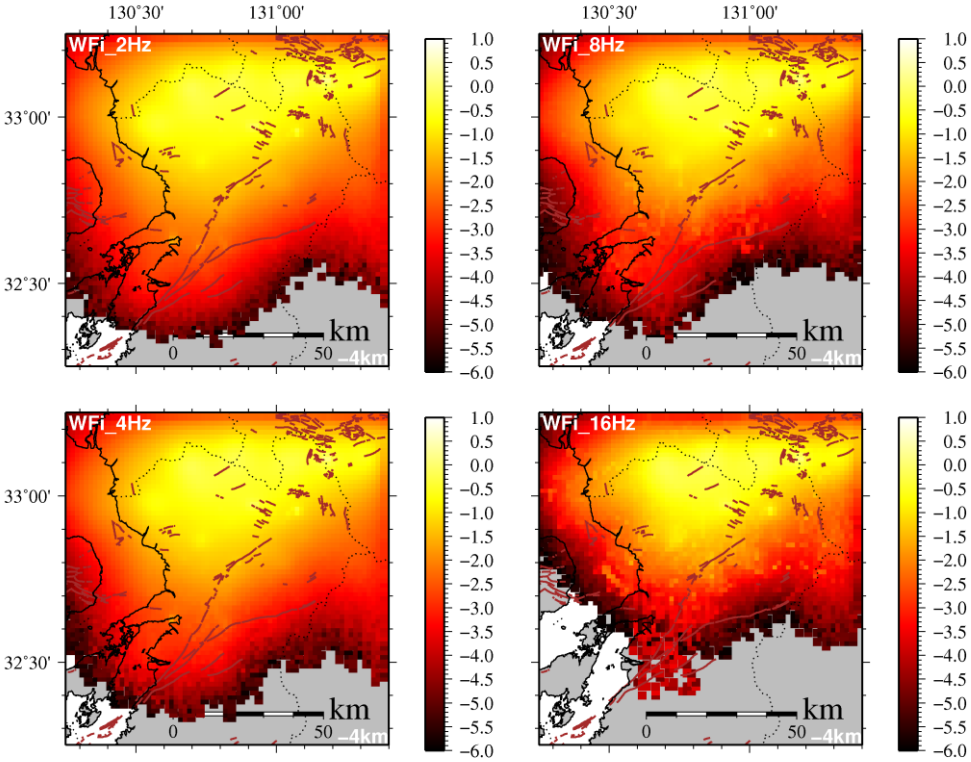

Figure 3.2.19 Same as Fig. 3.2.17 except depth = 4 km.

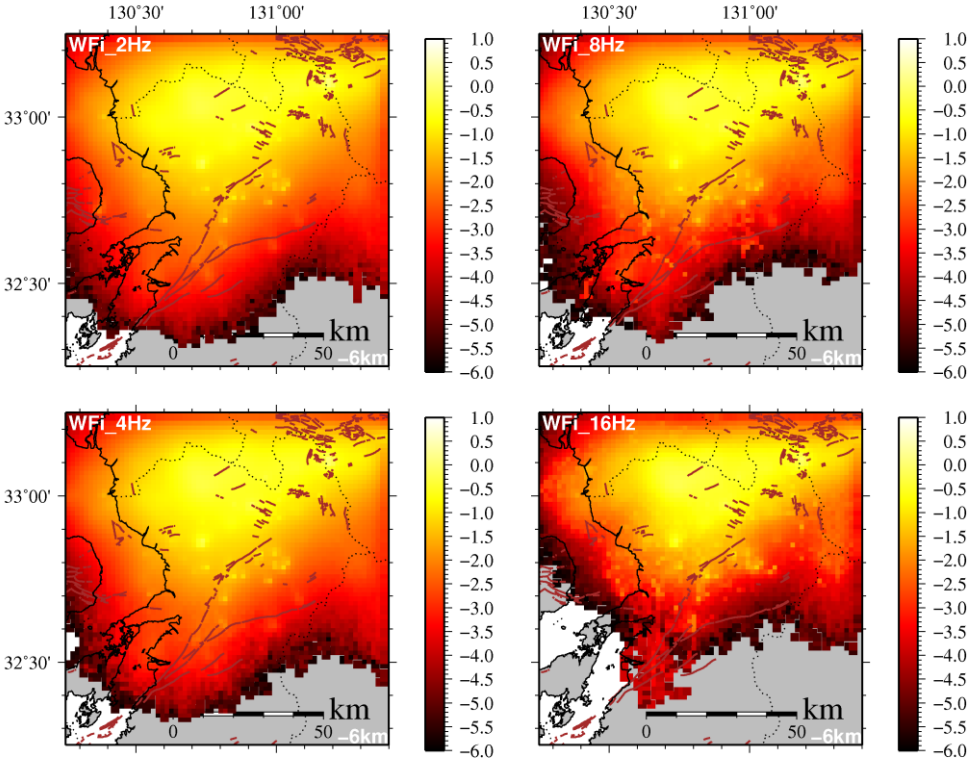

Figure 3.2.20 Same as Fig. 3.2.17 except depth = 6 km.

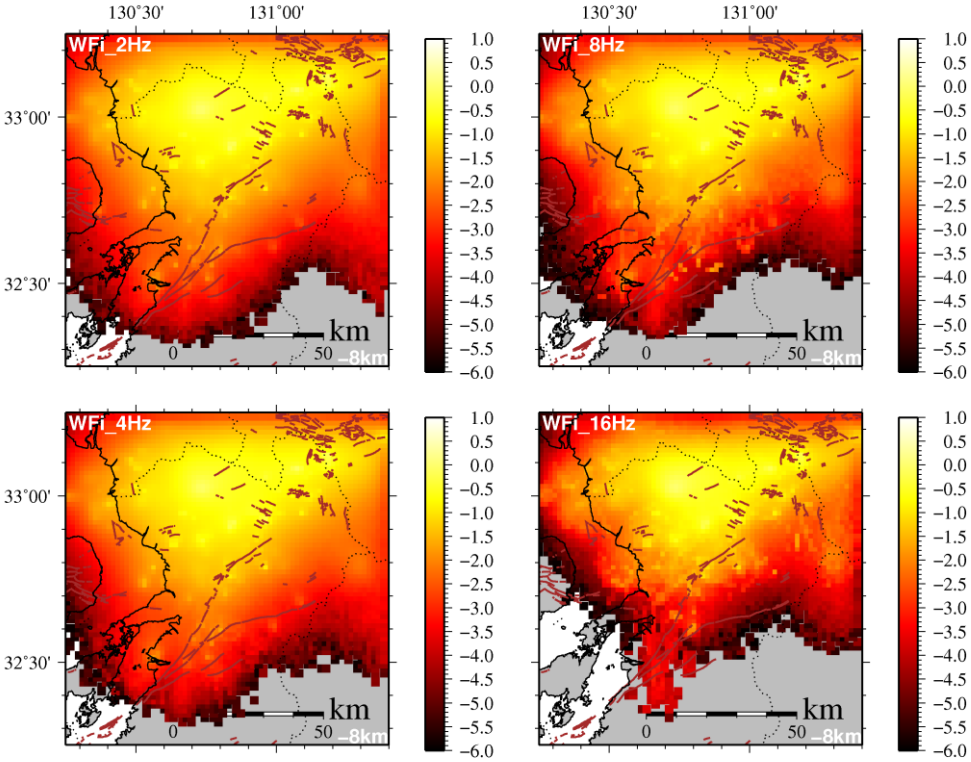

Figure 3.2.21 Same as Fig. 3.2.17 except depth = 8 km.

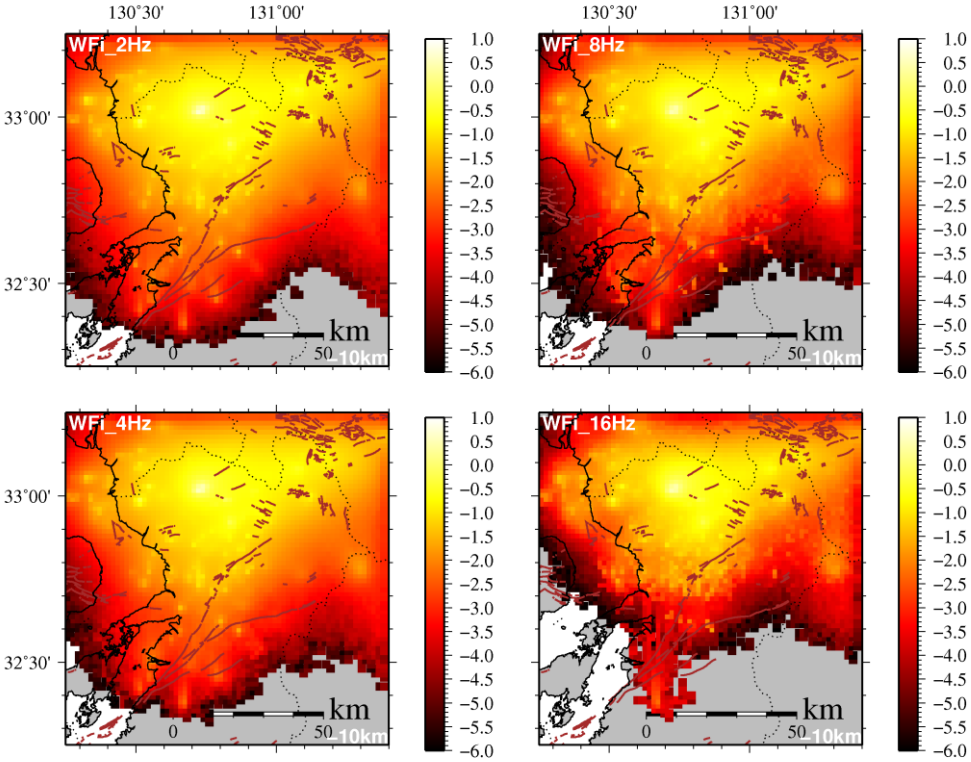

Figure 3.2.22 Same as Fig. 3.2.17 except depth = 10 km.

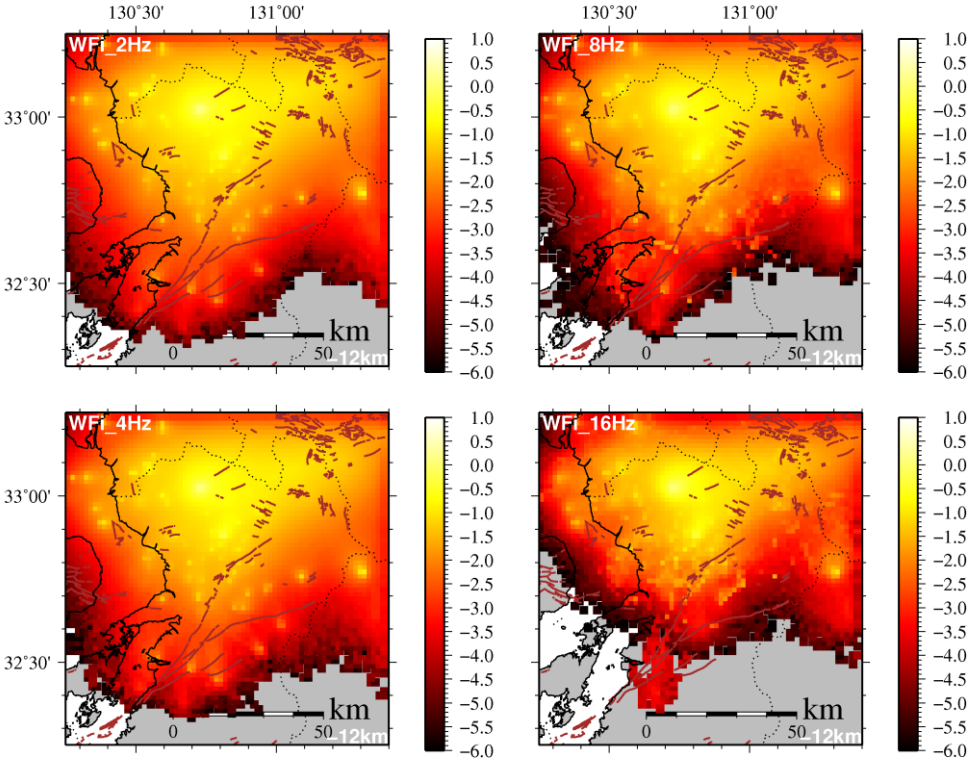

Figure 3.2.23 Same as Fig. 3.2.17 except depth = 12 km.

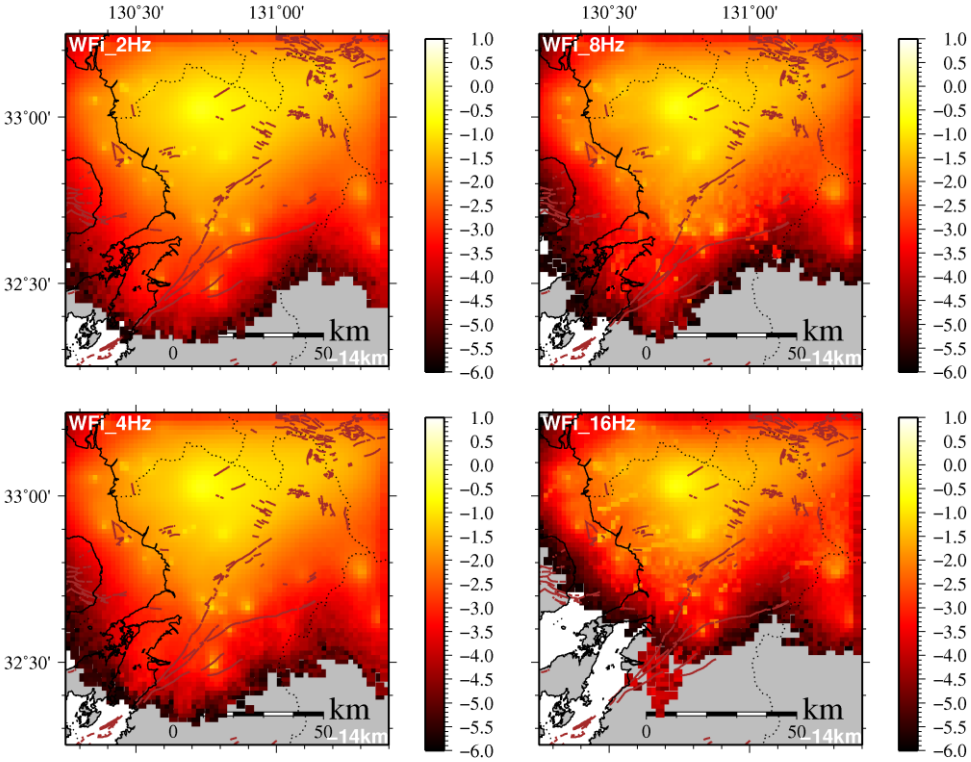

Figure 3.2.24 Same as Fig. 3.2.17 except depth = 14 km.

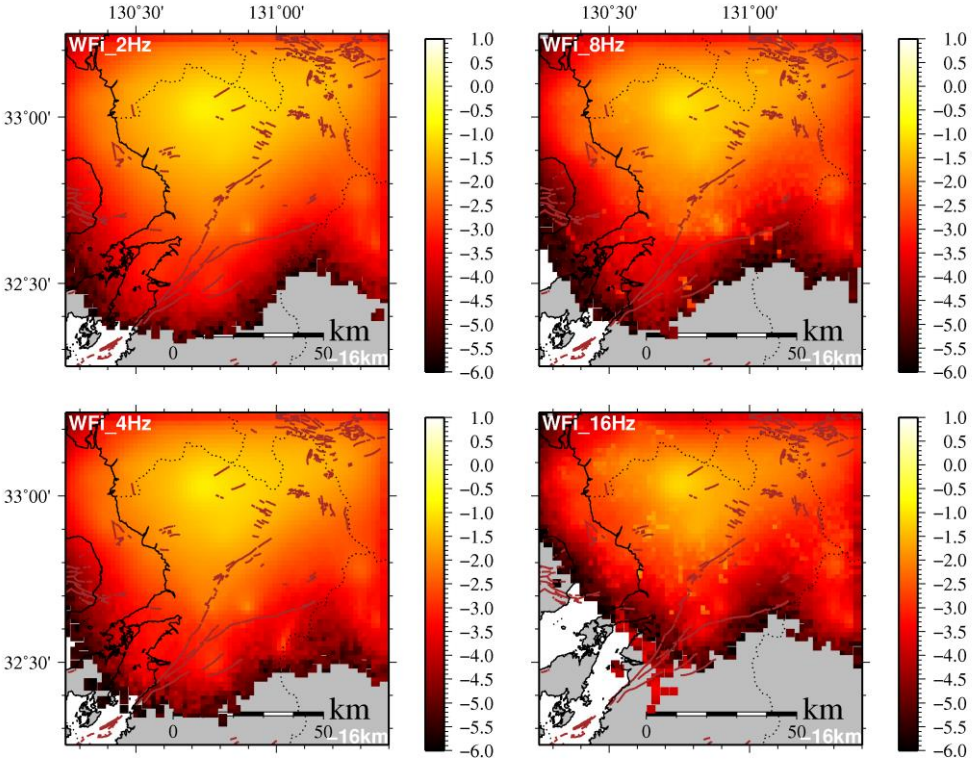

Figure 3.2.25 Same as Fig. 3.2.17 except depth = 16 km.

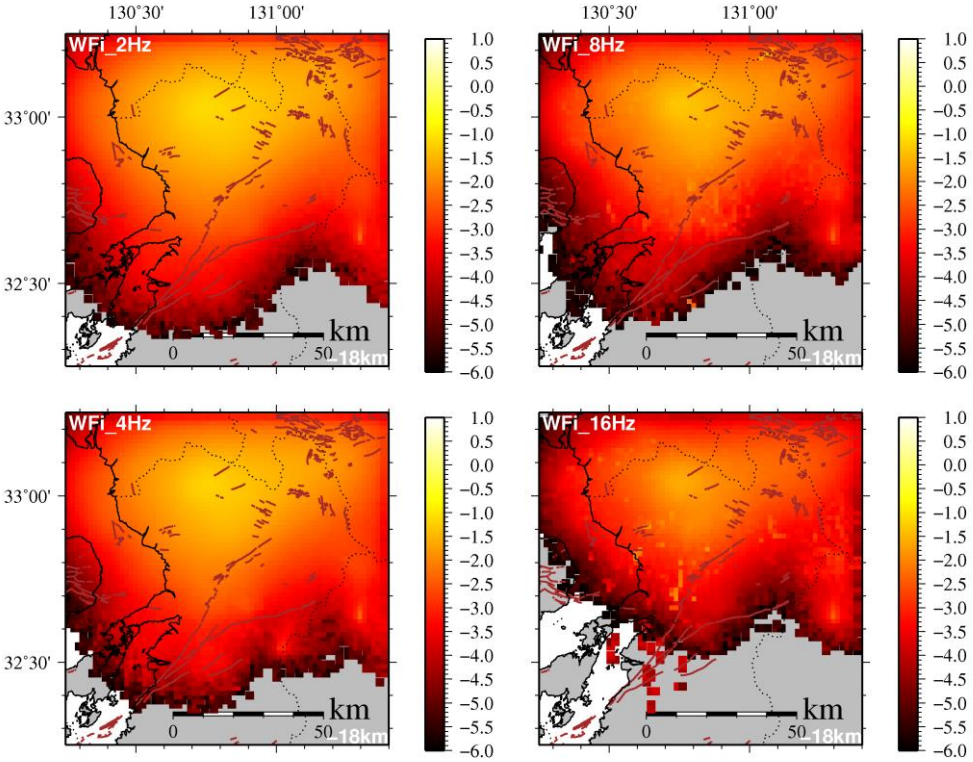

Figure 3.2.26 Same as Fig. 3.2.17 except depth = 18 km.

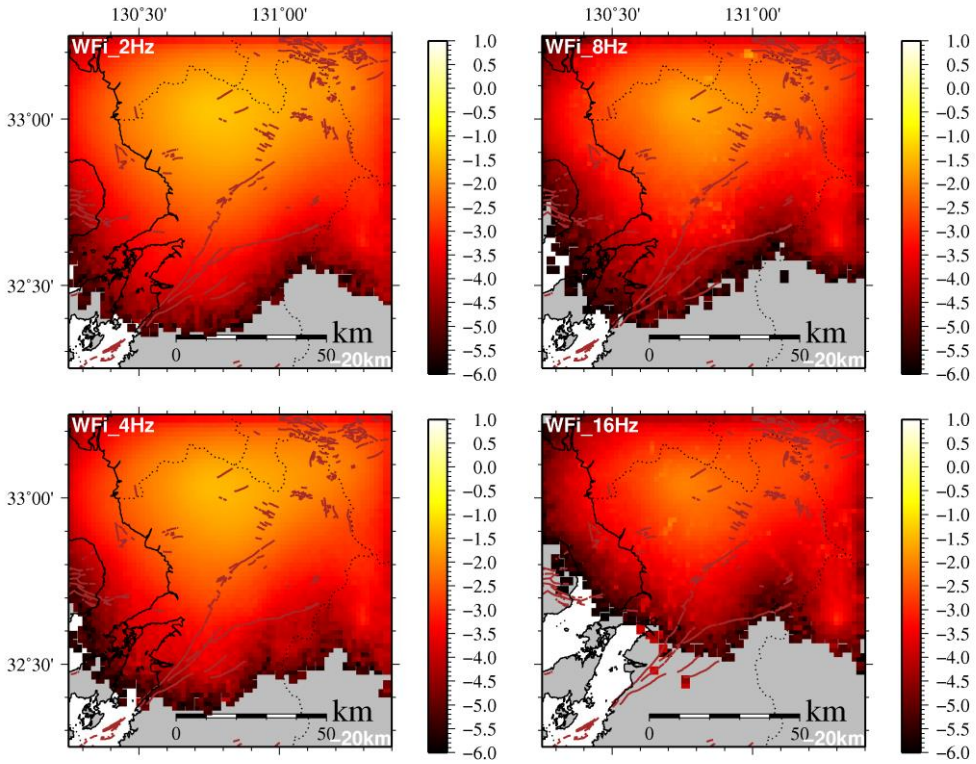

Figure 3.2.27 Same as Fig. 3.2.17 except depth = 20 km.

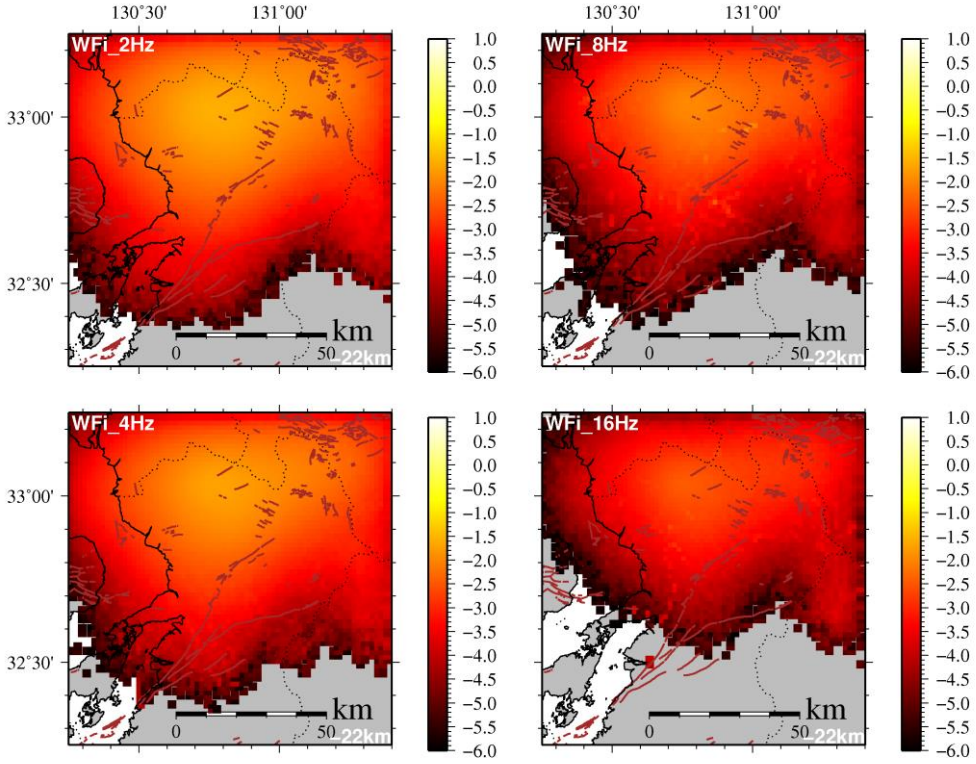

Figure 3.2.28 Same as Fig. 3.2.17 except depth = 22 km.

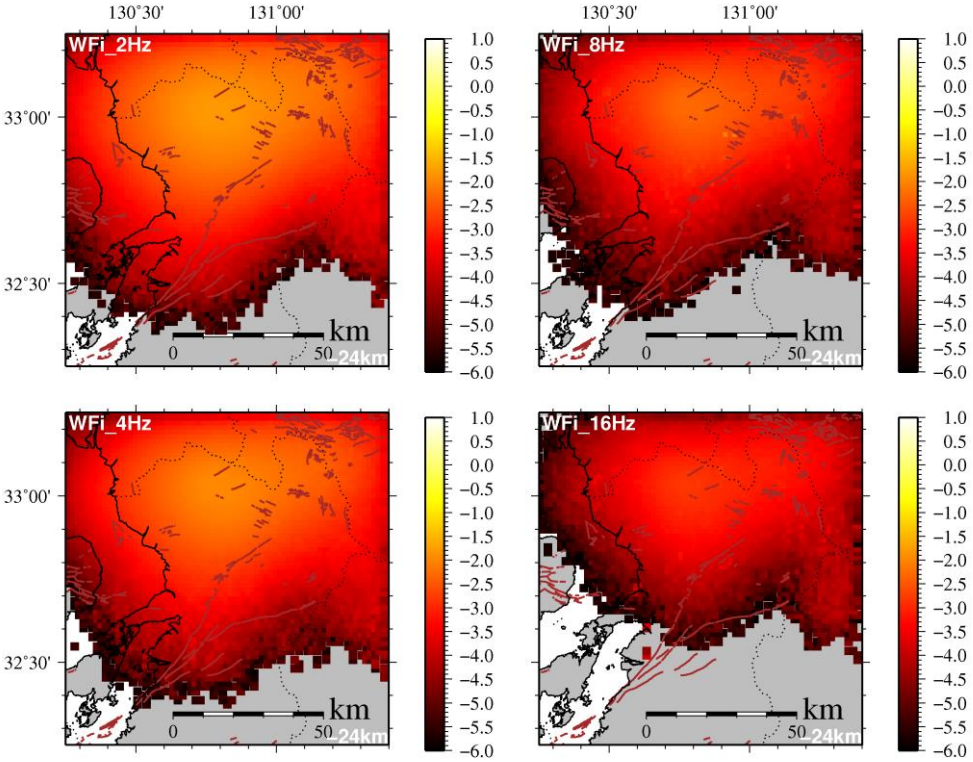

Figure 3.2.29 Same as Fig. 3.2.17 except depth = 24 km.

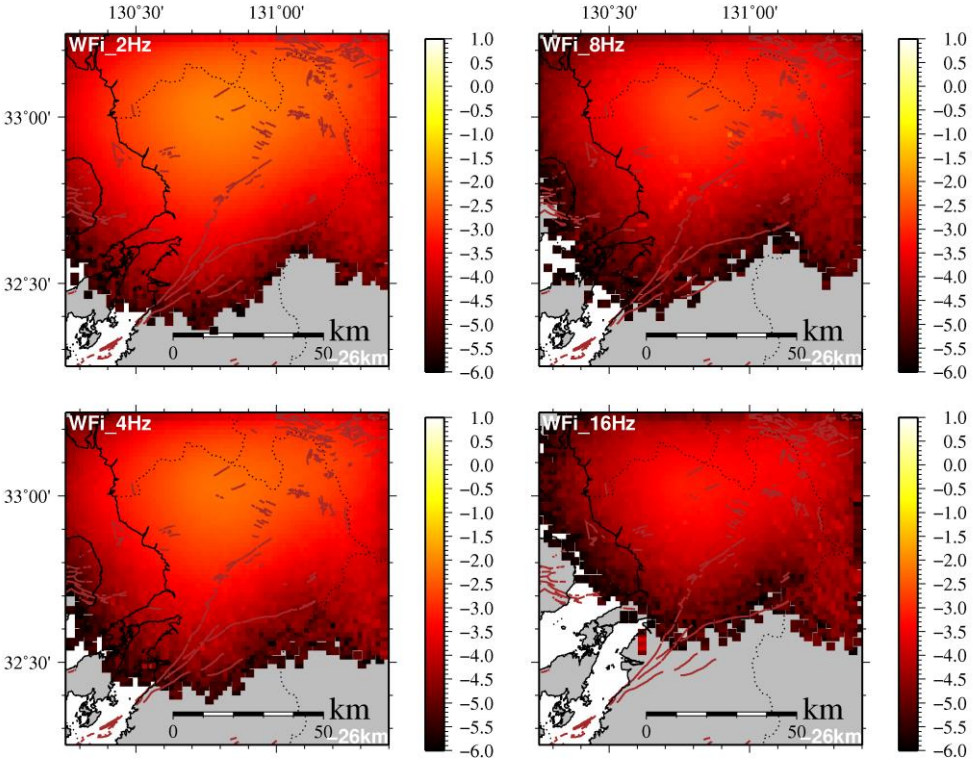

Figure 3.2.30 Same as Fig. 3.2.17 except depth = 26 km.

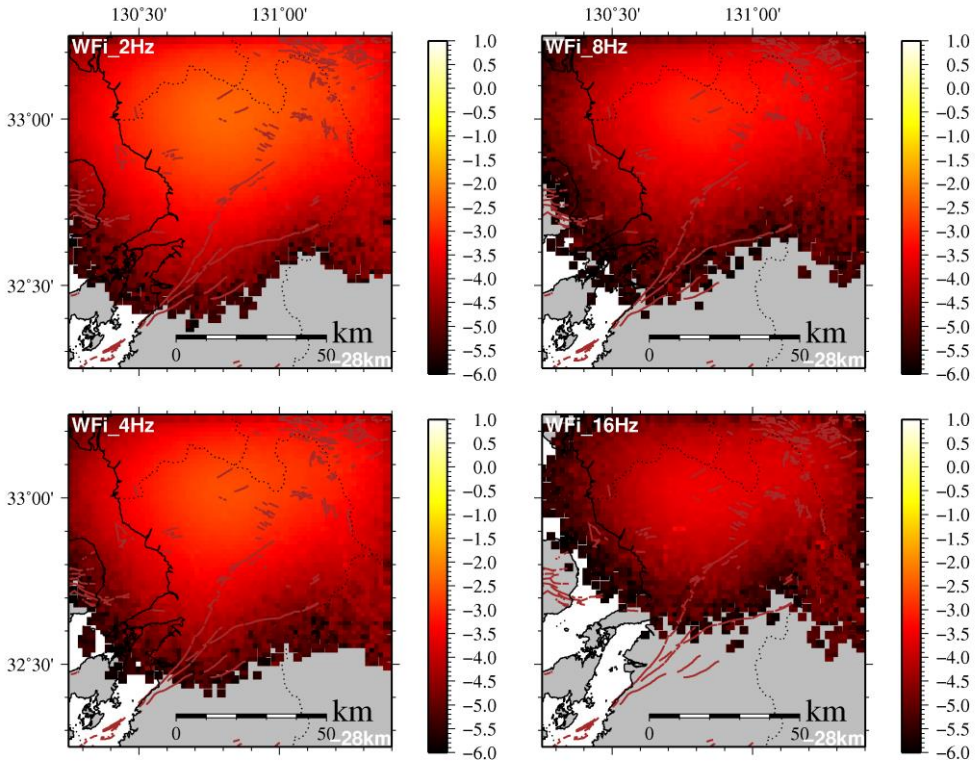

Figure 3.2.31 Same as Fig. 3.2.17 except depth = 28 km.

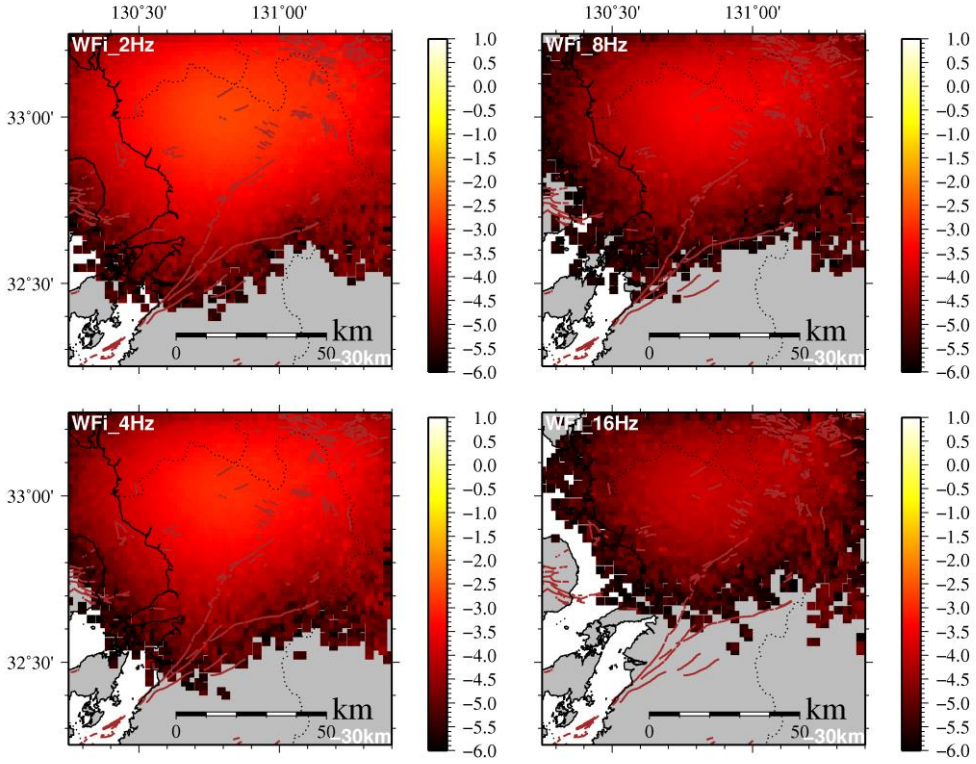

Figure 3.2.32 Same as Fig. 3.2.17 except depth = 30 km.

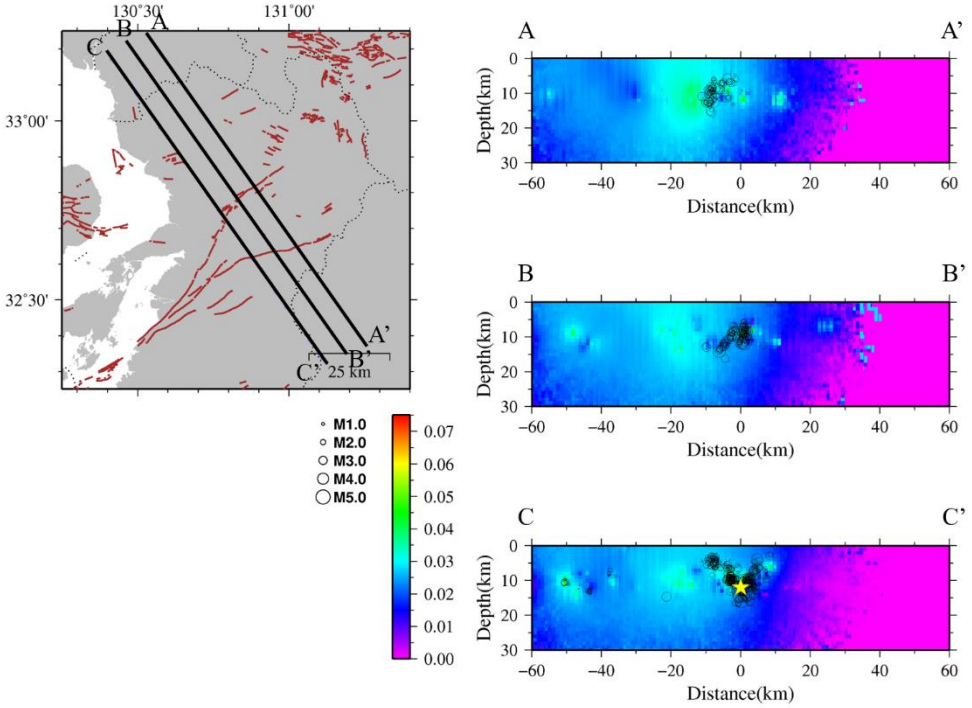

Figure 3.2.33 Cross-sections of the distribution of Q_i^{-1} at 2Hz. Left map shows the target area and right three panels correspond to the black solid lines shown on the left map. Color in the map indicates Q_i^{-1} value as shown in the scale bar at the center of the map. Solid circles indicate hypocenters of aftershocks of the 2016 Kumamoto earthquake.

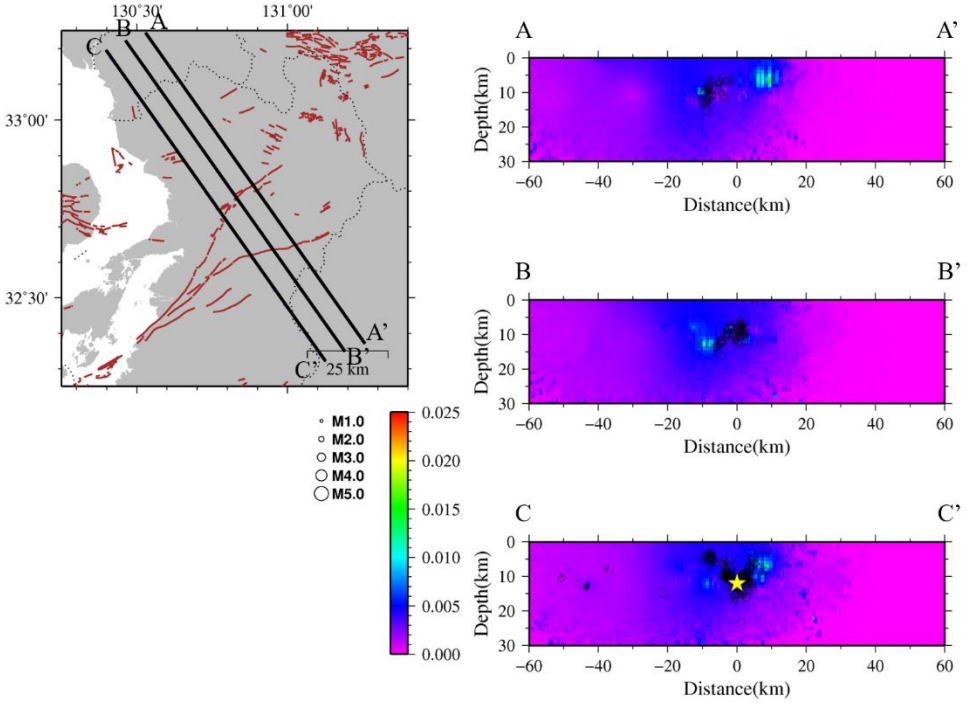

Figure 3.2.34 Same as Fig. 3.2.33 except frequency = 4Hz.

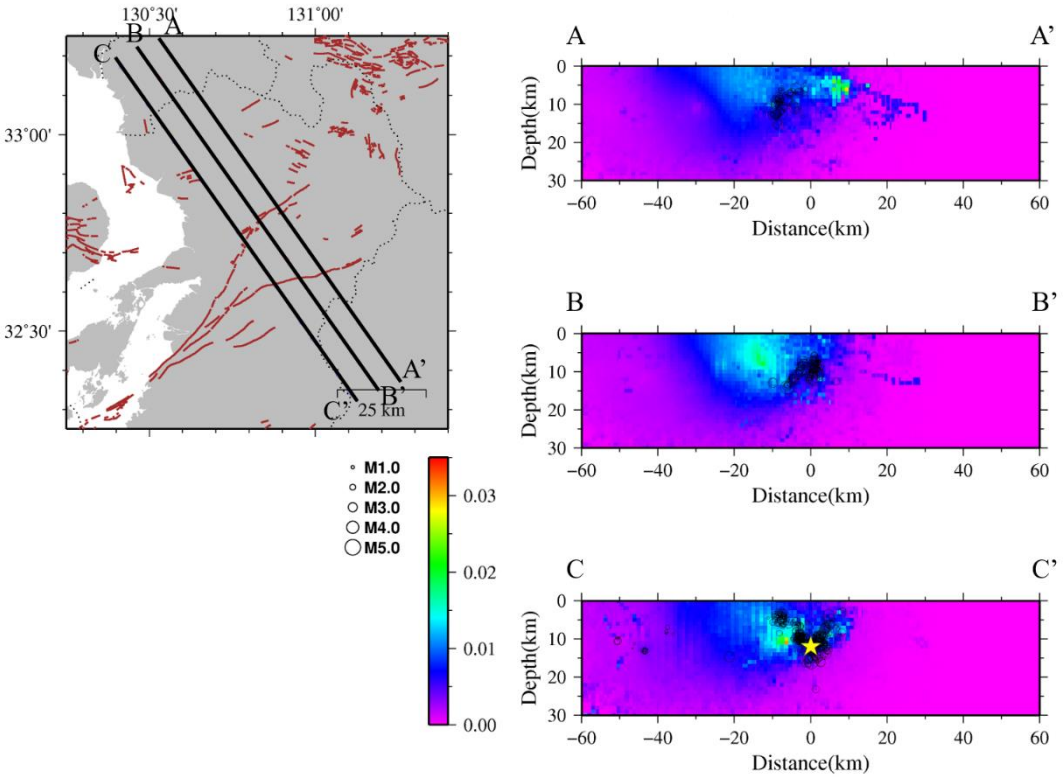

Figure 3.2.35 Same as Fig. 3.2.33 except frequency = 8Hz.

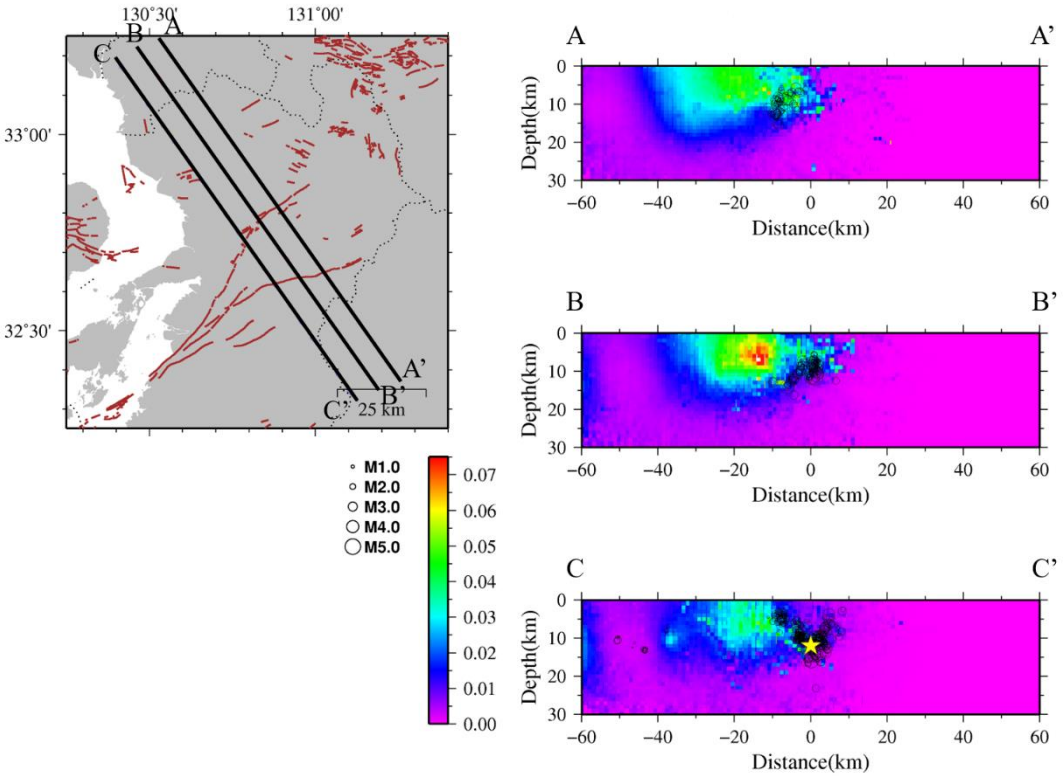

Figure 3.2.36 Same as Fig. 3.2.33 except frequency = 16Hz.

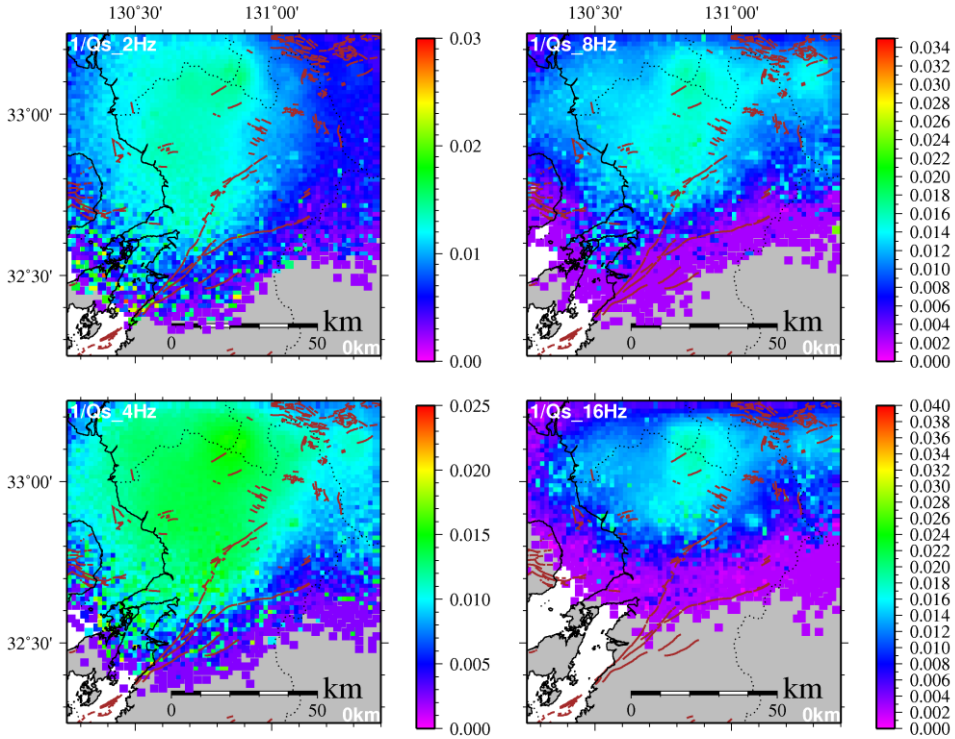

Figure 3.2.37 Map showing estimated Q_s^{-1} distribution at depth of 0 km. The result at four frequency ranges are displayed. Color in the map indicates Q_s^{-1} value as shown in the scale bar at the left of the map.

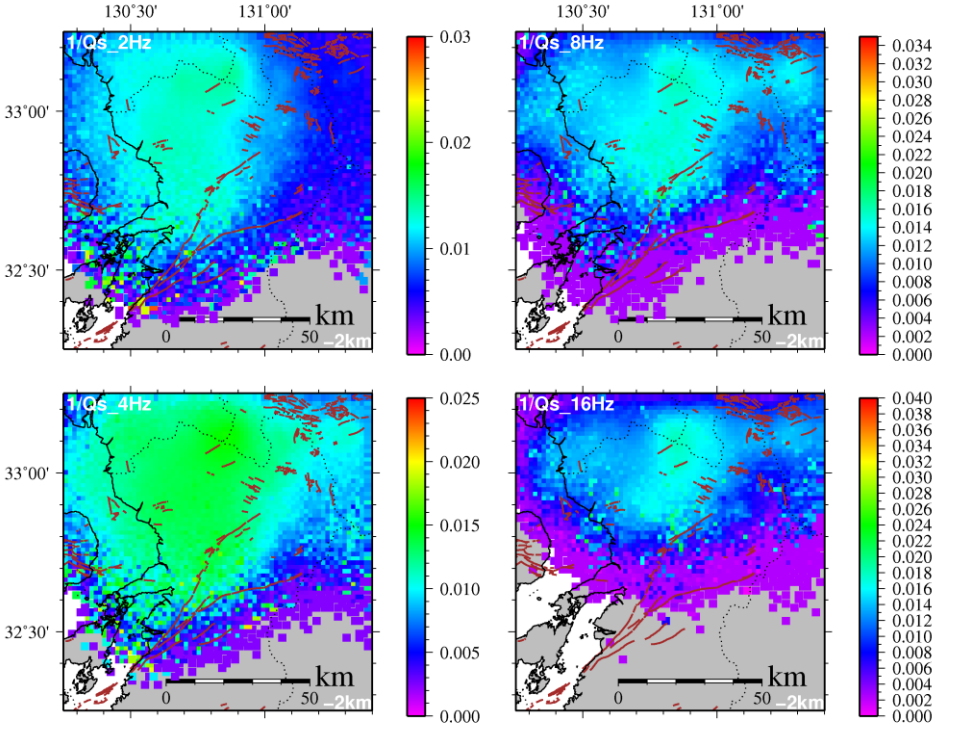

Figure 3.2.38 Same as Fig. 3.2.37 except depth = 2 km.

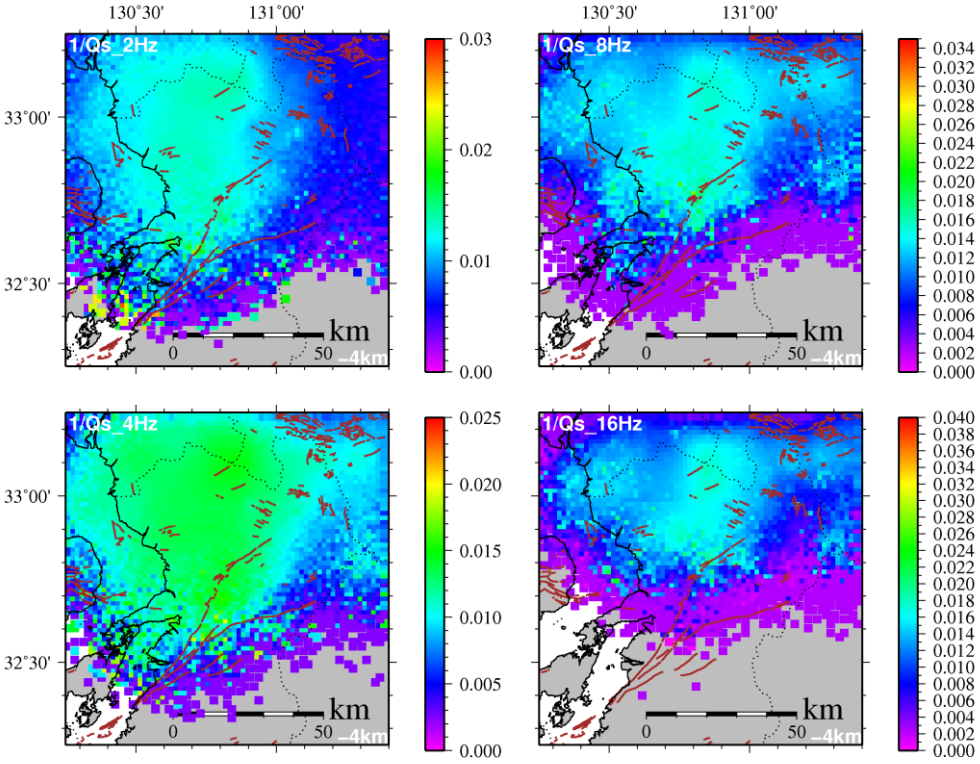

Figure 3.2.39 Same as Fig. 3.2.37 except depth = 4 km.

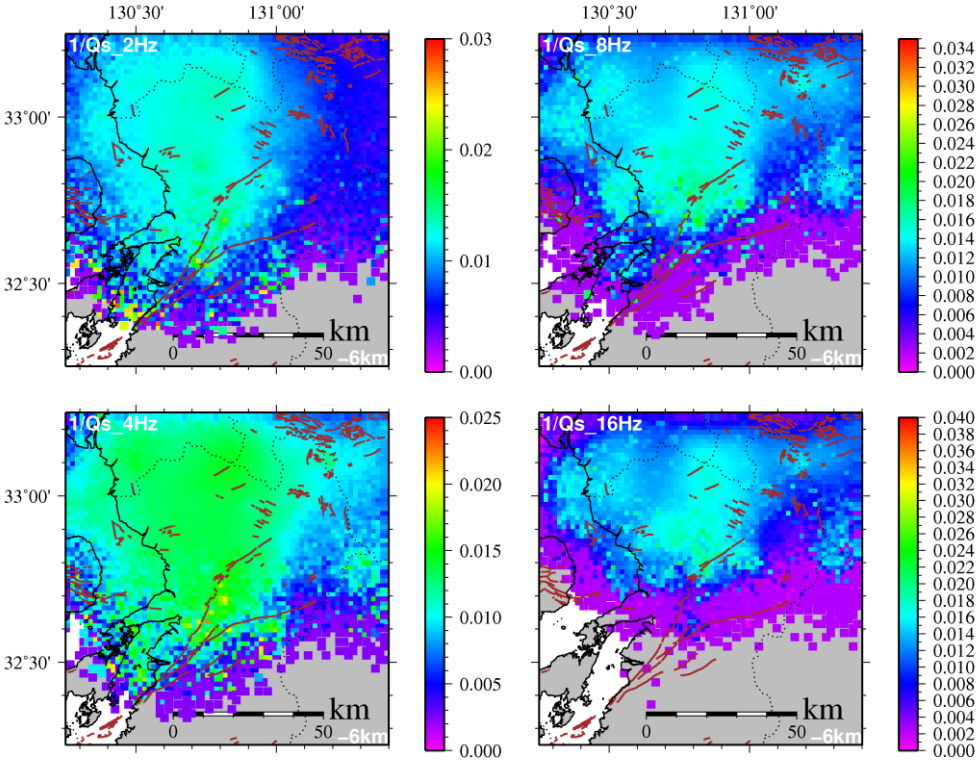

Figure 3.2.40 Same as Fig. 3.2.37 except depth = 6 km.

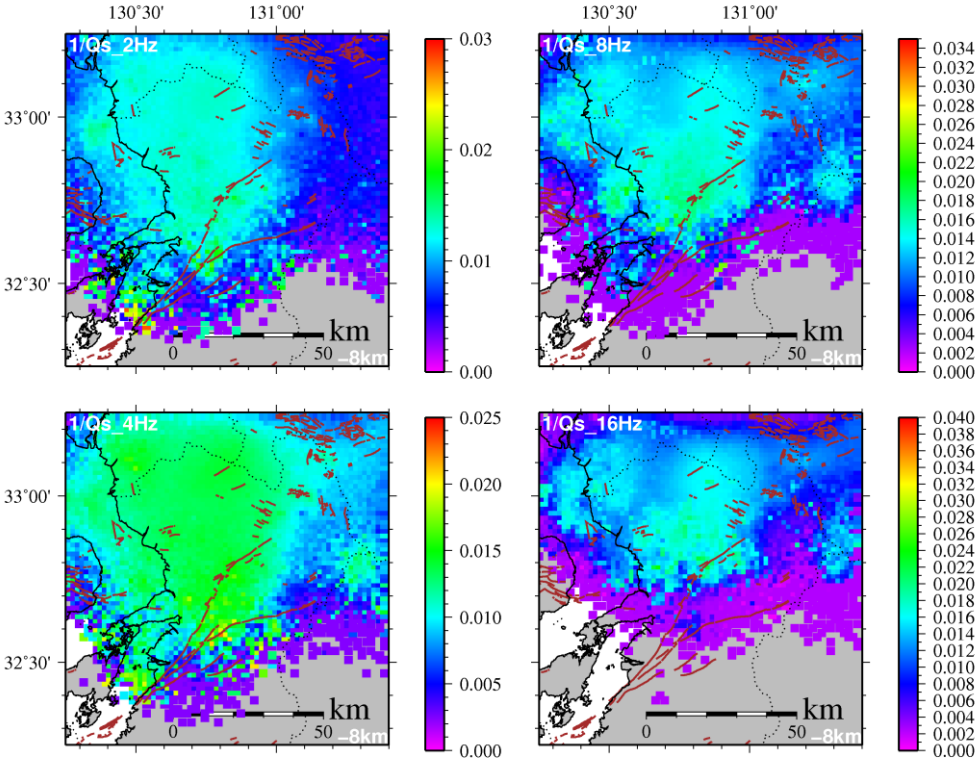

Figure 3.2.41 Same as Fig. 3.2.37 except depth = 8 km.

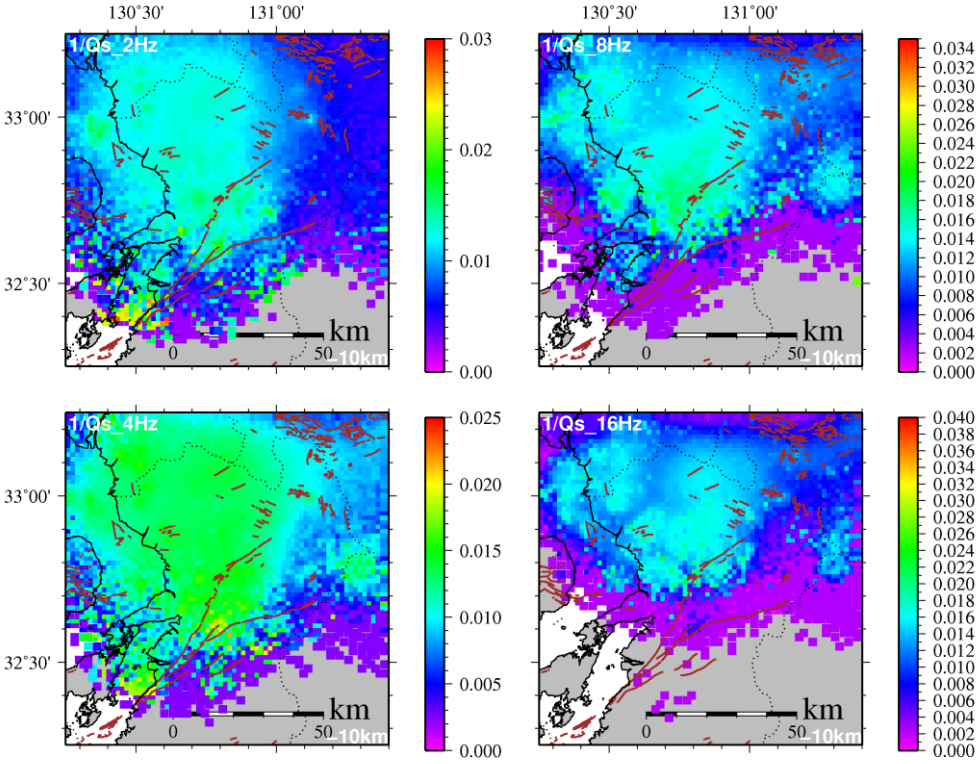

Figure 3.2.42 Same as Fig. 3.2.37 except depth = 10 km.

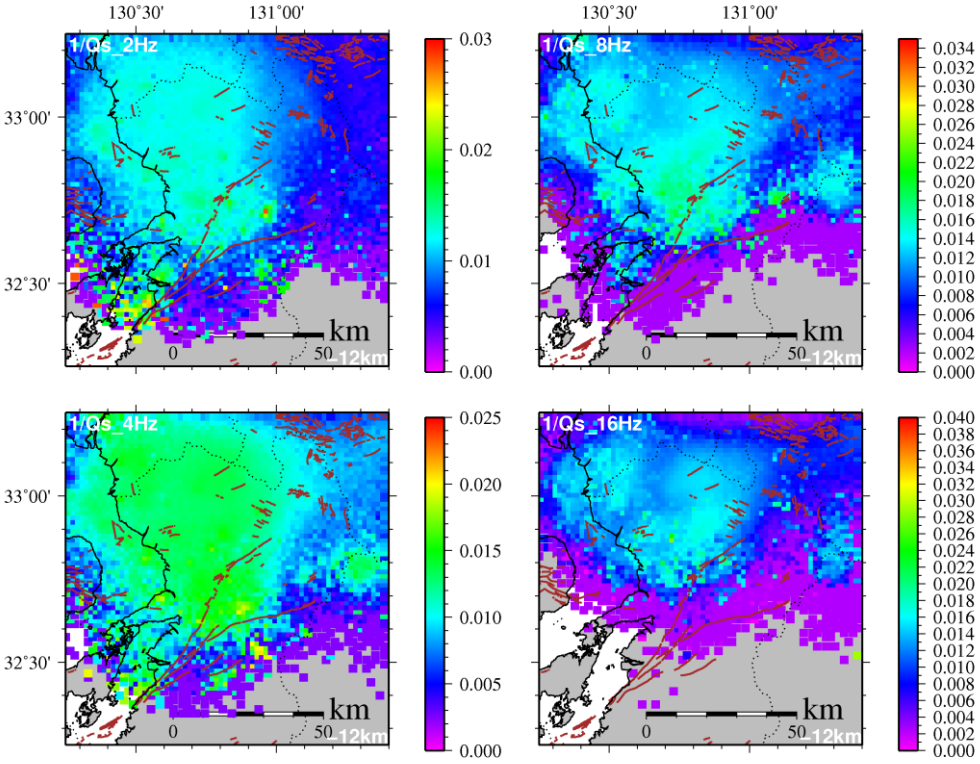

Figure 3.2.43 Same as Fig. 3.2.37 except depth = 12 km.

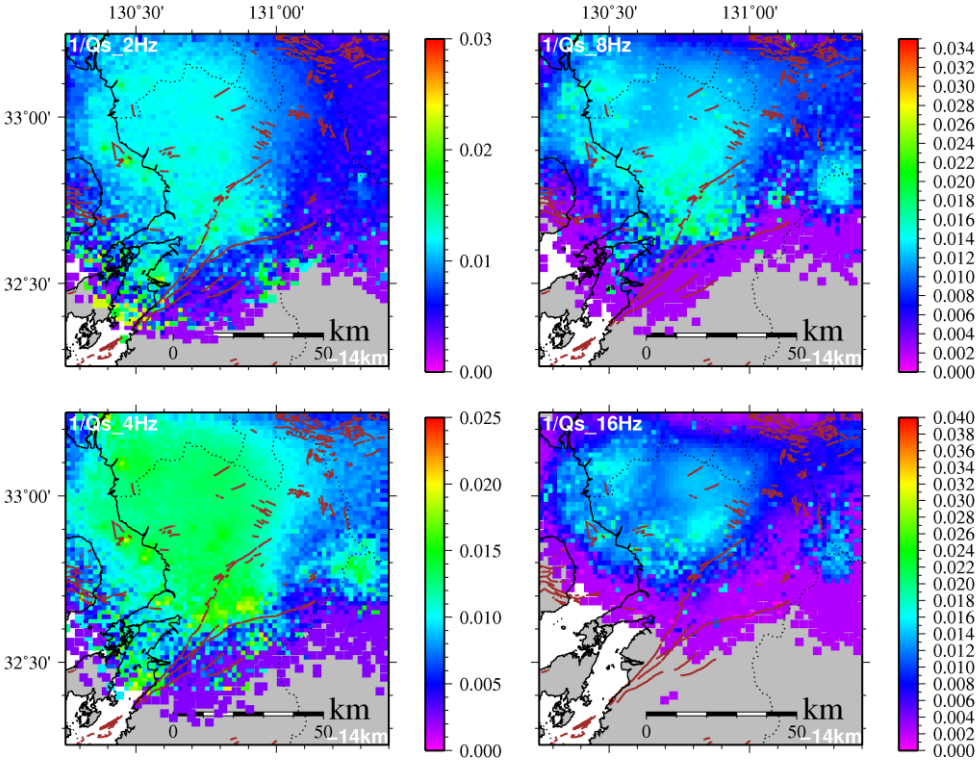

Figure 3.2.44 Same as Fig. 3.2.37 except depth = 14 km.

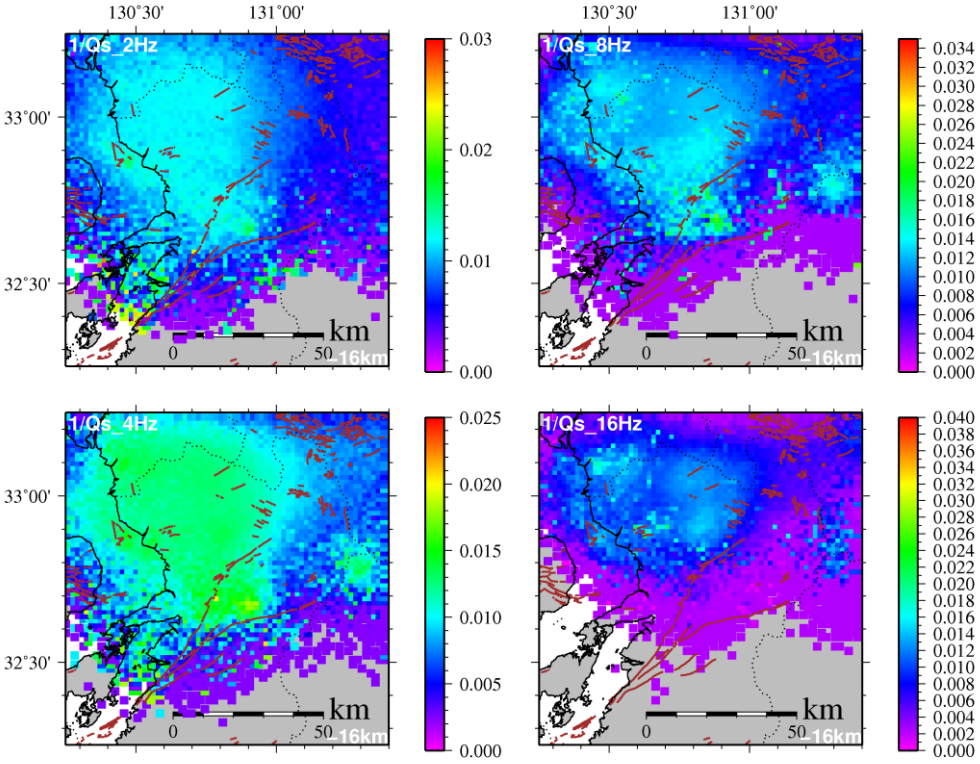

Figure 3.2.45 Same as Fig. 3.2.37 except depth = 16 km.

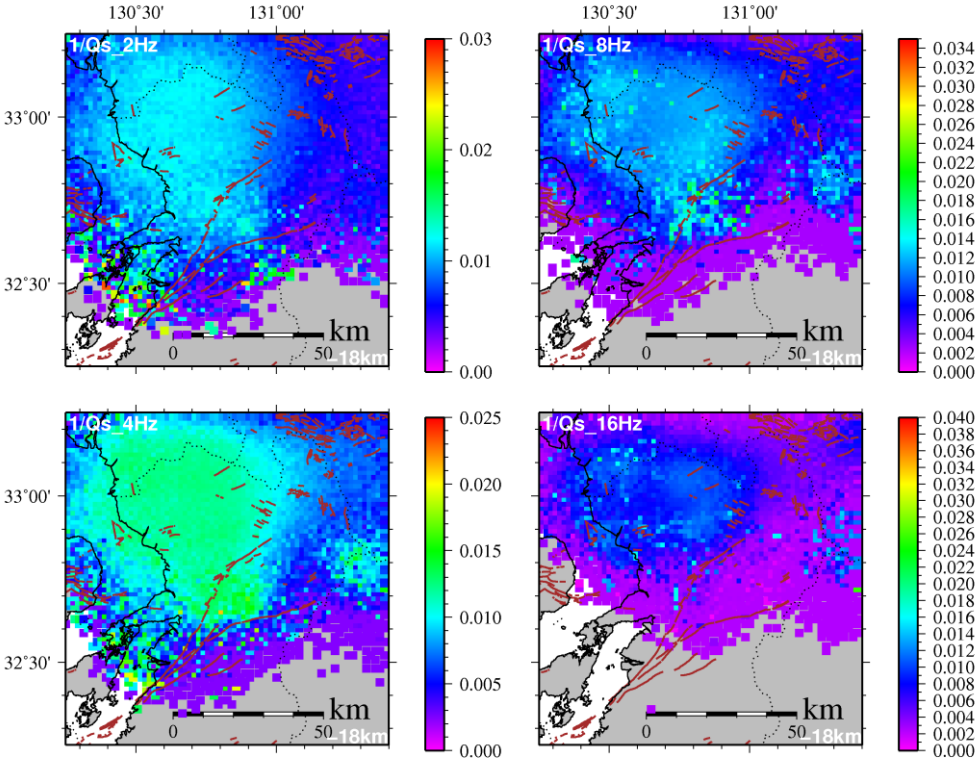

Figure 3.2.46 Same as Fig. 3.2.37 except depth = 18 km.

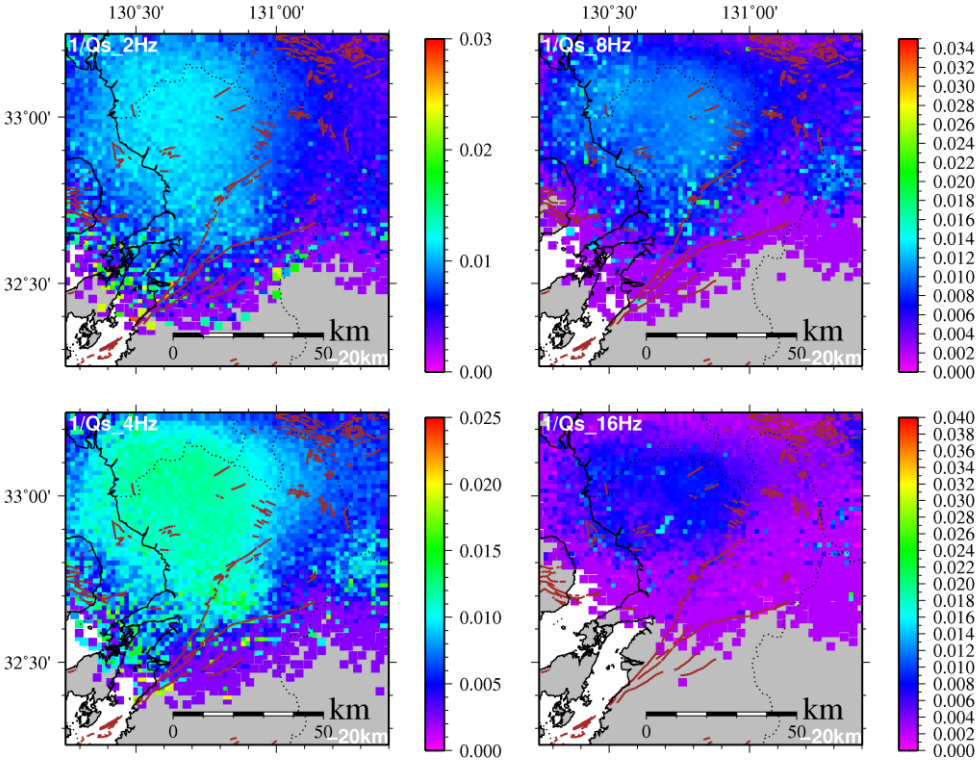

Figure 3.2.47 Same as Fig. 3.2.37 except depth = 20 km.

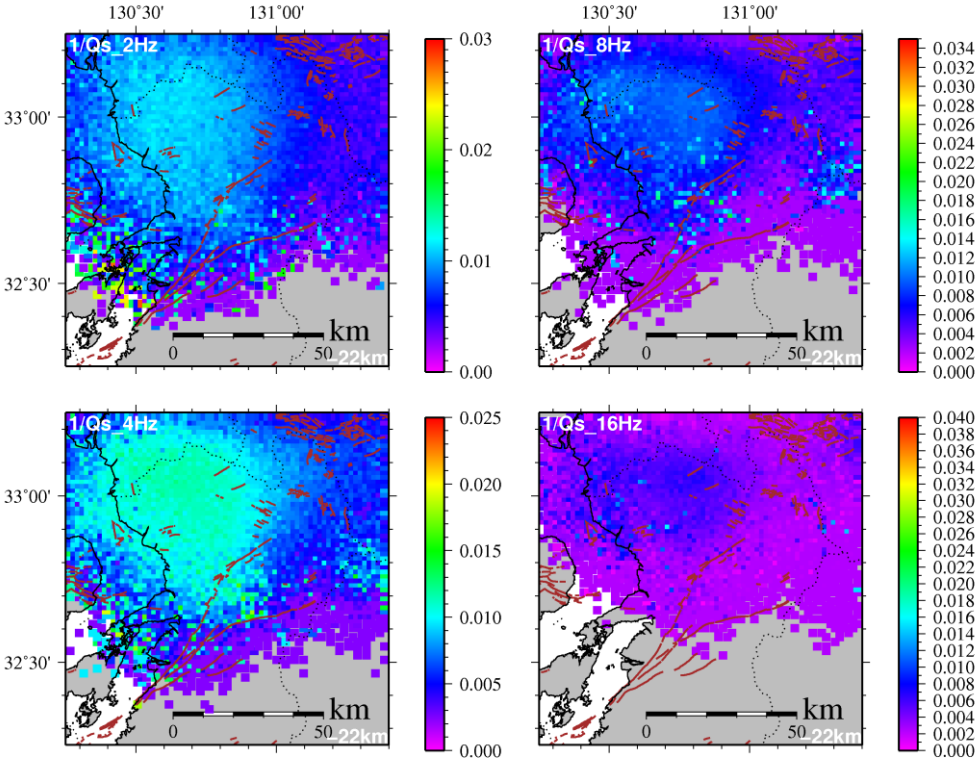

Figure 3.2.48 Same as Fig. 3.2.37 except depth = 22 km.

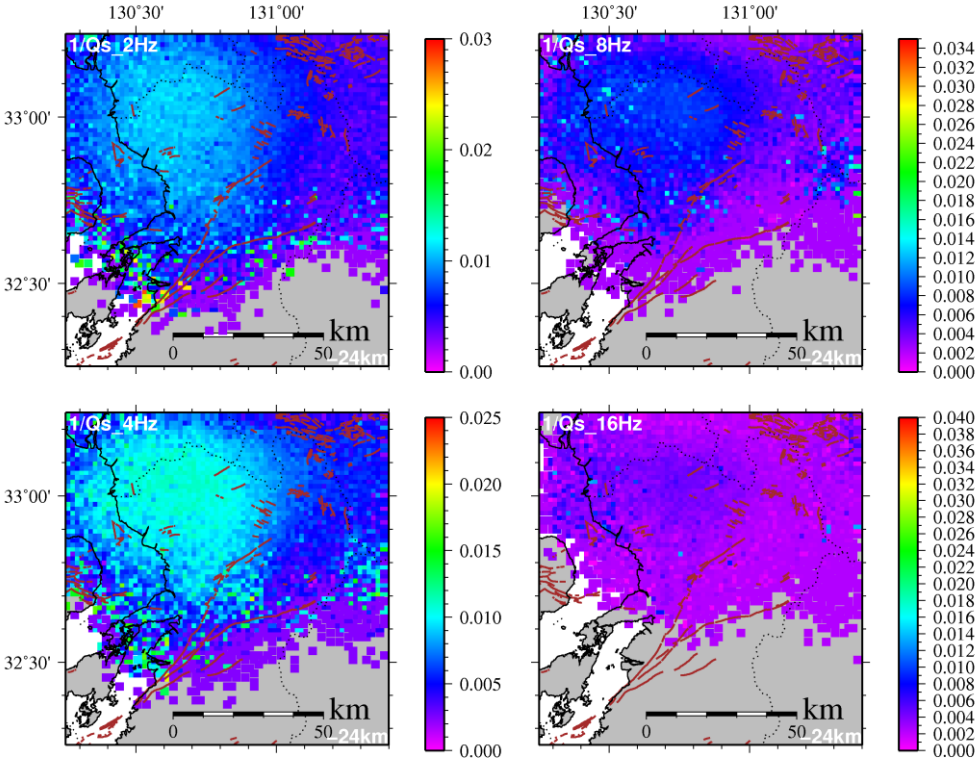

Figure 3.2.49 Same as Fig. 3.2.37 except depth = 24 km.

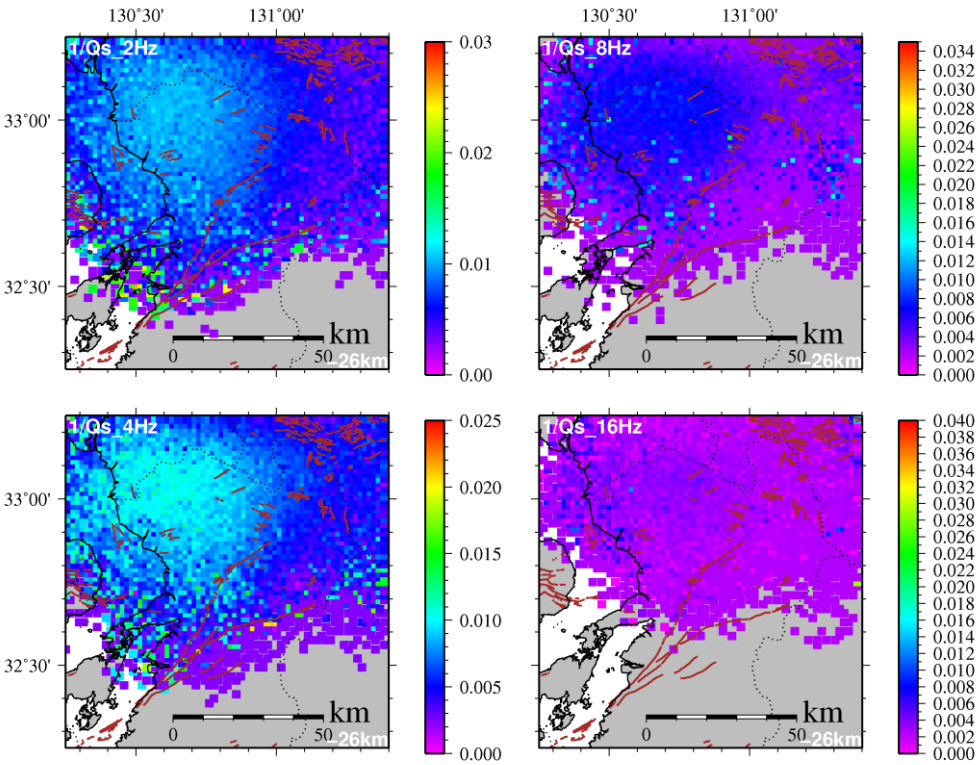

Figure 3.2.50 Same as Fig. 3.2.37 except depth = 26 km.

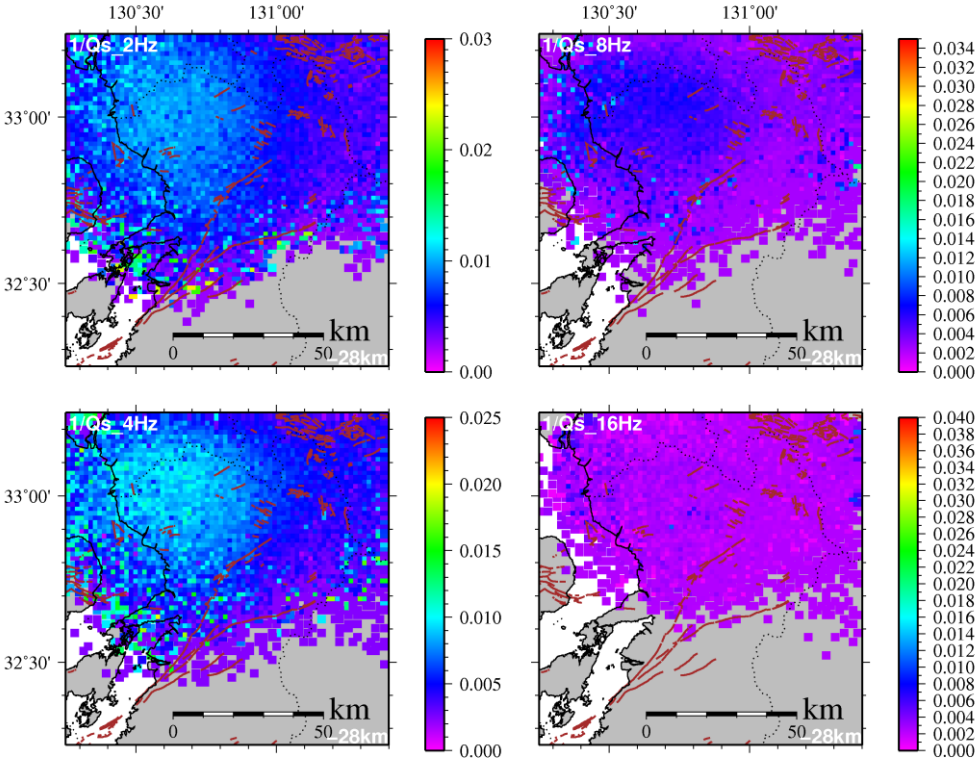

Figure 3.2.51 Same as Fig. 3.2.37 except depth = 28 km.

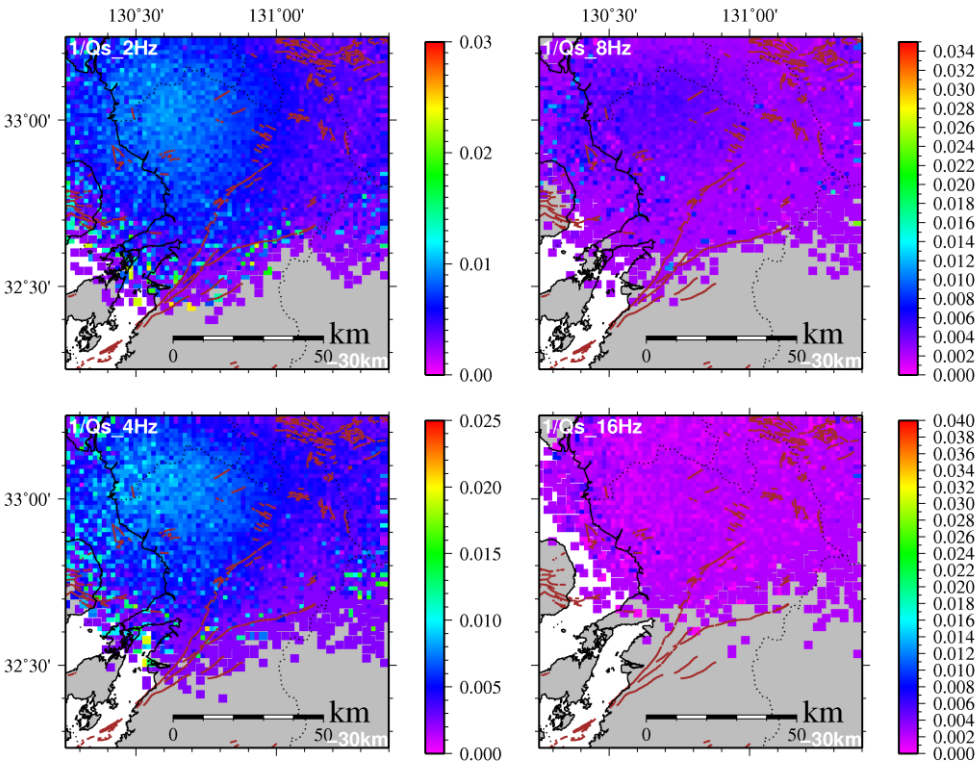

Figure 3.2.52 Same as Fig. 3.2.37 except depth = 30 km.

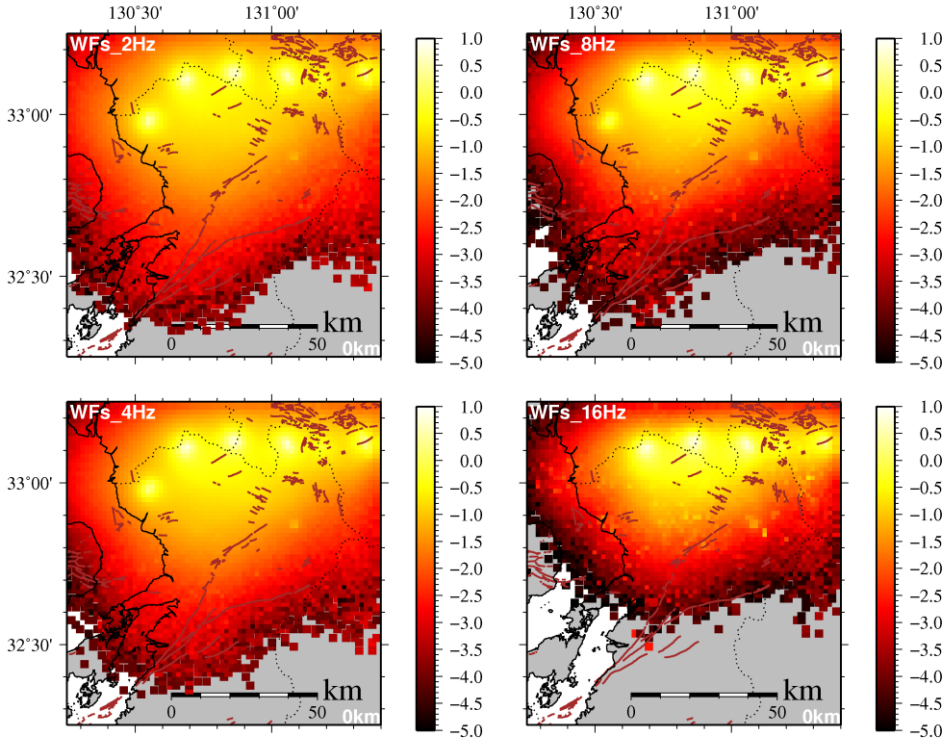

Figure 3.2.53 Map showing the weight distribution of Q_s^{-1} at depth 0 km. The result at four frequency ranges are displayed. Colors in the map indicates Q_s^{-1} value as shown in the scale bar at the left of the map.

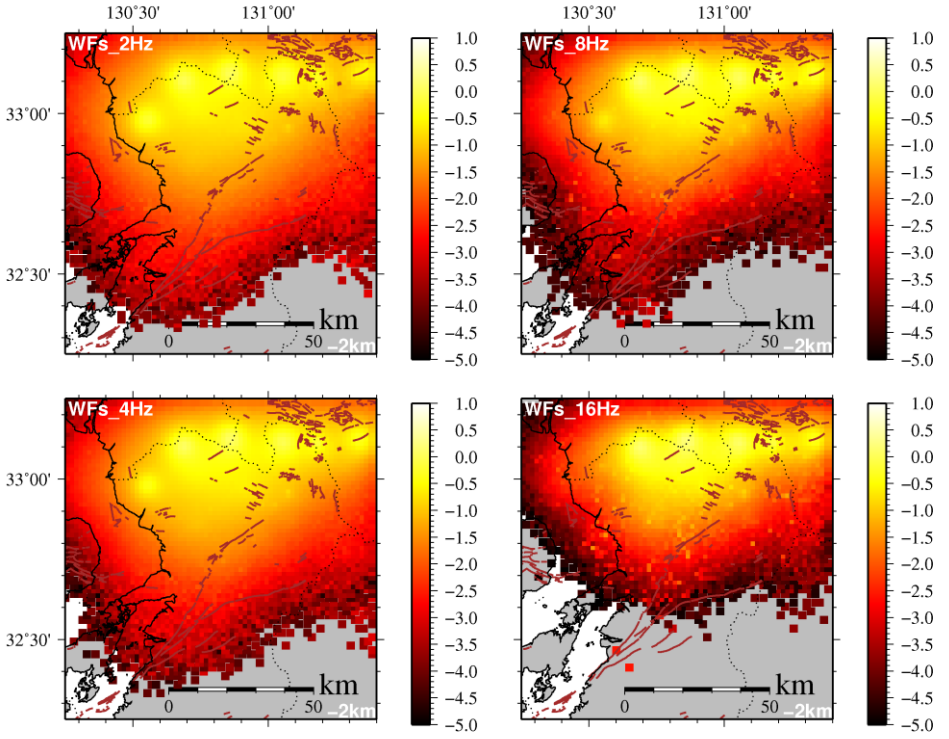

Figure 3.2.54 Same as Fig. 3.2.53 except depth = 2 km.

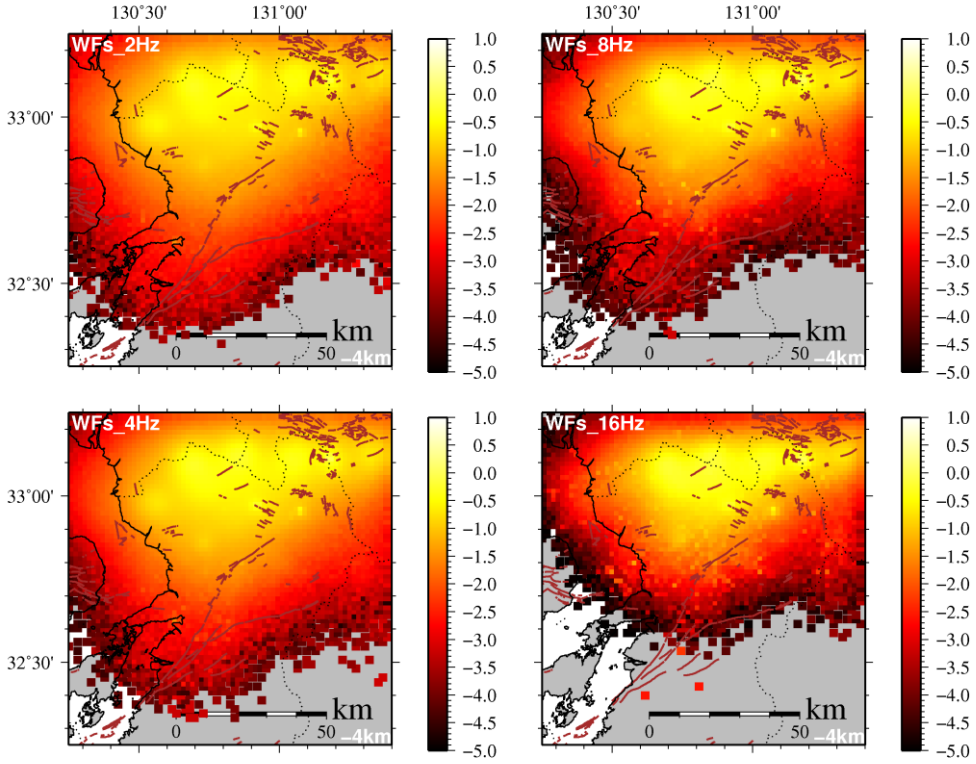

Figure 3.2.55 Same as Fig. 3.2.53 except depth = 4 km.

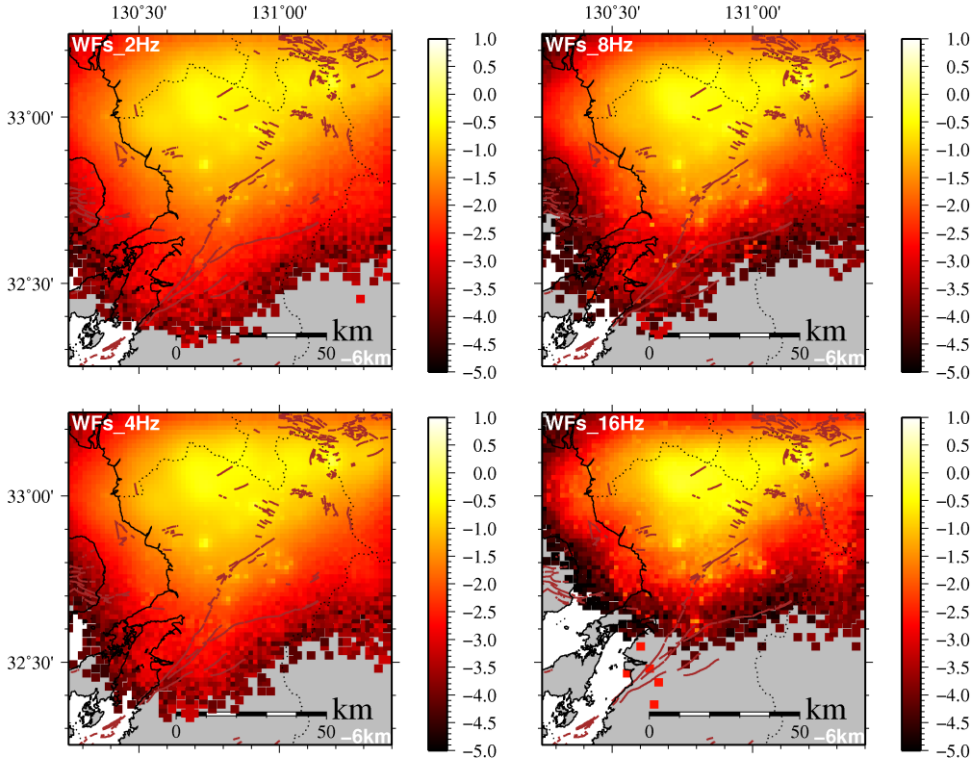

Figure 3.2.56 Same as Fig. 3.2.53 except depth = 6 km.

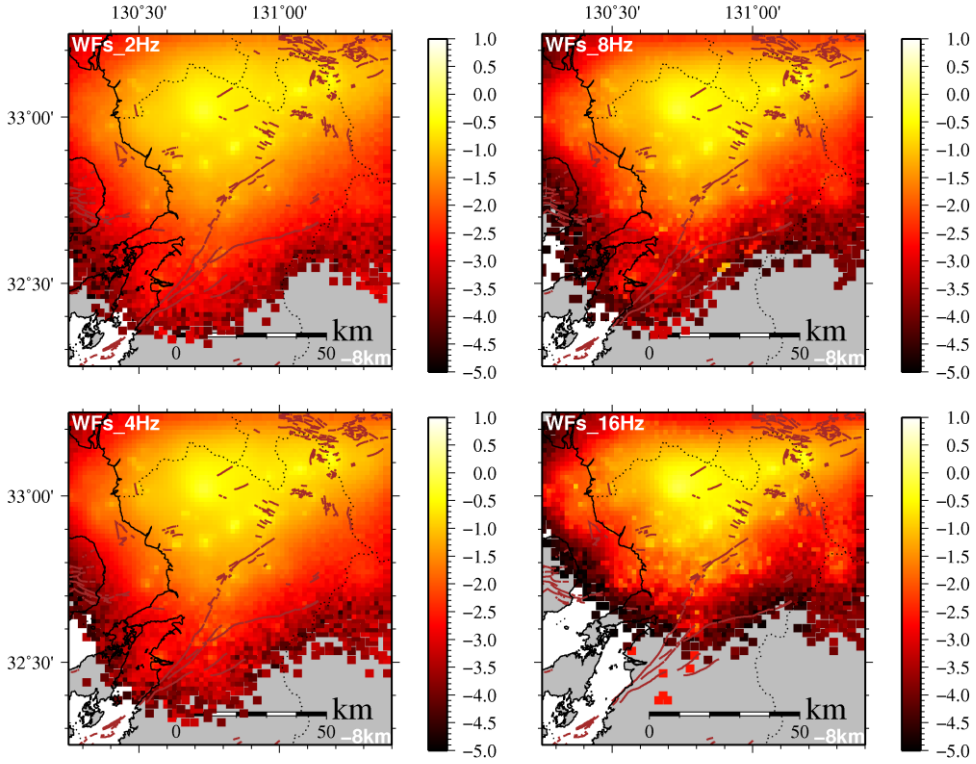

Figure 3.2.57 Same as Fig. 3.2.53 except depth = 8 km.

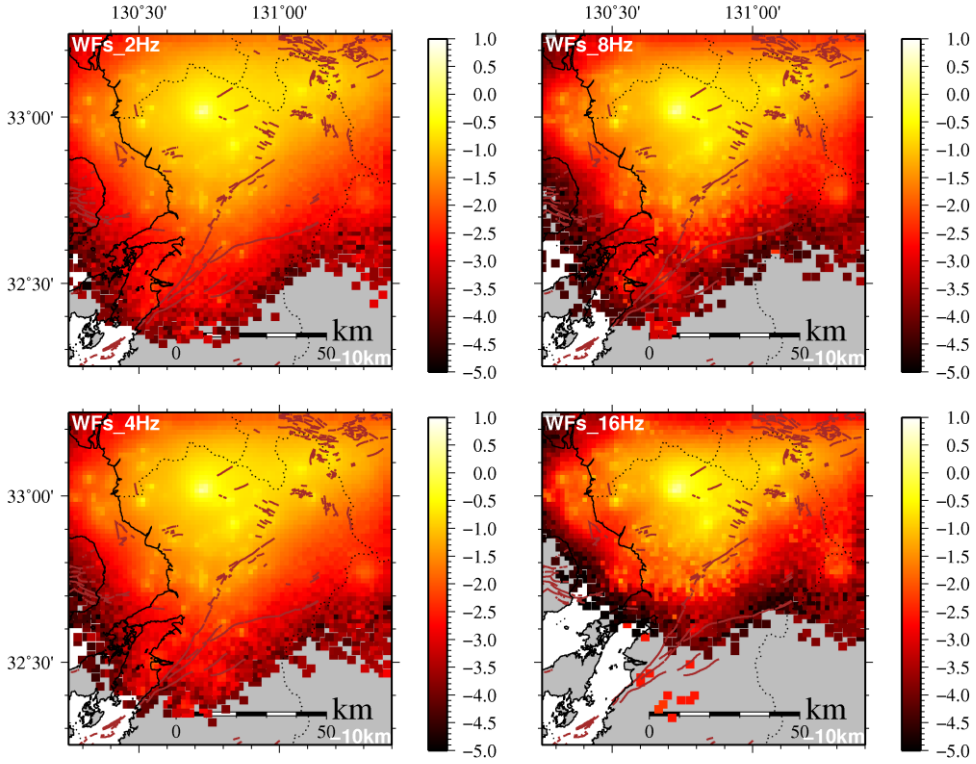

Figure 3.2.58 Same as Fig. 3.2.53 except depth = 10 km.

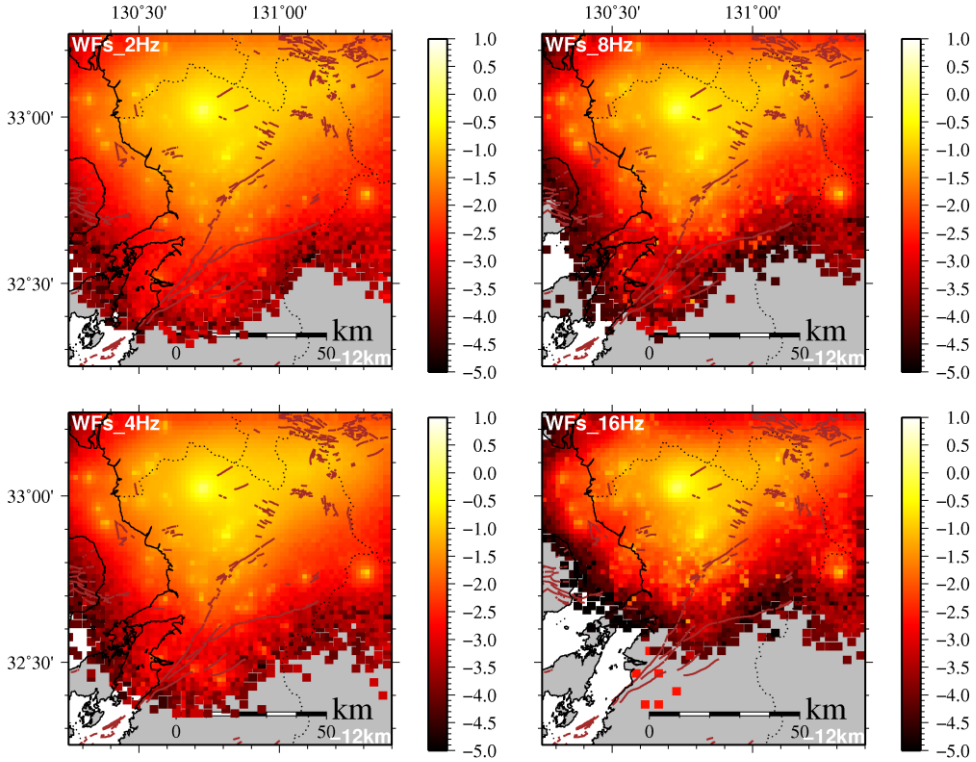

Figure 3.2.59 Same as Fig. 3.2.53 except depth = 12 km.

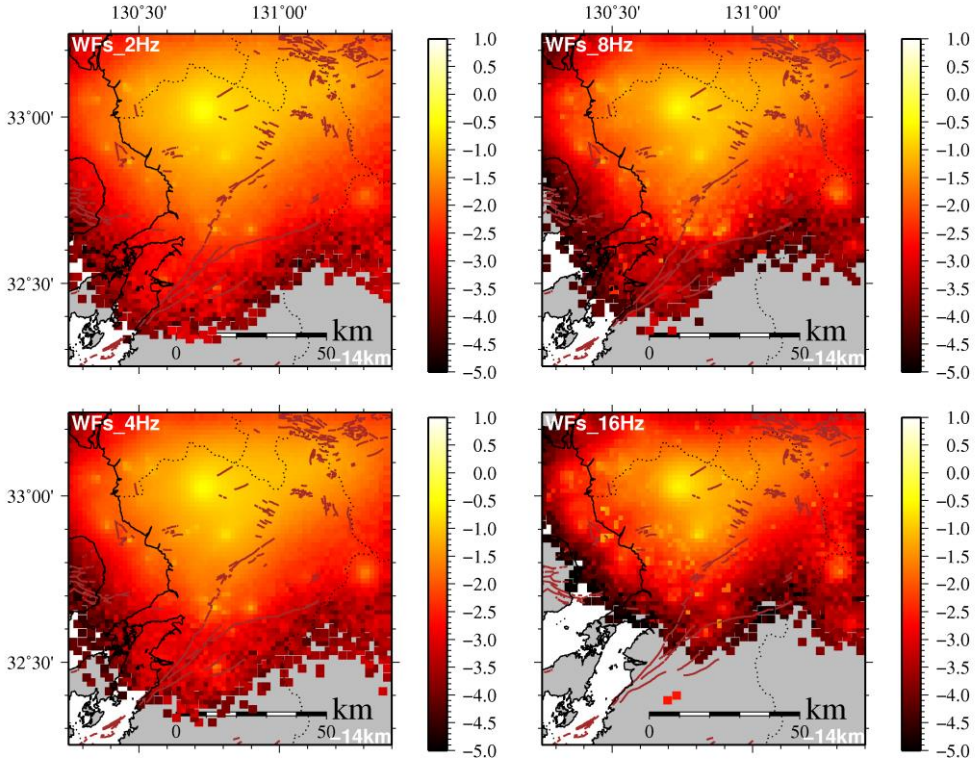

Figure 3.2.60 Same as Fig. 3.2.53 except depth = 14 km.

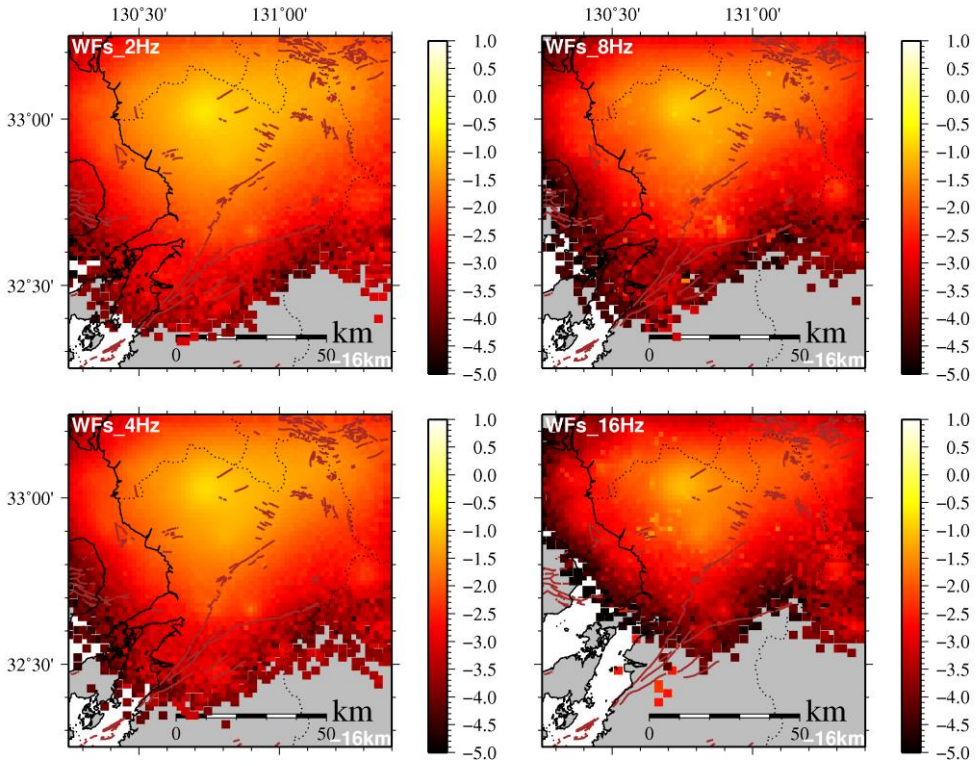

Figure 3.2.61 Same as Fig. 3.2.53 except depth = 16 km.

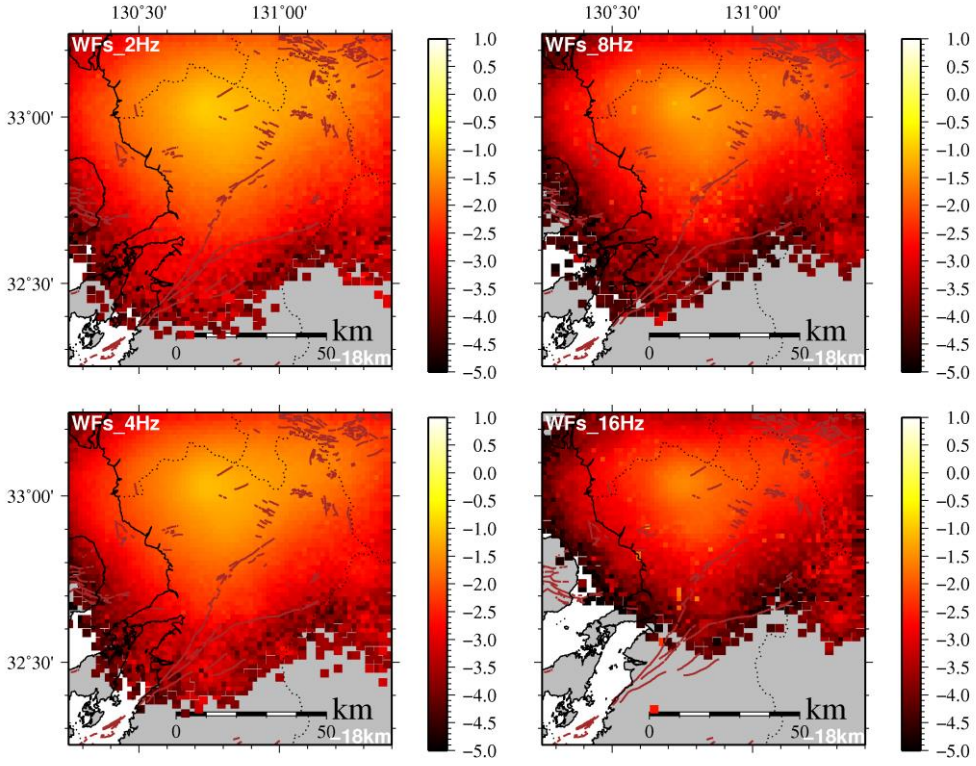

Figure 3.2.62 Same as Fig. 3.2.53 except depth = 18 km.

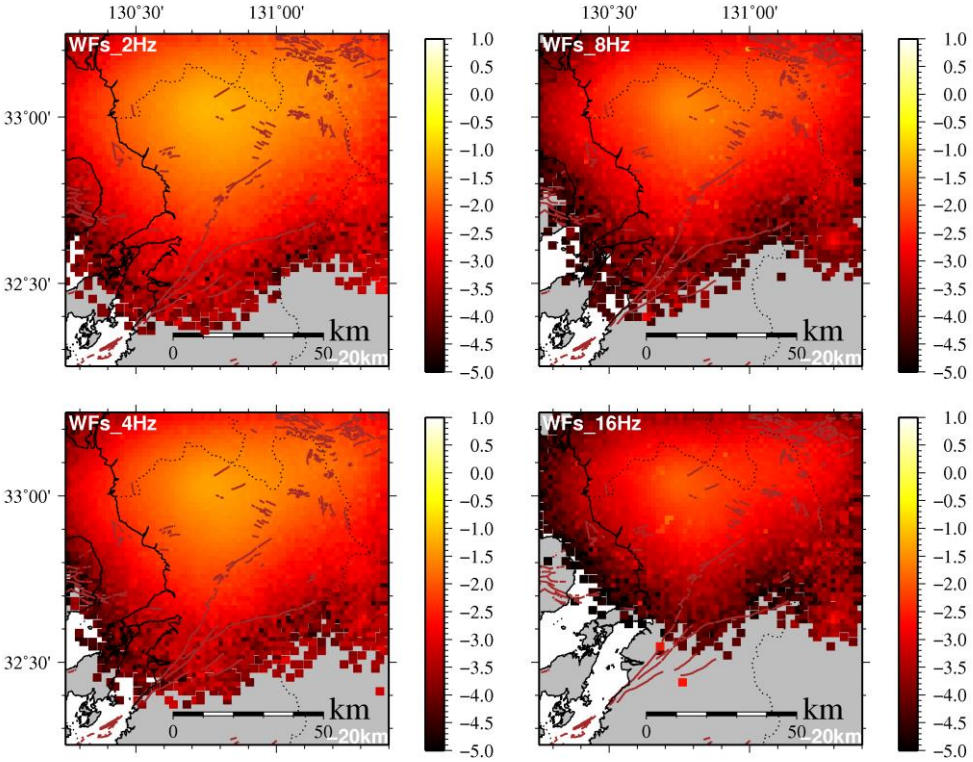

Figure 3.2.63 Same as Fig. 3.2.53 except depth = 20 km.

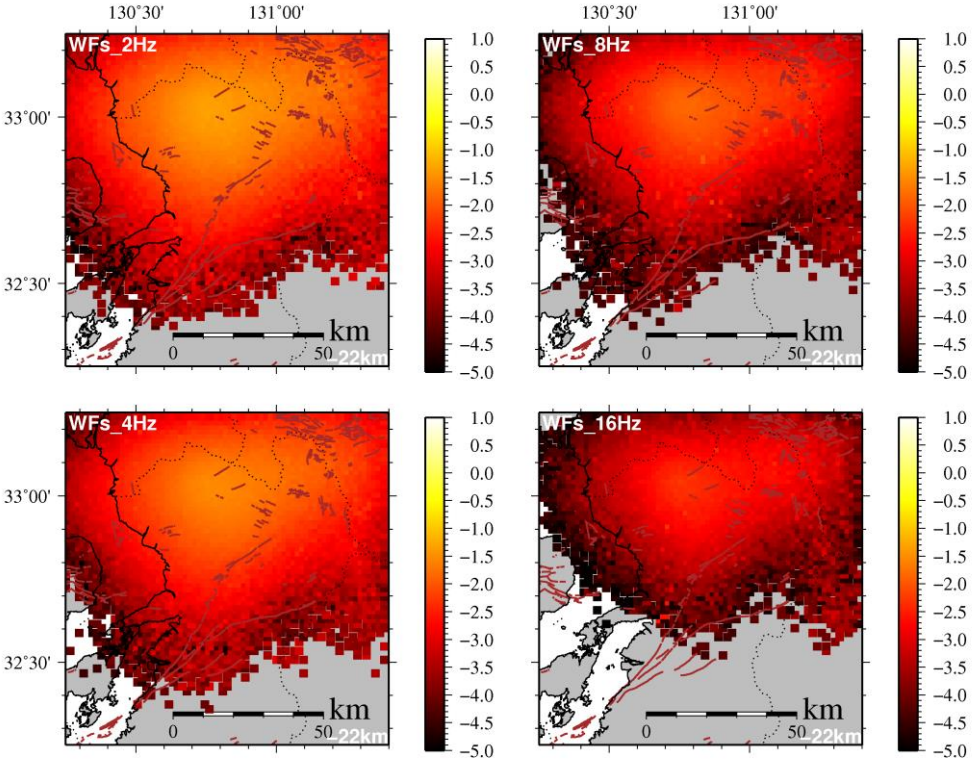

Figure 3.2.64 Same as Fig. 3.2.53 except depth = 22 km.

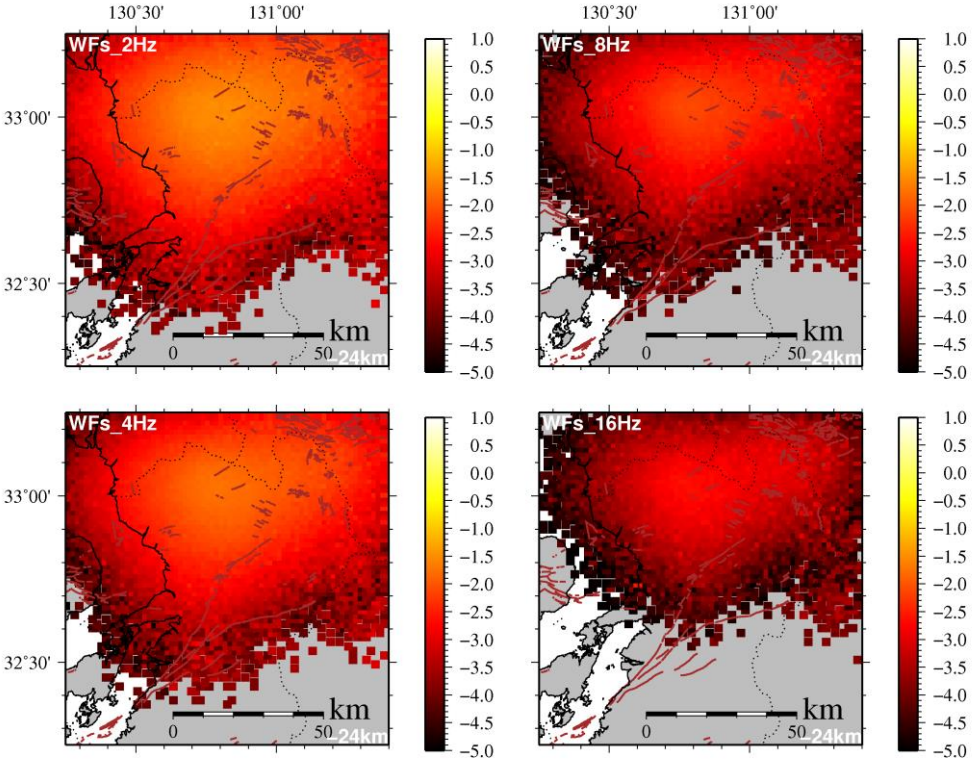

Figure 3.2.65 Same as Fig. 3.2.53 except depth = 24 km.

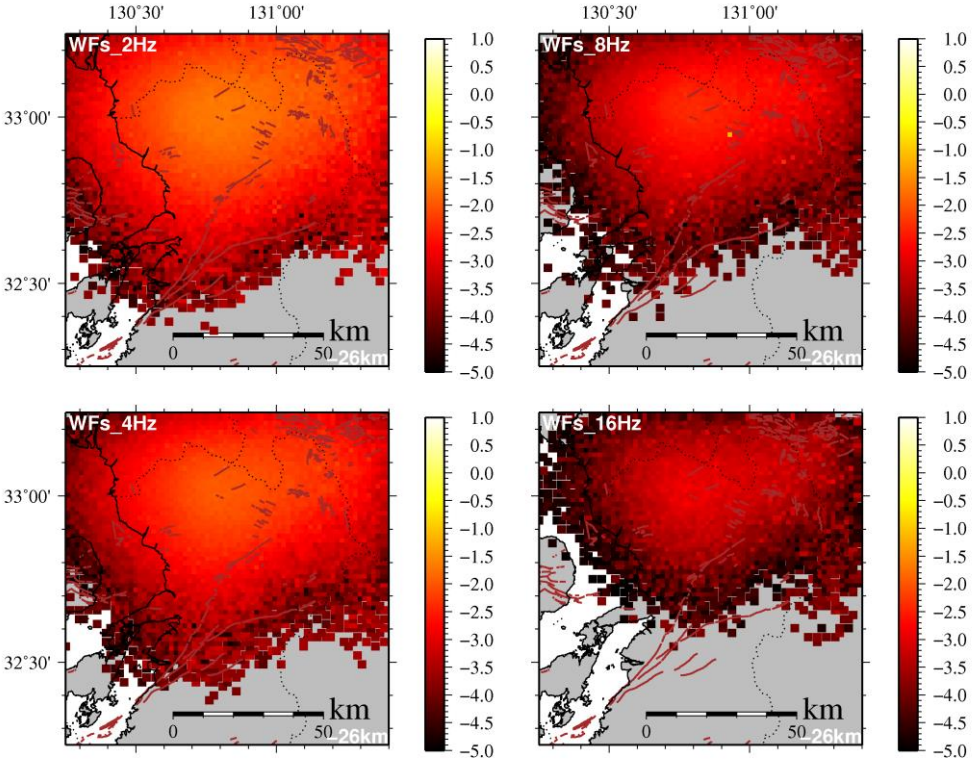

Figure 3.2.66 Same as Fig. 3.2.53 except depth = 26 km.

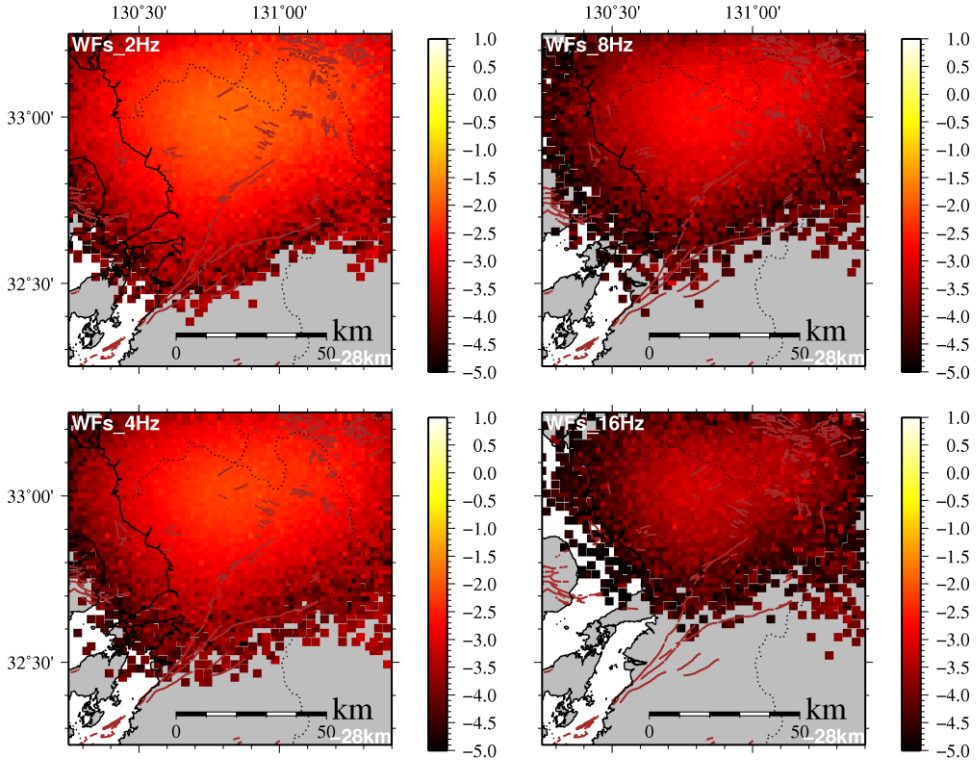

Figure 3.2.67 Same as Fig. 3.2.53 except depth = 28 km.

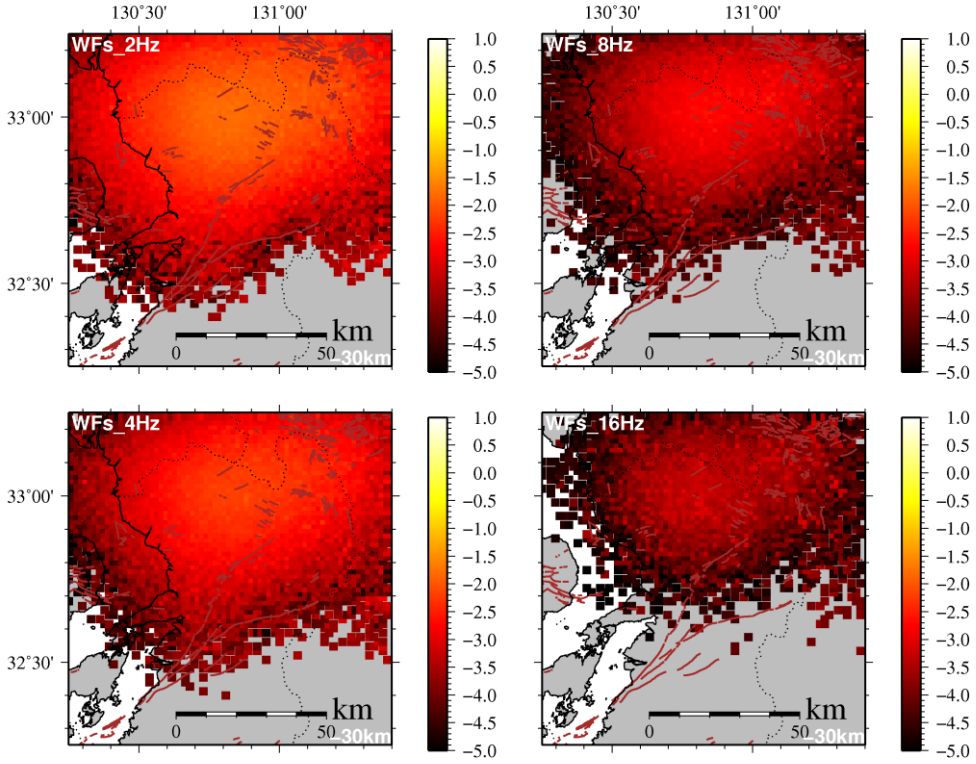

Figure 3.2.68 Same as Fig. 3.2.53 except depth = 30 km.

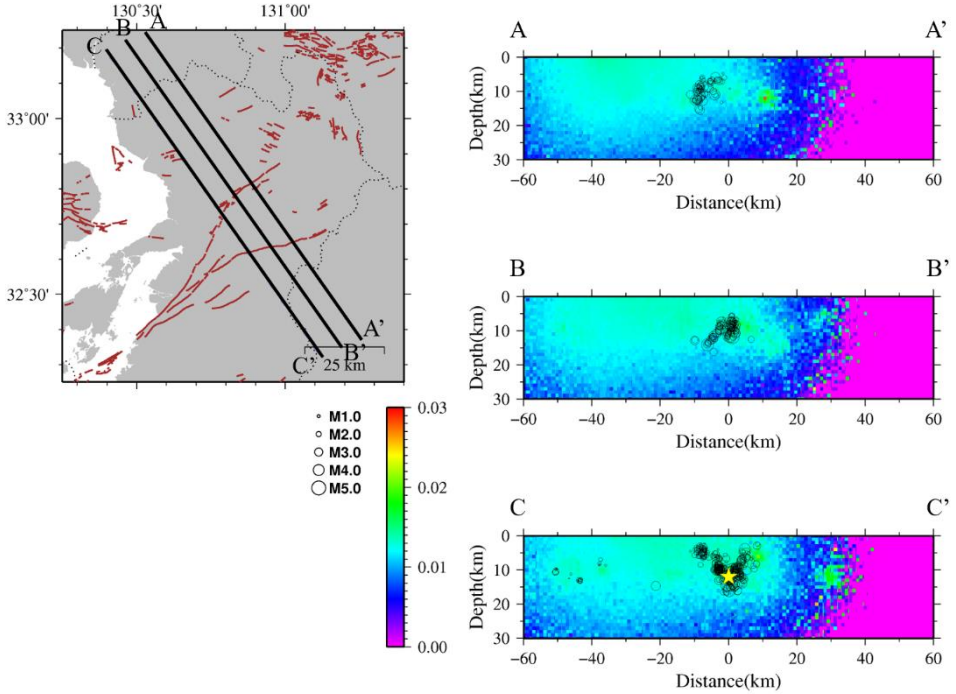

Figure 3.2.33 Cross-sections of the distribution of Q_s^{-1} at 2Hz. Left map shows the target area and right three panels correspond to the black solid lines shown on the left map. Color in the map indicates Q_s^{-1} value as shown in the scale bar at the center of the map. Solid circles indicate hypocenters of aftershocks of the 2016 Kumamoto earthquake.

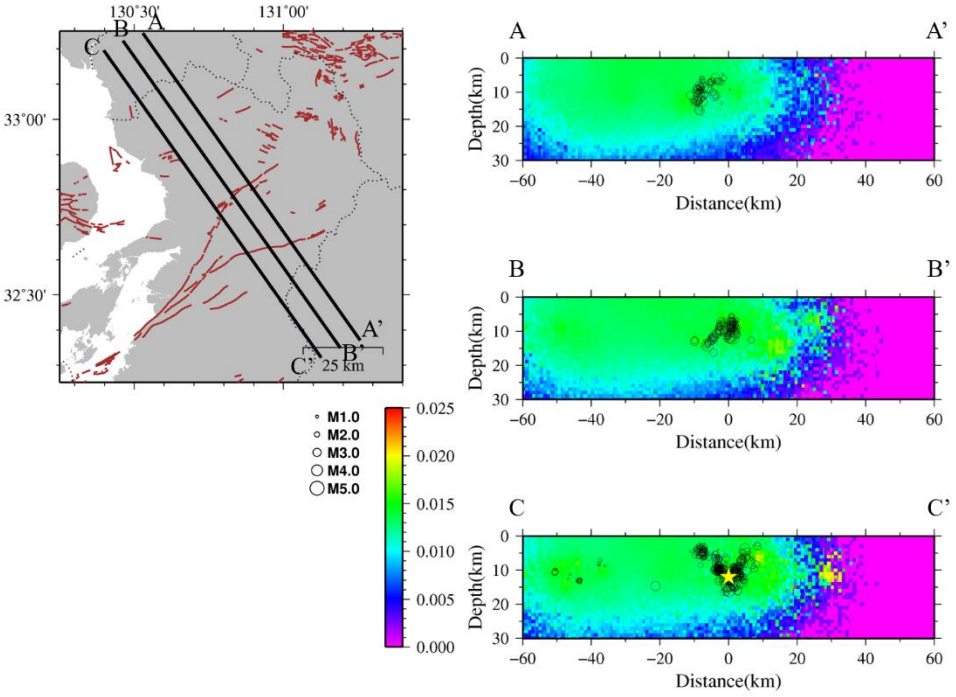

Figure 3.2.70 Same as Fig. 3.2.69 except frequency = 4Hz.

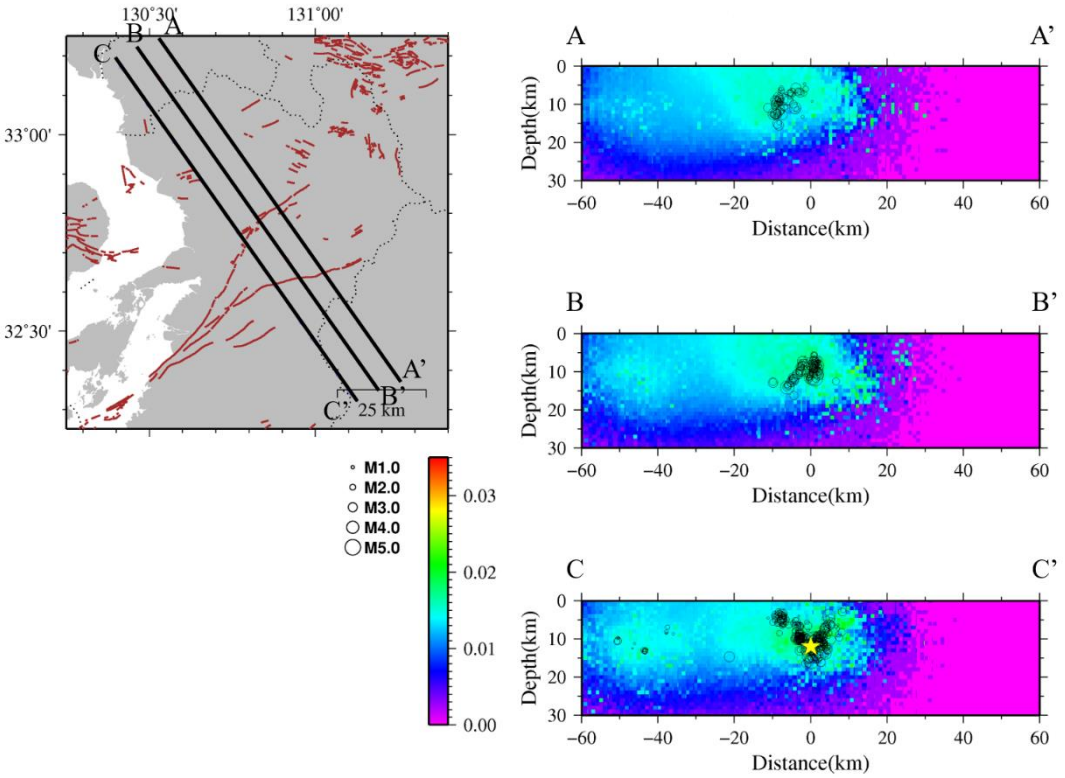

Figure 3.2.71 Same as Fig. 3.2.69 except frequency = 8Hz.

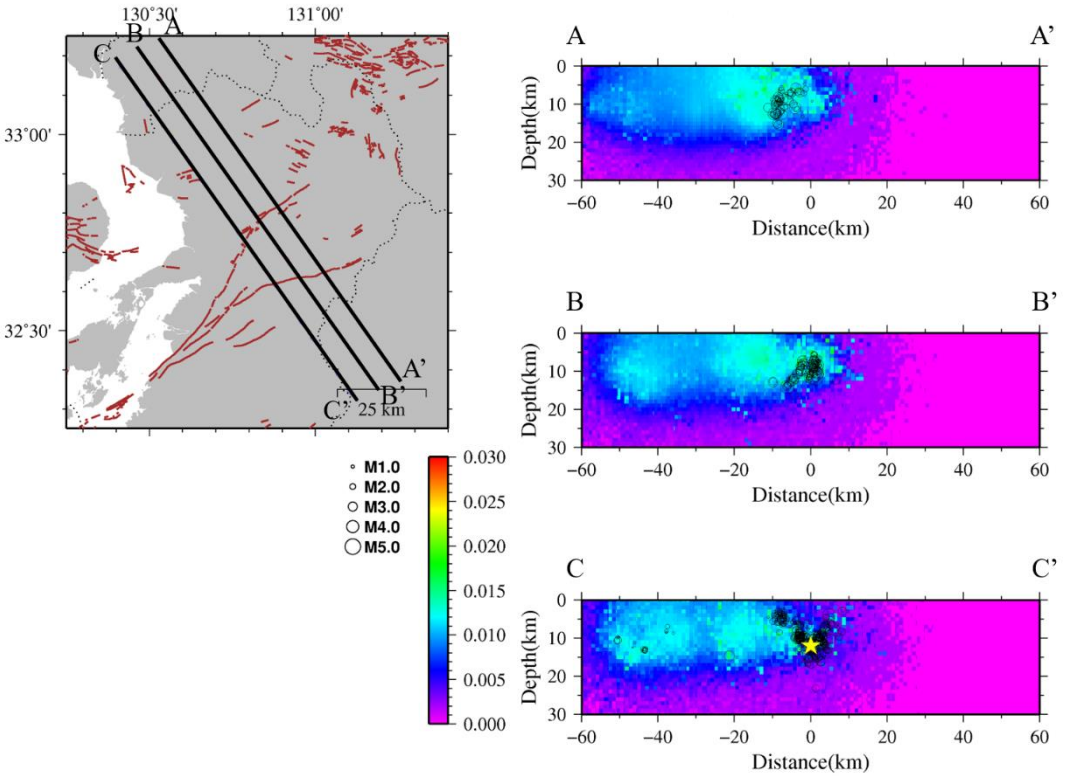

Figure 3.2.72 Same as Fig. 3.2.69 except frequency = 16Hz.

3.3 Strong scatterer

As described chapter 2.4, we estimate location of scatters with strong scattering coefficient from lapse time of ripple extracted the average envelope, locations of hypocenter and stations. S wave component dominates in S-coda wave from P waves (Sato et al., 2012), we adopt homogeneous S wave velocity structure of 3.2 km/sec in order to calculate the spatial likelihood distribution. From the dataset used in the previous section, we extract data for locating strong scatterer from each envelope through the processing in 2.4. Stacking the likelihood distribution for the event pairs satisfying the condition of the selection described before, we obtain distribution of strong scatterer for four frequency bands. Figures 3.3.1 – 3.3.16 show the obtained distribution of 2, 4, 8, 16 Hz bands at depth ranges until 30 km with interval of 2 km. In the 2, 4, and 8 Hz bands, the strong scatterers are found near the junction of the Futagawa sand the Hinagu fault zones, near the epicenter location of the main shock of the Kumamoto earthquake and the foreshock. The distinct scatterers are detected in the 2Hz band. In this frequency band, we can see strong scatterers as follows;

1: Southern edge of the rupture zone of the Kumamoto earthquake until depth of 10 km.

2: Segment boundary of the two fault zone at depth around 15 km.

3: Western extension of the Futagawa fault zone at depth of 18 km.

All of these features seem to be relate to the fault structure and characteristics of the Kumamoto earthquake.

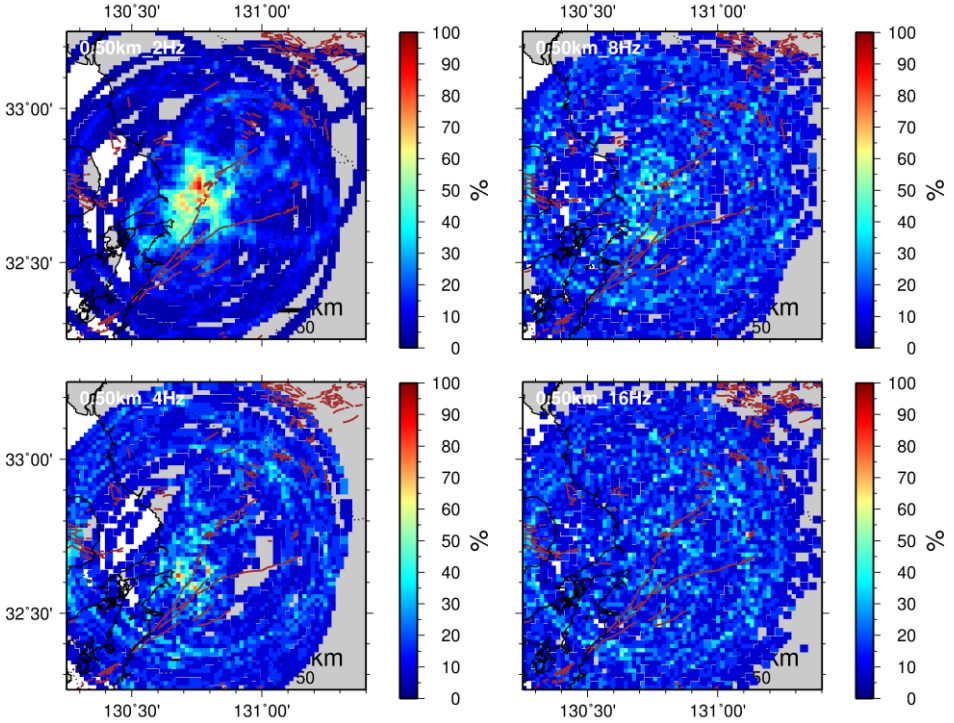

Figure 3.3.1 Map showing strong scatterers distribution at depth of 0km. The result at four frequency ranges are displayed. Color in the map indicates the ratio of the detected ripple to the sum as shown in the scale bar at the left of each map.

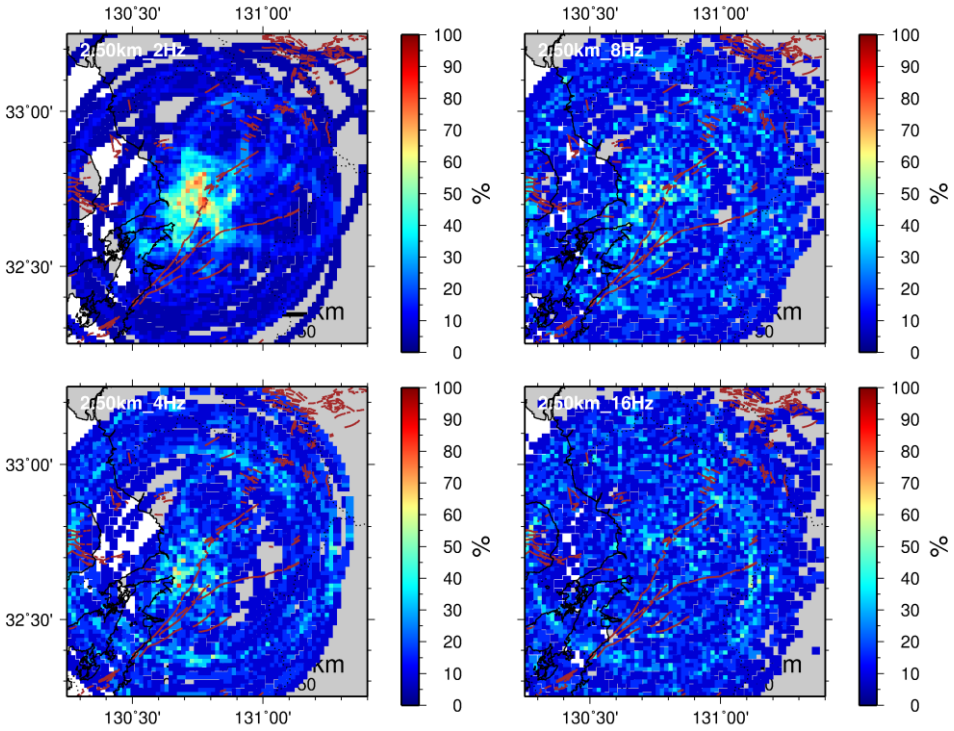

Figure 3.3.2 Same as Fig. 3.3.1 except depth= 2 km.

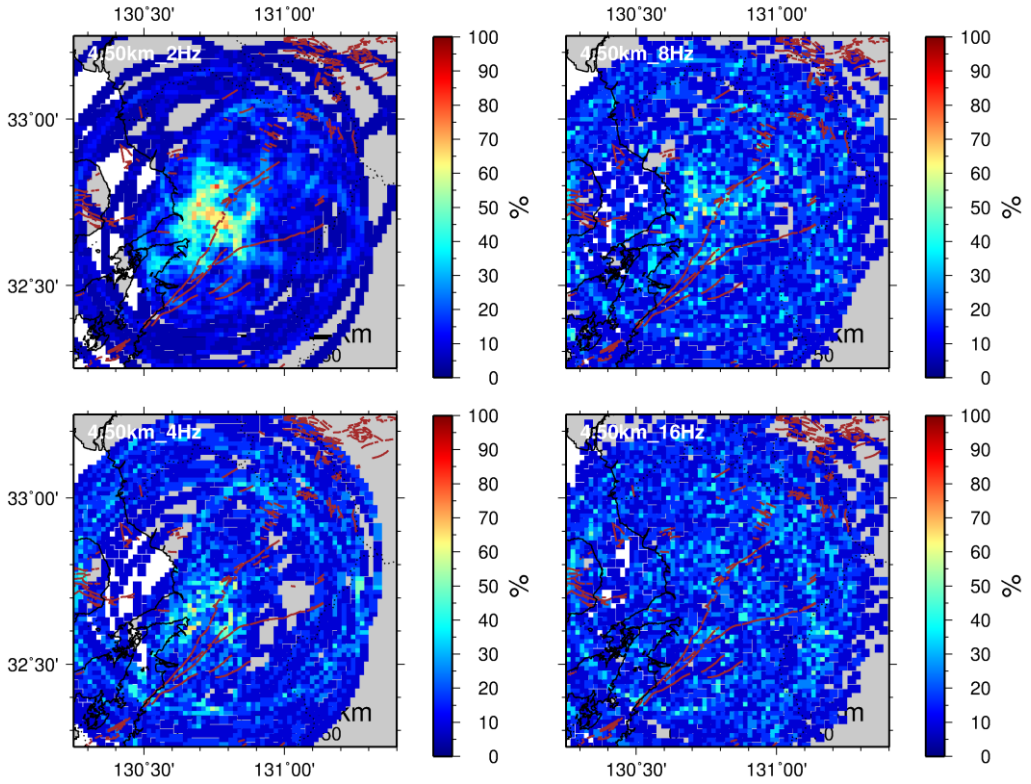

Figure 3.3.3 Same as Fig. 3.3.1 except depth= 4 km.

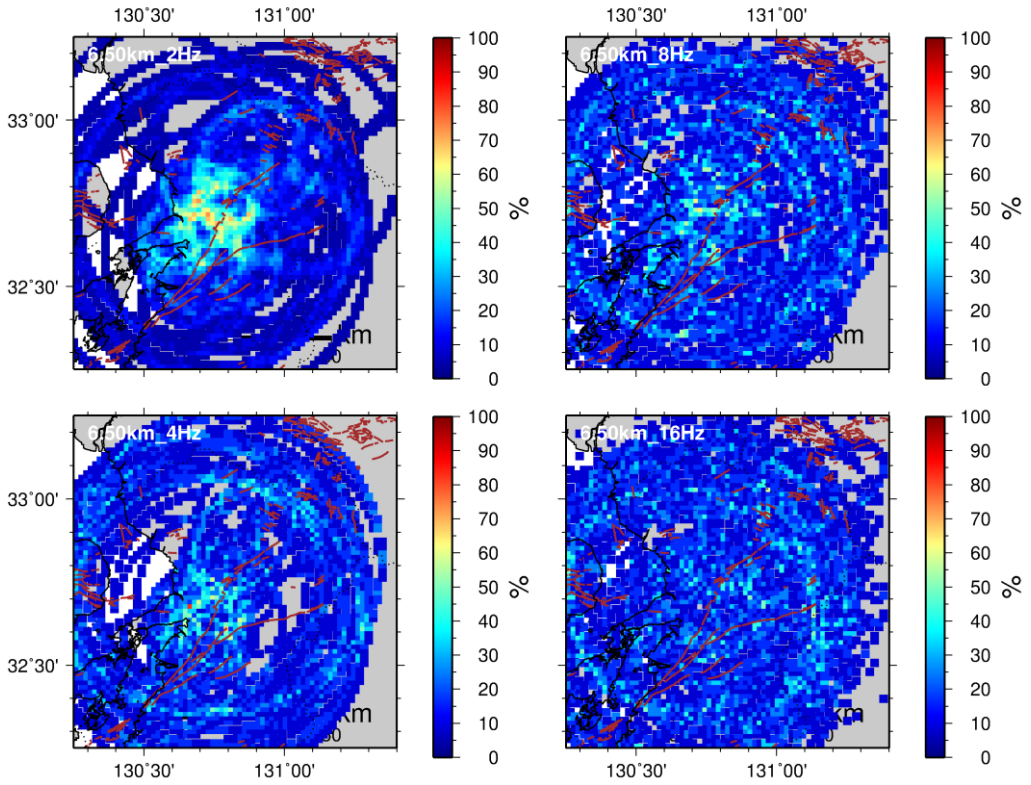

Figure 3.3.4 Same as Fig. 3.3.1 except depth= 6 km.

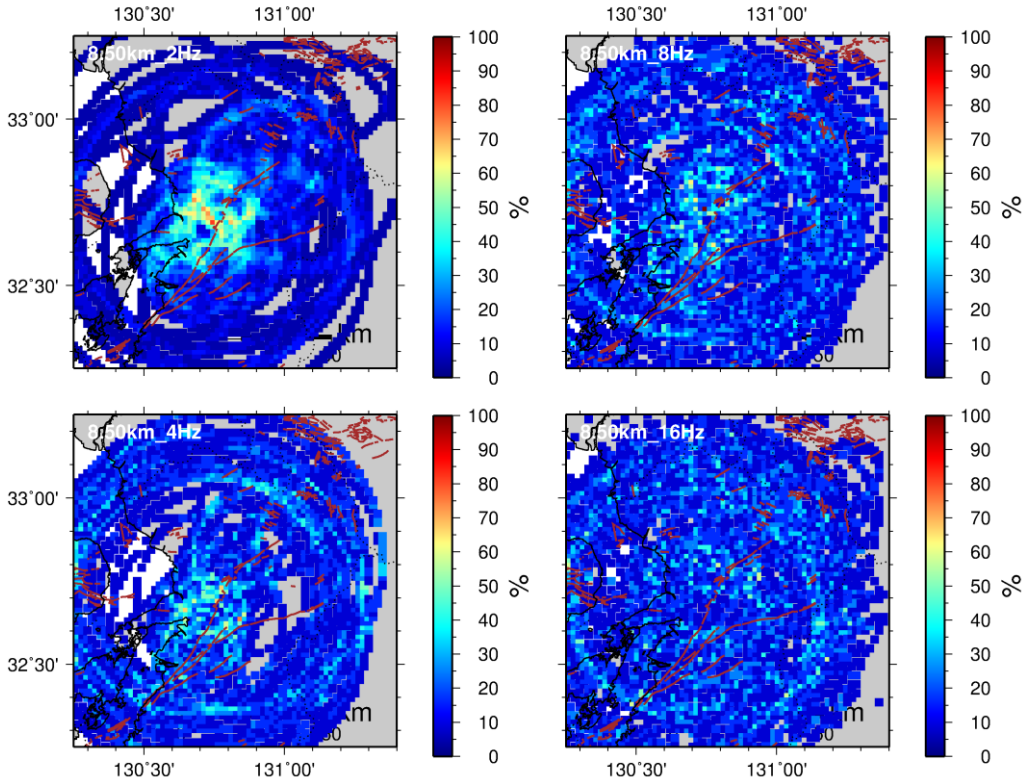

Figure 3.3.5 Same as Fig. 3.3.1 except depth= 8 km.

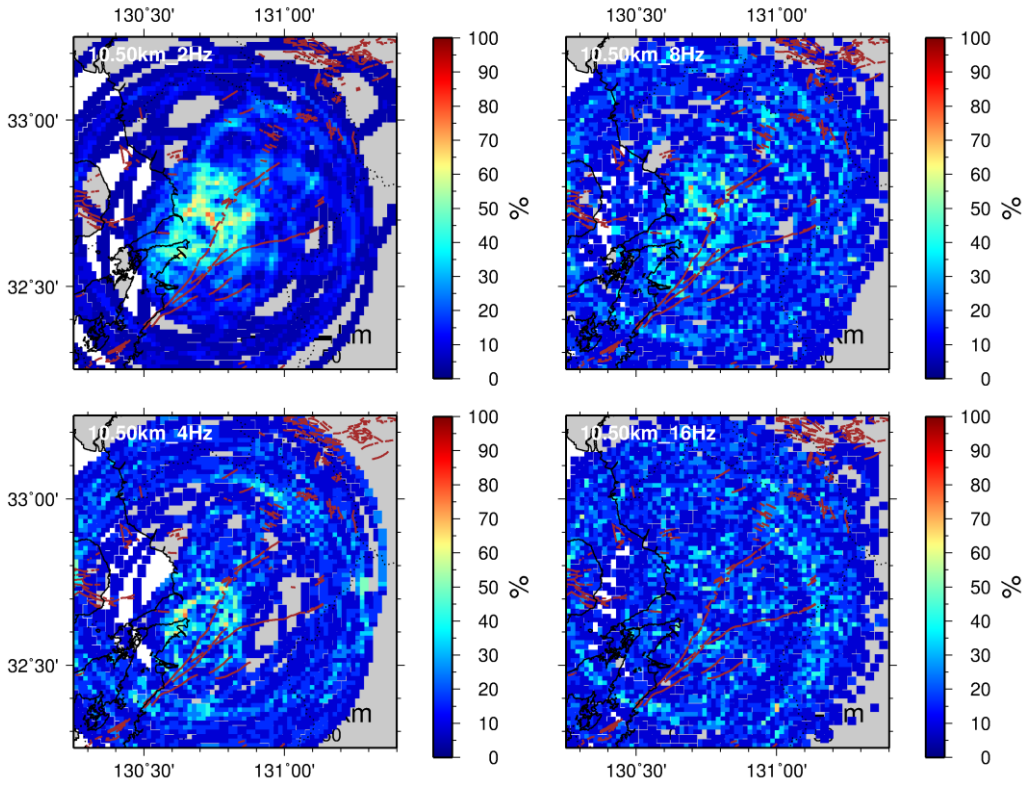

Figure 3.3.6 Same as Fig. 3.3.1 except depth= 10 km.

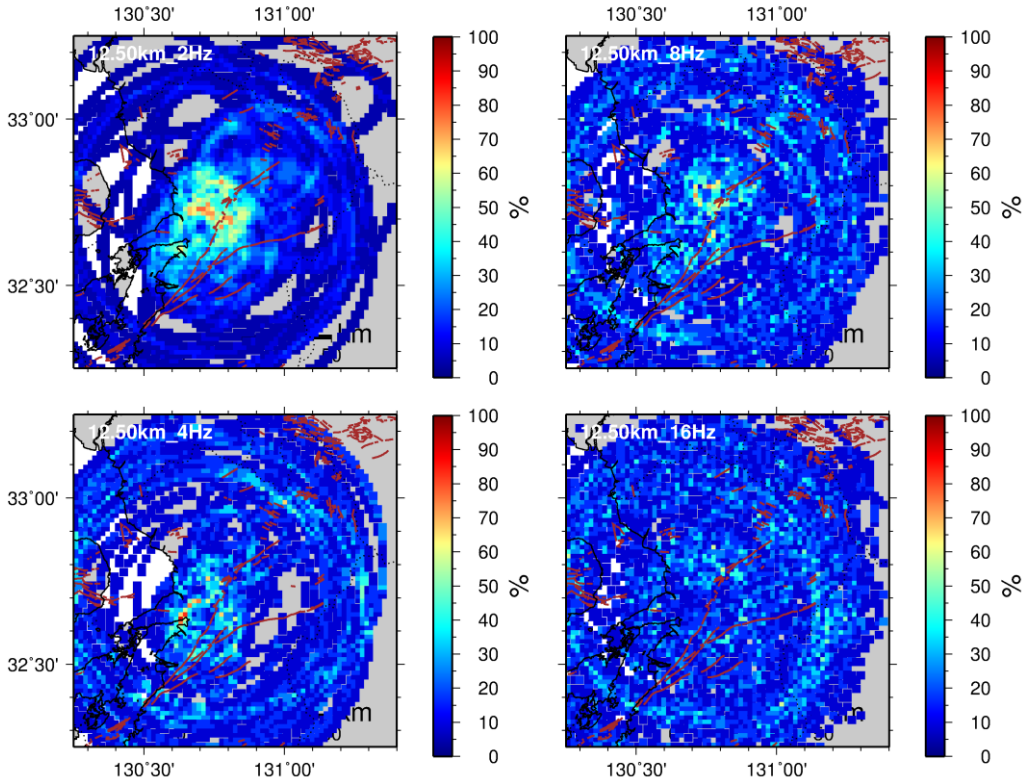

Figure 3.3.7 Same as Fig. 3.3.1 except depth= 12 km.

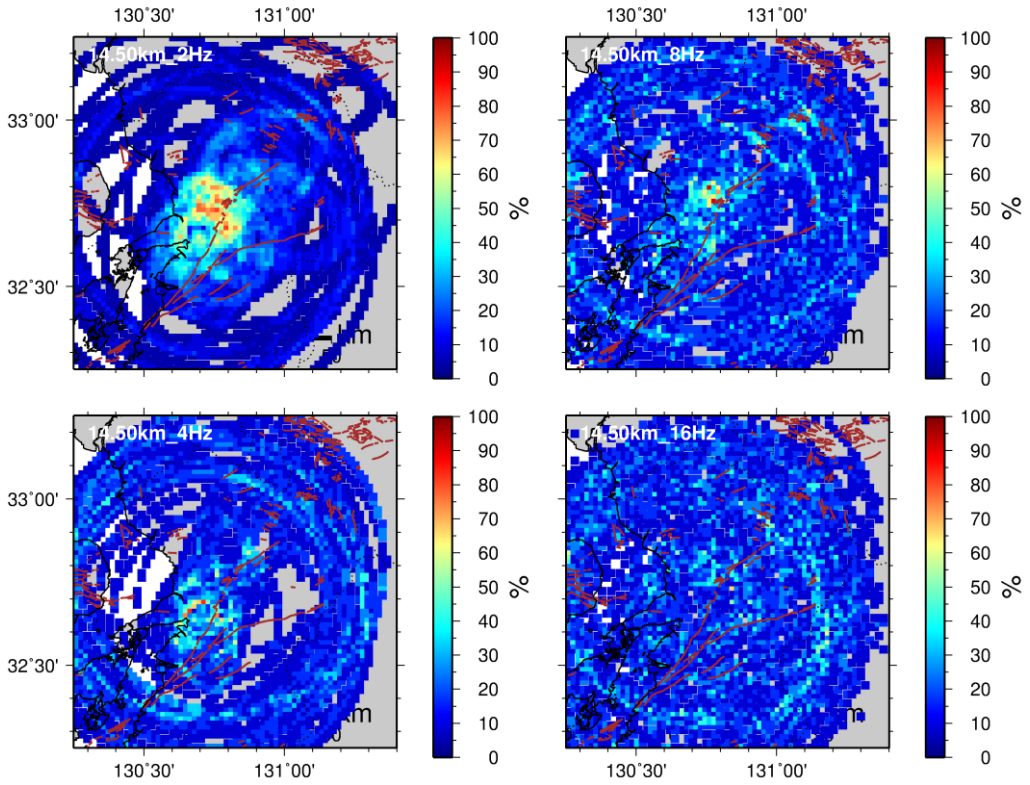

Figure 3.3.8 Same as Fig. 3.3.1 except depth= 14 km.

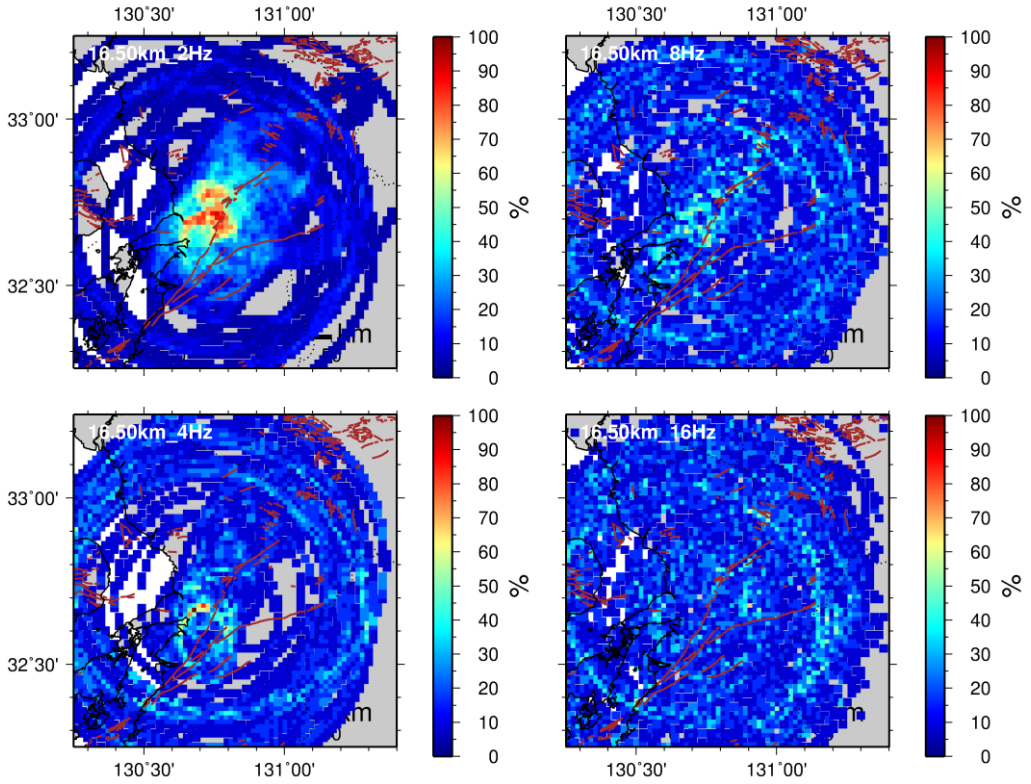

Figure 3.3.9 Same as Fig. 3.3.1 except depth= 16 km.

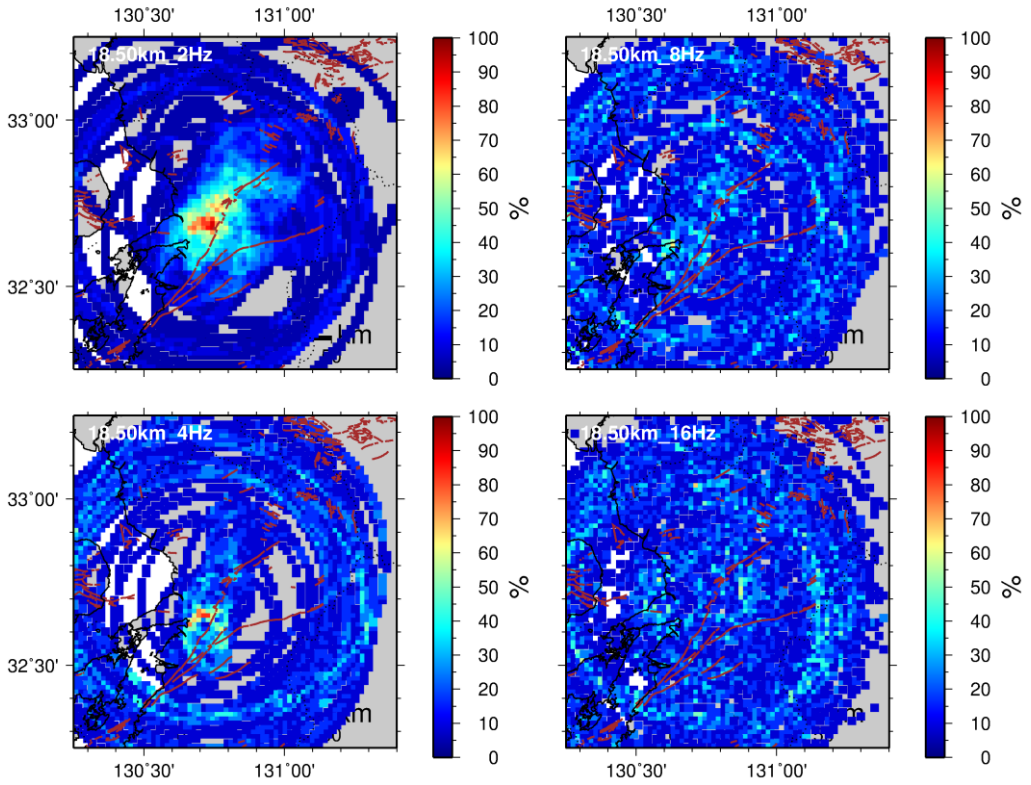

Figure 3.3.10 Same as Fig. 3.3.1 except depth= 18 km.

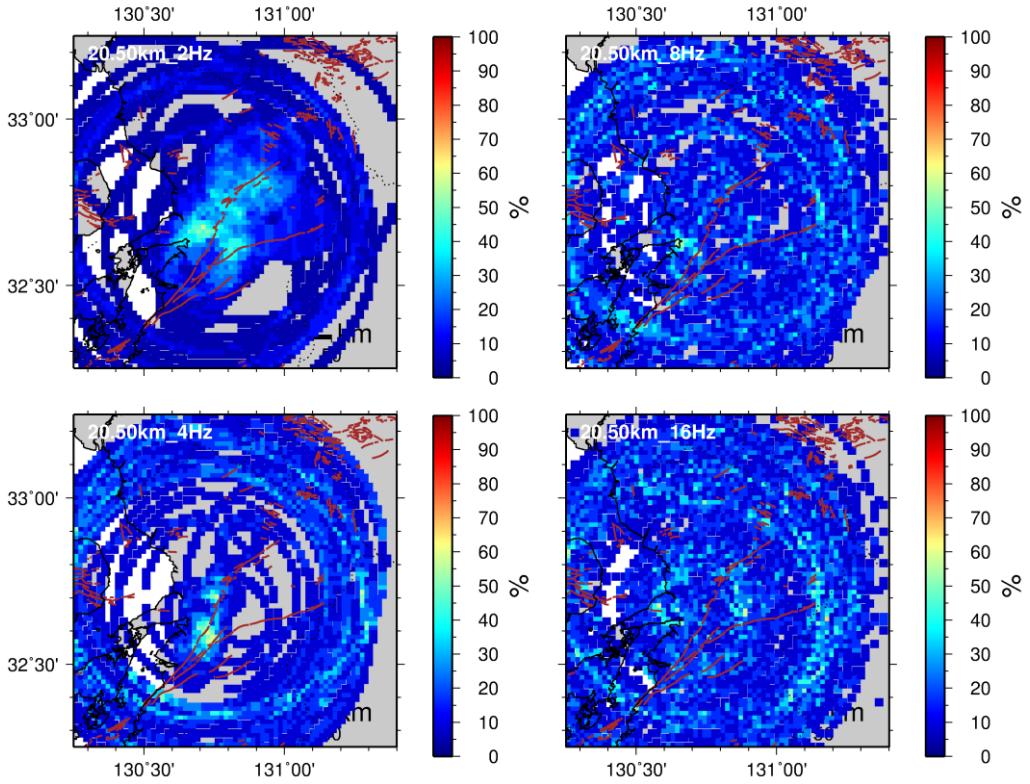

Figure 3.3.11 Same as Fig. 3.3.1 except depth= 20 km.

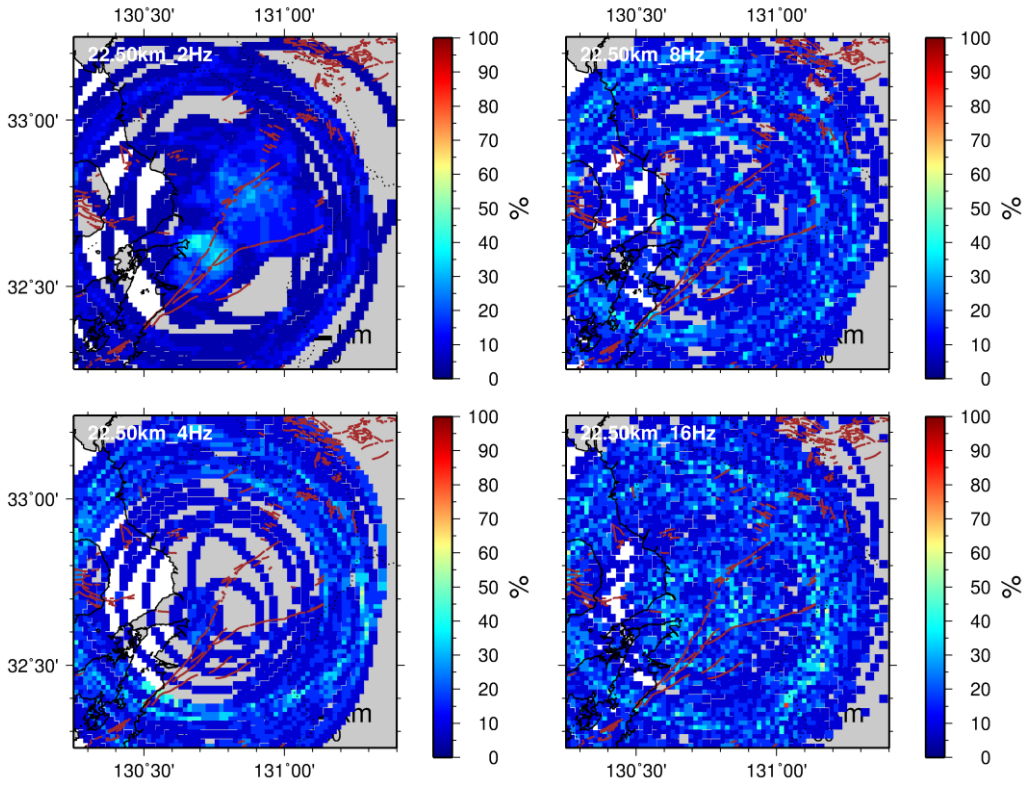

Figure 3.3.12 Same as Fig. 3.3.1 except depth= 22 km.

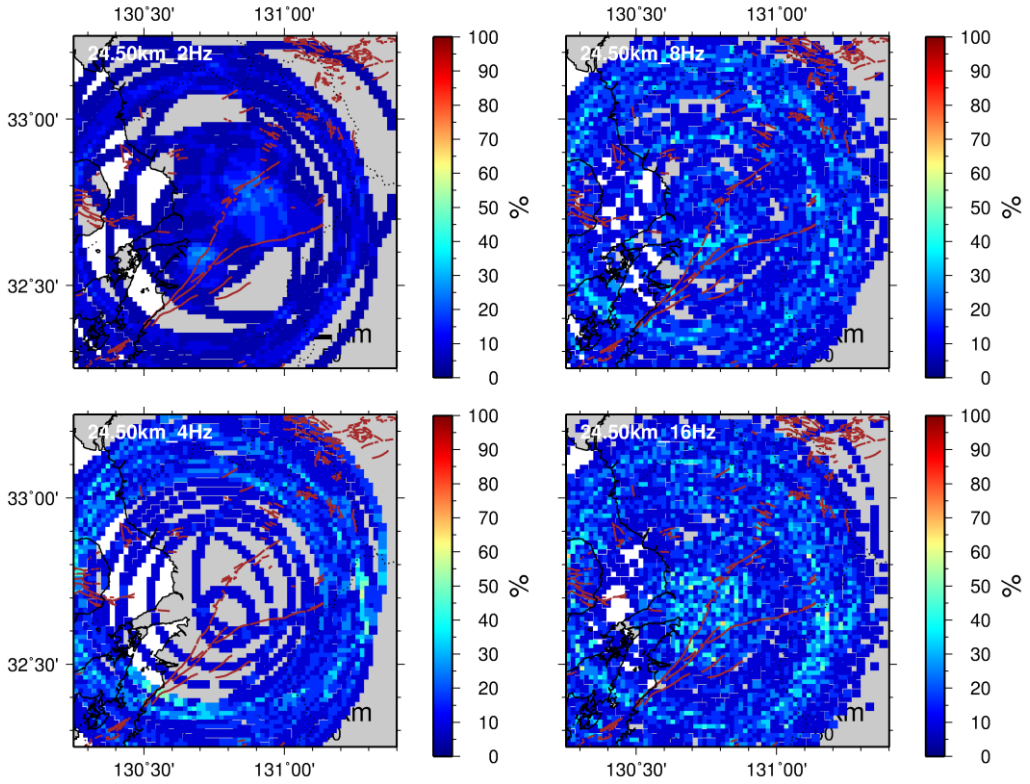

Figure 3.3.13 Same as Fig. 3.3.1 except depth= 24 km.

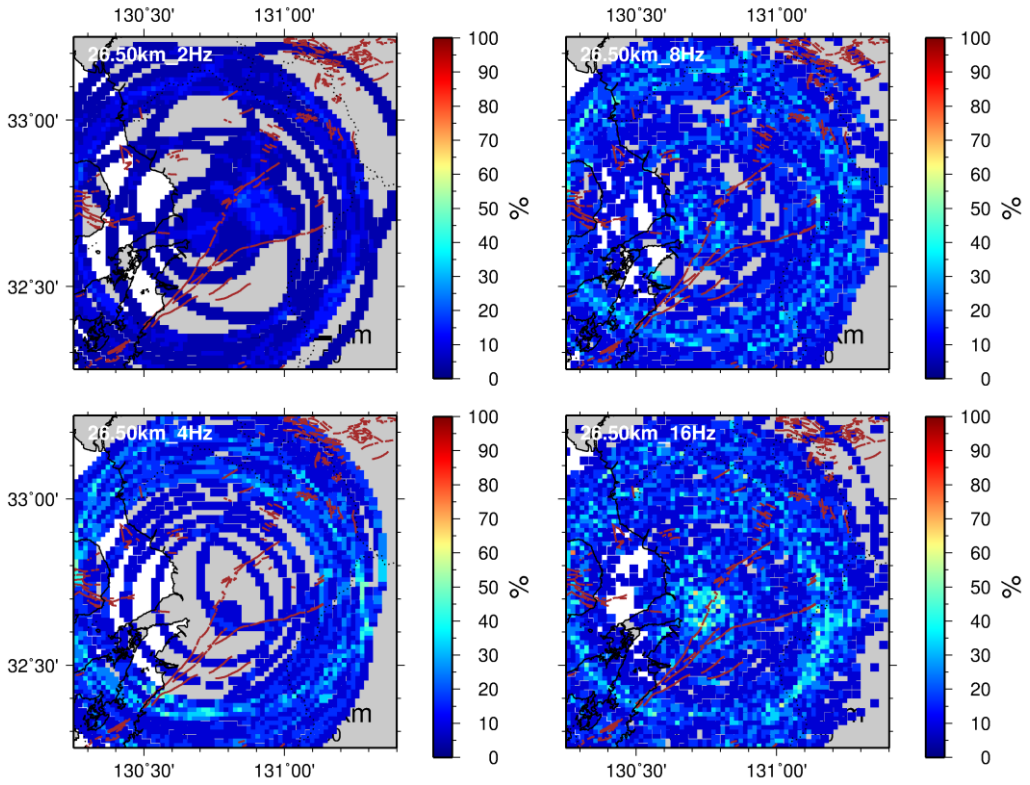

Figure 3.3.14 Same as Fig. 3.3.1 except depth= 26 km.

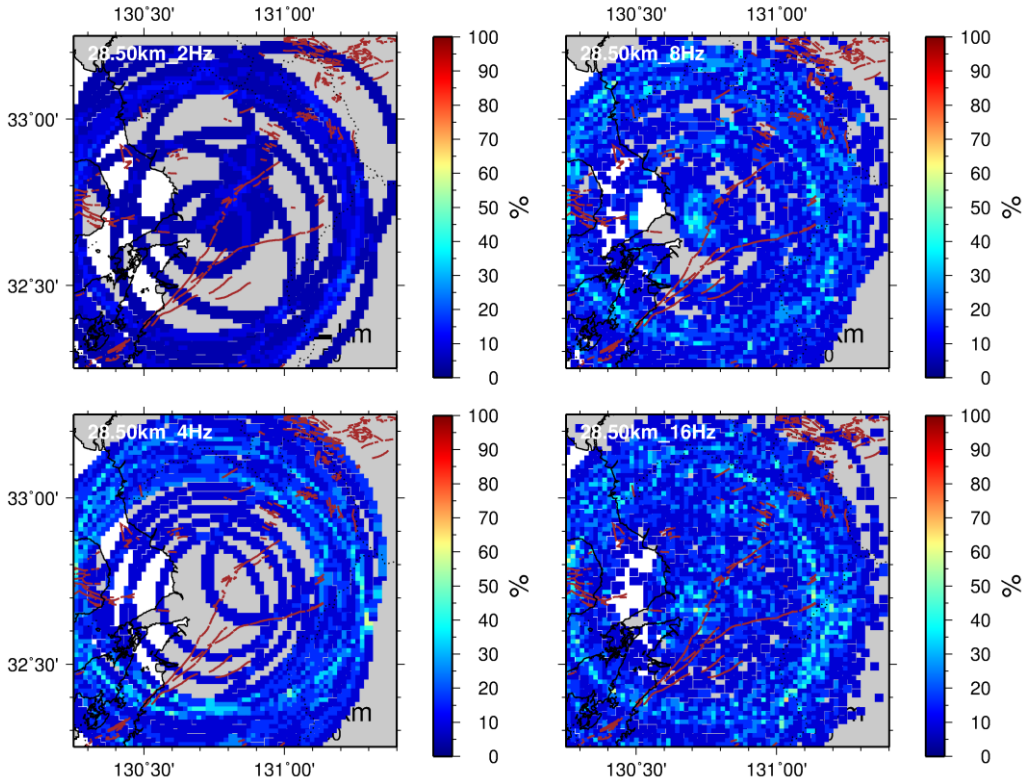

Figure 3.3.15 Same as Fig. 3.3.1 except depth= 28 km.

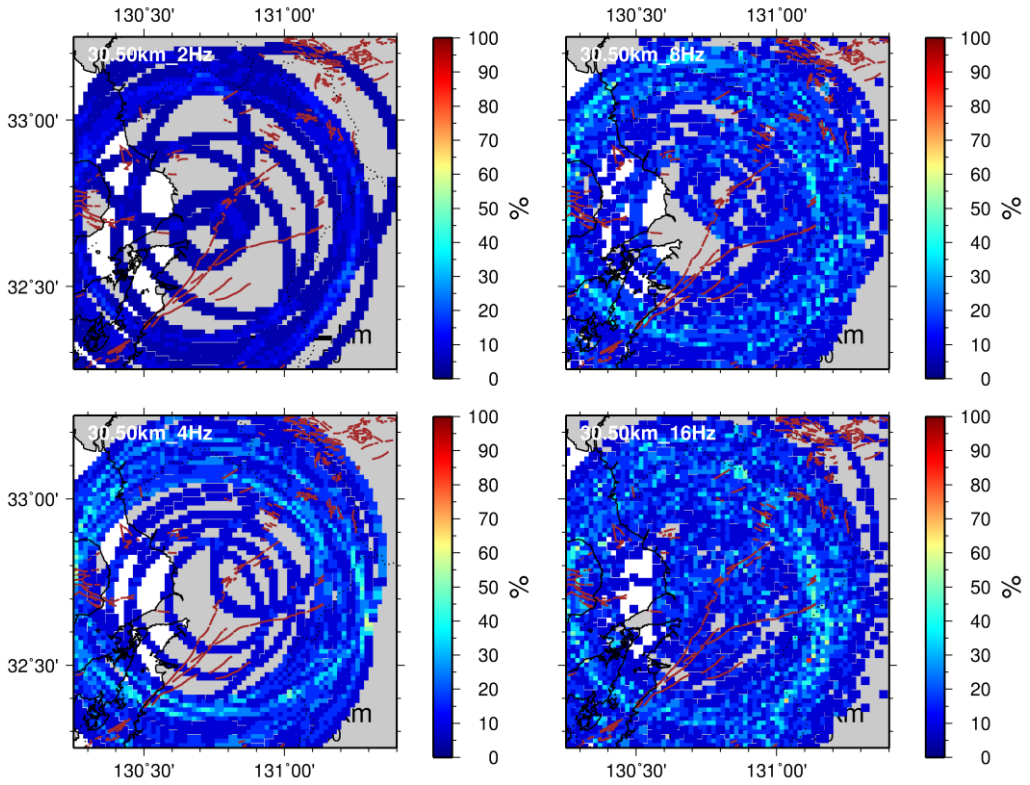

Figure 3.3.16 Same as Fig. 3.3.1 except depth= 30 km.

Chapter 4.

Discussion

We performed the envelope analysis to the seismograms observed in and around the hypocentral area of the 2016 Kumamoto earthquake sequence. The structure of Q_i^{-1} provides several features in the target area. The results suggested that the large attenuation factor around the volcano in the bands of 2, 4 Hz is attributed to the complex structure of the volcano and the existence of magma / fluid. Abe et al. (2017) detected extreme low velocity body beneath Aso volcano by the receiver function analysis. They showed that the low velocity part corresponds to the magma ascending process to the volcano. High temperature and fluid related to the process might be cause for the high attenuation structure found in this study. Wang et al. (2017) have estimated total attenuation structure, which is correspond to α_t in this study, in the similar target area. They also showed high attenuation area exist at Aso volcano. Comparing Q_i^{-1} and Q_s^{-1} structure in this study with their result, we could conclude the strong attenuation area found in the volcano mainly caused by internal attenuation mechanism. In the bands at 8, 16 Hz, the medium in the western side of the fault zone shows a feature that seismic wave is strongly attenuated, which could relate to structure due to the aftershock activity extending to the west side of the fault zone (Fig. 4.1).

The scattering attenuation factor in the west side of the fault zone is larger than that in the east side for the all frequency bands analyzed in this study, which may correspond to non-uniform seismic activity in the target area.

The region of high scattering attenuation around Aso caldera at 8 Hz does not always show good correspondence to the resistivity structure of Aizawa et al. (2017). Low and high resistivity anomaly areas are found around Aso caldera where high Q_s^{-1} value is estimated. This implies that the cause of Q_s^{-1} might not be relate to the fluid distribution in the area.

The strong scatterer distribution directly relates to Q_s^{-1} estimation from envelope shape analysis. We note that, as described above, the Q_s^{-1} structure estimated here reveals lack of the spatial resolution because the envelope within the time window used in this study is sensitive to the spatial variation in Q_i^{-1} rather than Q_s^{-1}.

The strong scatterer distribution implies relation heterogeneous structure to the activity of earthquake and fault zone structure. As shown in the results in the 16 Hz band, no remarkable scatterers are recognized. This suggests that structure with wavelength of seismic waves at 16 Hz is relatively "homogeneous" because of uniform Q_s^{-1} structure estimated.

Considering both the distributions of Q_s^{-1} and of the strong scatterers, the scattering attenuation is stronger in the west side of the fault zone than that in the east side, and the attenuation is particularly large near the junction of the fault zone. This characteristic obtained in other fault zones. For example, Nishigami (1999) have estimated that the scattering intensity is large at the segment boundary of the fault at the San Andreas fault zone.

In the target area of this study, heterogeneous structure of P waves was estimated by using scattering phases. Matsumoto et al. (2004, SSJ) showed scatterer distribution from the records of several artificial sources by array analysis. Distribution of P wave scatterer at similar frequency bands to those in this study was imaged (Fig. 4.2). The locations of parts generating the strong P wave scattered phases correspond to the Hinagu and Futagawa fault zones, which coincides the spatial feature of strong scatterer distribution of S wave in this study. Normal moveout section along the profile across the Hinagu fault have obtained by Matsumoto et al. (2004, SSJ). Figure 4.1 shows their result. The strong phases recognized in the lower crust around depth of 22 km. The strong heterogeneity in the lower crust was imaged only eastern part of the fault zone. They interpreted that heterogeneous structure in the western part is strong and complex. The reflector like structure in the eastern part might not be detected analysis in this study. However, we imaged strong heterogeneous structure in the seismogenic zone around the Hinagu and Futagawa faults.

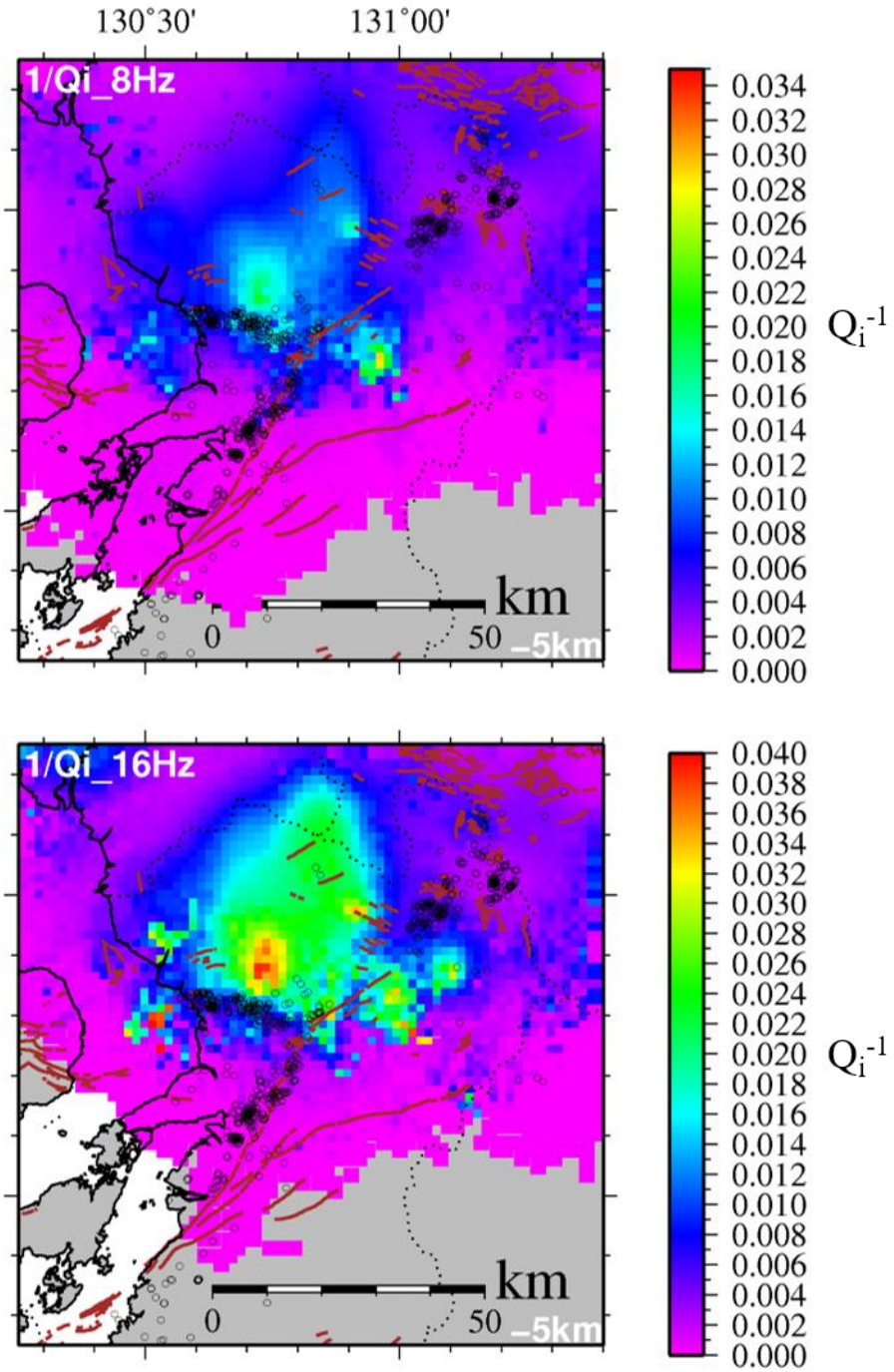

Figure 4.1 The distribution of Qi-1 and aftershock at 5 km depth. Upper panel and lower panel show the result at 8Hz and 16Hz respectively. Black solid circle indicates the location of hypocenter and its size is not dependent on the magnitude. Color in the map indicates Q_i^{-1} value as shown in the scale bar at the left of the map.

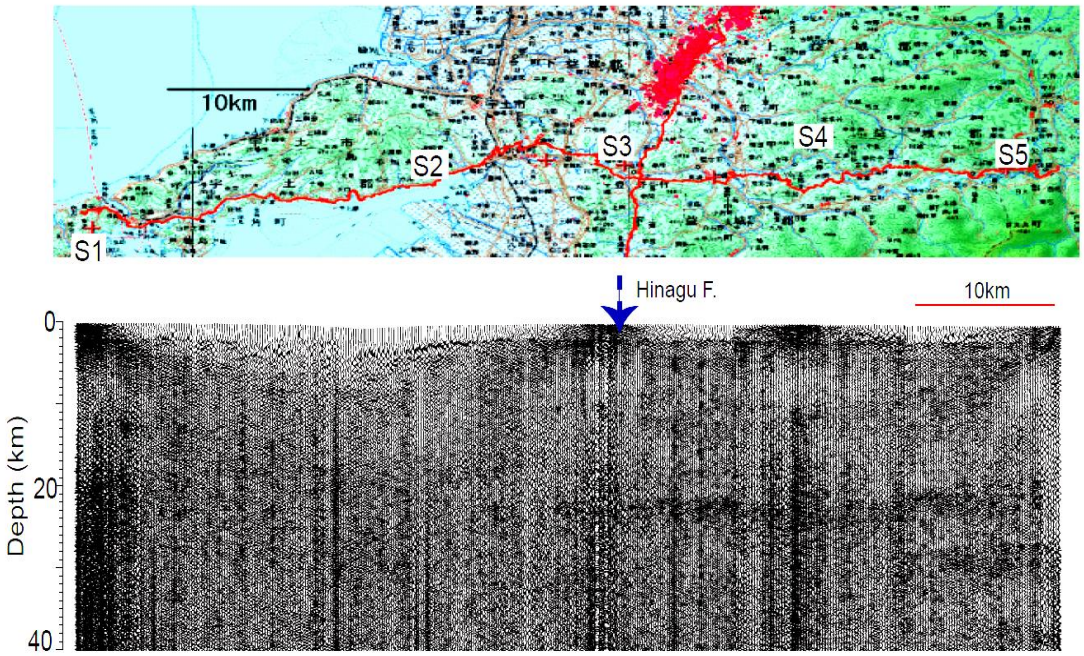

Figure 4.2 Seismic section beneath the graben. The map shows the profile of the exploration carried out by the 2003 Joint Universities seismic experiment. Lower panel shows the normal move-out section along the profile. Distinct reflectors can be found in the lower crust. (Matsumoto et al., 2004, SSJ)

Chapter 5.

Conclusion

We investigated small scale heterogeneous structure in the earth's crust. We focused envelope shape of the seismogram for shallow crustal earthquakes in order to characterize the heterogeneous structure. This study obtained conclusions in development of analysis method and heterogeneous structure in and around hypocentral area of the 2016 Kumamoto earthquake sequence as listed below.

For the method improvement;

- Three dimensional weighting factor has been introduced to estimate spatial structure in a target area.
- Monte-Carlo simulation is performed to calculate for spatial weighting factors for every station – event pairs.
- Resolution of the estimation has improved by the present method compared with previous studies.
- For the heterogeneous structure;
  Based on envelope decay analysis, intrinsic attenuation structure in lower frequency band revealed change at the geological boundary such as active fault and volcanic structure.
- In addition, scattering strength is high at the junction point between Hinagu and Futagawa faults. It is similar to the previous studies.
- Strong heterogeneity also has been detected at the junction from the ripple analysis.
- The envelope and ripple analysis reveal consistency each other.

These results showed that the seismic faulting relates to the small scale heterogeneities.

This study suggests small scale heterogeneity detecting the present study might contribute to evaluation for the potential of the earthquake occurrence.

Acknowledgement

I would like to express my deep gratitude from the bottom of my heart to Associate Prof. Satoshi Matsumoto for giving courteous and enthusiastic guidance and encouragement.
I am grateful to Prof. Hiroshi Shimizu for his useful advices and encouragements.
I also would like to give Dr. Azusa Shito my gratitude for study on seismic attenuation structure together and technical support.
I would like to thank Associate Prof. Takeshi Matsushima for his technical support and useful comments for making presentation.
I would like to thank the members of the institute of seismology and volcanology, faculty of sciences, Kyushu University.
This work is partly supported by MEXT under KAKENHI Grant Number 16H06298, under Comprehensive Research Project for the major active faults related to The 2016 Kumamoto Earthquake, and Earthquake and Volcano Hazards Observation and Research Program, and also supported by Earthquake Research Institute, The University of Tokyo under Joint Usage Program.
I used data by JMA, NIED, Kyoto, Kyushu Universities and the Group for Urgent Joint Seismic Observation of the 2016 Kumamoto Earthquakes. We are grateful to Dr. Hoshiba for the computation program of Monte-Carlo simulation, and for parallel calculation of this simulation we have used the computer systems of the Earthquake and Volcano Information Center of the Earthquake Research Institute, the University of Tokyo. I used Generic Mapping Tools (Wessel and Smith,1998) to draw figures.

References

Abe, Y., Ohkura, T., Shibutani, T., Hirahara, K., Yoshikawa, S., Inoue, H. (2017), Low-velocity zones in the crust beneath Aso caldera, Kyushu, Japan, derived from receiver function analyses, Journal of Geophysical Research: Solid Earth, 122 (3), pp. 2013-2033

Aizawa, K., Asaue, H., Koike, K., Takakura, S., Utsugi, M., Inoue, H., Yoshimura, R., Yamazaki, K., Komatsu, S., Uyeshima, M., Koyama, T., Kanda, W., Shiotani, T., Matsushima, N., Hata, M., Yoshinaga, T., Uchida, K., Tsukashima, Y., Shito, A., Fujita, S., Wakabayashi, A., Tsukamoto, K., Matsushima, T., Miyazaki, M., Kondo, K., Takashima, K., Hashimoto, T., Tamura, M., Matsumoto, S., Yamashita, Y., Nakamoto, M., Shimizu, H. (2017), Seismicity controlled by resistivity structure: The 2016 Kumamoto earthquakes, Kyushu Island, Japan, Earth, Planets and Space., 69, 4.

Aki, K. (1969), Analysis of the seismic coda of local earthquakes as scattered waves, Journal of Geophysical Research., 74, 615-631.

Asano, Y. and Hasegawa, A. (2004), Imaging the fault zones of the 2000 western Tottori earthquake by a new inversion method to estimate three-dimensional distribution of the scattering coefficient, Journal of Geophysical Research., 109, B06306.

Asano, K., Iwata, T. (2016), Source rupture processes of the foreshock and mainshock in the 2016 Kumamoto earthquake sequence estimated from the kinematic waveform inversion of strong motion data, Earth, Planets and Space, 68 (1)

Del Pezzo, E., Ibáñez, J., Prudencio, J., Bianco, F. and De Siena, L. (2016), Absorption and scattering 2-D volcano images from numericallycalculated space-weighting functions. Geophysical Journal International., 206(2), 742–756.

Del Pezzo, E., De La Torre, A., Bianco, F., Ibanez, J., Gabrielli, S., De Siena, L. (2018), Numerically calculated 3d space-weighting functions to image crustal volcanic structures using diffuse coda waves, Geosciences (Switzerland), 8 (5), art. no. 175.

Komatsu, M., Takenaka, H. and Oda, H., (2017), Three-dimensional P- and S-wave attenuation structures around the source region of the 2016 Kumamoto earthquakes, Earth, Planets and Space., 69, 101.

Matsumoto, S., Watanabe, A., The Research Group for the 2003 Hinagu Fault Seismic Expedition (2004), P-wave scatterer distribution around Hinagu Fault, Kyushu, Japan, based on seismic array observation, S06-08151210-0182A, 10/11, B78, 2004 Fall Meeting of Seismological Society of Japan.

Nshigami, K. (1991), A new inversion method of coda waveforms to determine spatial distribution of Coda scatterers in the crust and uppermost mantle, Geophysical Research Letters., 18, 2225-2228.

Nishigami, K. (1997), Spatial distribution of coda scatterers in the crust around two active volcanoes and one active fault system in central Japan: Inversion analysis of coda envelope, Physics of the Earth and Planetary Interiors., 104, 75-89.

Nishigami, K. (2000), Deep crustal heterogeneity along and around the San Andreas fault system in central California and its relation to the segmentation, Journal of Geophysical Research., 105, 7983-7998.

Obara, K. (1997), Simulations of anomalous seismogram envelopes at coda portions, Physics of the Earth and Planetary Interiors., 104, 109-125.

Paasschens, J. C. (1997), Solution of the time-dependent Boltzmann equation, Physical Review E., 56, 1135–1140.

Sato, H., Fehler, M.C., Maeda, T. (2012), Seismic wave propagation and scattering in the heterogeneous earth: Second edition

Shirahama, Y., Yoshimi, M., Awata, Y., Maruyama, T., Azuma, T., Miyashita, Y., Mori, H., Imanishi, K., Takeda, N., Ochi, T., Otsubo, M., Asahina, D., Miyakawa, A. (2016), Characteristics of the surface ruptures associated with the 2016 Kumamoto earthquake sequence, central Kyushu, Japan, Earth, Planets and Space, 68 (1), art. no. 191

Shito, A., Matsumoto, S., Shimizu, H., Ohkura, T., Takahashi, H., Sakai, S., Okada, T., Miyamachi, H., Kosuga, M., Maeda, Y., Yoshimi, M., Asano, Y., Okubo, M. (2017), Seismic velocity structure in the source region of the 2016 Kumamoto earthquake sequence, Japan, Geophysical Research Letters., 44, 7766–7772.

Wang, Z.W., Zhao, D., Liu, X. and Li, X. (2017), Seismic attenuation tomography of the source zone of the 2016 Kumamoto earthquake (M 7.3), Journal of Geophysical Research., 122, 2988–3007.

Yoshimoto, K. (2000), Monte Carlo simulation of seismogram envelopes in scattering media, Journal of Geophysical Research., 105, 6153-6161.